UC San Diego
UC San Diego Electronic Theses and Dissertations

Title

ELAVL3 Disruption in Amyotrophic Lateral Sclerosis and Frontotemporal Lobar Degeneration: A Neuropathological View

Permalink

https://escholarship.org/uc/item/8z40c8m5

Author

Costantino, Isabel M

Publication Date

2024

Peer reviewed|Thesis/dissertation

UNIVERSITY OF CALIFORNIA SAN DIEGO

ELAVL3 Disruption in Amyotrophic Lateral Sclerosis and Frontotemporal Lobar
Degeneration: A Neuropathological View

A dissertation submitted in partial satisfaction of the requirements
for the degree Doctor of Philosophy

in

Neurosciences

by

Isabel Costantino

Committee in charge:

> Professor Don Cleveland, Chair
> Professor John Ravits, Co-chair
> Professor Eugene Yeo
> Professor Amir Zarrinpar

2024

The dissertation of **Isabel Costantino** is approved, and it is acceptable in quality and form for publication on microfilm and electronically.

University of California San Diego
2024

DEDICATION

To my family near and far.

TABLE OF CONTENTS

LIST OF ABBREVIATIONS

AD	Alzheimer's disease
ALS	Amyotrophic lateral sclerosis
bvFTD	Behavioral variant frontotemporal dementia
CBD	Corticobasal degeneration
CBS	Corticobasal syndrome
CE(s)	Cryptic exon(s)
CISH	Chromogenic *in situ* hybridization
ELAVL	Embryonic lethal abnormal visual system-like
FFPE	Formalin-fixed paraffin embedded
FTD	Frontotemporal dementia (clinical diagnosis)
FTD-MND	Frontotemporal dementia- Motor neuron disease
FTLD	Frontotemporal lobar degeneration (neuropathological diagnosis)
IF	Immunofluorescence
LMN	Lower motor neuron
naPPA	Non-fluent variant Primary Progressive aphasia
nELAVL	Neurally-expressed ELAVL family members (ELAVL2, ELAVL3, ELAVL4)
OPC	Oligodendrocyte precursor cell
PSP	Progressive supranuclear palsy
pTDP-43	Phosphorylated TDP-43
qPCR	Quantitative reverse transcription polymerase chain reaction
RBP	RNA binding protein
RRM	RNA recognition motif
RT-PCR	Reverse transcription polymerase chain reaction
svPPA	Semantic variant Primary Progressive Aphasia
TDP43	Transactivation response element DNA-binding protein 43 (TDP-43)
UMN	Upper motor neuron
UTR	Untranslated region

LIST OF FIGURES

LIST OF TABLES

ACKNOWLEDGMENTS

My journey in medical research is an odyssey fifteen years in the making. I owe immense gratitude to those who have nurtured my growth as a scientist, physician, and human being. Foremost, I would like to thank my family. My partner in life, David Espiritu, is unwavering in his support. He is the best example of resilience and persistence I have ever known—a man to set high goals and exceed them. My achievements in this doctoral program would not have been possible without the home and life we built together.

I wish to thank my parents, Diana and Jason Costantino. They instilled a profound sense of love, curiosity, service, and scholarship in my heart. I am lucky to call you my parents (thank you for not kicking me off the family cellphone plan). Thank you to my big brother, Benjamin Costantino. He is my role model, and it has brought tremendous joy to deepen our relationship as adults. I'm sorry for unique chaos that only a younger sister can bring into an older brother's life (and lying to Mom and Dad about you to get my way). Thank you to my big sister, Cristina Costantino. She trailblazed a path that sparked my medical and research dreams. I cherish the time we are together, and I thank her for the East Coast home away from home she always provided. I attended her thesis presentation as a young college student, and as a toast I said, "Thank you for proving someone with a PhD can also have tattoos," and I stand by that statement today. I wish to thank my family in Los Angeles, Monica Hall-Gressler and Eric Gressler, who always welcomed David and I into their home for respite. I thank my cousin, Kalen Gressler, who has made me feel like the cool cousin for years. I am thankful for your presence in my life.

I express my heartfelt appreciation to my advisor, John Ravits. His unwavering support, enthusiasm, and positivity not only sparks passion but also propels his mentees

towards success. Thank you for answering emergency phone calls and emails, pushing me to present and publish my work, and having empathy and kindness for your mentees. I will be forever proud to say you were my mentor.

Chapter 2 contains material taken from the manuscript by Costantino, I.M., Meng, A., Ravits, J. (2024) "Alternatively spliced ELAVL3 cryptic exon 4a causes ELAVL3 downregulation in ALS TDP-43 proteinopathy" Accepted for submission at *Acta Neuropathologica*. I, Isabel Costantino, am the primary investigator and author of this paper.

VITA

2008-2012	Bachelor of Arts, Neuroscience Bachelor of Arts, Cell Biology Dartmouth College – Hanover, NH
2012-2016	Research Technician & Tissue Bank Coordinator Massachusetts General Hospital – Boston, MA
2016-2018	Medical Student, Medical Scientist Training Program UCSD School of Medicine – La Jolla, CA
2018-2024	Doctor of Philosophy, Neurosciences University of California San Diego – La Jolla, CA

SELECT PUBLICATIONS

Costantino I, Meng A, Ravits J. Alternatively spliced ELAVL3 cryptic exon 4a causes ELAVL3 downregulation in ALS TDP-43 proteinopathy. 2024 Accepted for publication at *Acta Neuropathologica*

Costantino I, Nicodemus J, Chun J. Genomic Mosaicism Formed by Somatic Variation in the Aging and Diseased Brain. *Genes* (Basel). 2021 Jul 14;12(7):1071.

Marquez A, Guernsey LS, Frizzi KE, Cundiff M, **Costantino I,** Muttalib N, Arenas F, Zhou X, Lim SH, Ferdousi M, Ponirakis G, Silverdale M, Kobylecki C, Jones M, Marshall A, Malik RA, Jolivalt CG. Tau associated peripheral and central neurodegeneration: Identification of an early imaging marker for tauopathy. *Neurobiol Dis*. 2021 Apr;151:105273.

ABSTRACT OF THE DISSERTATION

ELAVL3 Disruption in Amyotrophic Lateral Sclerosis and Frontotemporal Lobar

Degeneration: A Neuropathological View

by

Isabel Costantino

Doctor of Philosophy in Neurosciences

University of California San Diego, 2024

Professor Don Cleveland, Chair
Professor John Ravits, Co-chair

Amyotrophic lateral sclerosis (ALS) and frontotemporal lobar degeneration (FTLD)

are overlapping neurodegenerative diseases characterized by dysfunction of RNA binding

proteins (RBPs)[1,2]. The hallmark of greater than 95% of ALS and nearly half of FTLD cases involve the RBP TDP-43 (FTLD-TDP43), which mislocalizes from the nucleus and forms hyperphosphorylated cytoplasmic aggregations[2,3]. In FTLD related to hyperphosphorylated tau aggregates (FTLD-Tau), RBP dysfunction is also present[4].

Our group has identified ELAVL3 as an RBP dysregulated in ALS spinal cord[5,6]. Like TDP-43, ELAVL3 is involved in mRNA stability, alternative splicing and polyadenylation, and transcription rate[7]. Low transcript levels of *ELAVL3* and mislocalization of ELAVL3 protein out of the nuclear compartment is characteristic of ALS spinal cord motor neurons[5]. *ELAVL3* has been identified as a target gene of TDP-43[8]. Loss of TDP-43 nuclear splice function results in expression of non-conserved exonic sequences (cryptic exons, CEs)[9]. These inserted sequences can induce frameshifting, add premature stop or polyadenylation sequences, and/or changes the protein coding sequence. *ELAVL3* shows expression of CE 4a with *in vitro* knockdown of TDP-43 and FTLD-TDP43 frontal cortex[10,11].

Here, we report evidence for a pathogenic link between ELAVL3 and TDP-43 or Tau aggregates in ALS/FTLD brain and spinal cord. We confirm the expression of *ELAVL3* CE 4a in 40-70% of ALS spinal cord and motor cortex using multiple modalities. We predict ELAVL3 downregulation seen in anterior horn motor neurons is due to production of CE 4a-containing transcripts destined for destruction via non-sense mediated decay. We also expand previous neuropathologic findings of ELAVL3 nuclear loss in ALS spinal cord motor neurons[5]. We demonstrate ALS Betz cells are resilient to pathologic changes to ELAVL3 expression relative to spinal cord motor neurons; however, neurons of layers 3 and 5 of the motor cortex have reduced nuclear ELAVL3 expression. We show a triad of ELAVL3 pathologic findings in ALS motor cortex and FTLD frontal cortex: (1) reduction of nuclear

ELAVL3 expression in the presence of intracellular phosphorylated tau (pTau) or phosphorylated TDP-43 (pTDP-43), (2) rare cortical cells with ELAVL3 nuclear depletion and granular cytoplasmic aggregation, and (3) neuropil ELAVL3 "beads on a string" aggregates.

CHAPTER 1: BACKGROUND OF ALS/FTD, DYSFUNCTION OF RNA HOMEOSTASIS, AND THE RNA BINDING PROTEIN ELAVL3

1.1 Amyotrophic lateral sclerosis and frontotemporal dementia—discovery and natural history

Amyotrophic lateral sclerosis (ALS) is rare but uniformly fatal motor disease characterized by dysfunction and progressive degeneration of motor cortex upper motor neurons and spinal cord and brainstem lower motor neurons[12]. Descriptions of lower motor neuron-restricted cases of ALS were reported as early as the 1820s by Charles Bell[13], François-Amilcar Aran[14], and Jean Cruveilhier[15] and labeled as "progressive muscular atrophy"[16]. In his 1874 publication *De la sclérose latérale amyotrophique*, Jean-Martin Charcot defined the disease based on the clinical findings of progressive muscle atrophy ("amyotrophic" or "without nourishment to muscles") and neuropathologic findings of hardening ("sclerosis") of the descending "lateral" corticospinal tracts due to loss of anterior horn motor neurons[17]. There was early recognition that syndromes involving upper motor neuron degeneration, lower motor neuron degeneration, and mixed findings were linked[18]. The umbrella disorder of these linked presentations was termed "motor neuron disease" by W. Russell Brain[19].

The clinical phenotypes of ALS are classified by the degree of upper versus lower motor involvement as well as the location of disease onset[20]. Progressive muscular atrophy represents pure or predominant lower motor neuron dysfunction. In addition to muscle atrophy, patients can have flaccid paralysis, decreased deep tendon reflexes, and decreased overall tone. Primary lateral sclerosis refers to pure or predominant upper motor

neuron dysfunction. Patients can still present with muscle atrophy, but may show increased tone, spastic paralysis, and increased deep tendon reflexes. "Classical" ALS involves both upper and lower motor neuron involvement and thus can present with a mixture of motor signs. Bulbar-onset and pseudobulbar onset ALS are classifications based on focal onset in the muscles controlling speech, mastication, and swallowing in a predominantly lower motor neuron (LMN) and upper motor neuron pattern (UMN), respectively. The spread of the disease from the initial lesion, as shown by clinical presentation, typically occurs contralaterally at the same level (i.e. from one arm to the other) with lower motor neuron involvement and ipsilaterally (i.e. from the arm to the leg on the same side) with upper motor neuron involvement[21].

Age of onset peaks between 58-63 years, but for patients with genetic lesions, onset peaks nearly a decade younger[22]. The average time from onset to diagnosis is roughly a year, and inappropriate medical/surgical intervention is a common report[23]. The clinical endpoint for ALS patients is total respiratory failure necessitating mechanical ventilatory support. Disease features associated with worse prognosis include site of onset (respiratory and bulbar-onset ALS), increased age of onset, and measured rate of functional voluntary movement loss[24]. Survival from symptom onset is roughly inverse to age[24]. Those diagnosed younger than 45 often survive for greater than 10 years. For roughly half the population with symptom onset in mid-late adulthood (45-70 years old), survival is < 2.5 years; however, roughly 5-10% have a long average survival time of 5-10 years. For elderly adults older than 70 years old, average survival drops to ~1.7 years. About half of ALS patients have cognitive impairment—roughly 20% meeting clinical criteria for frontotemporal

dementia (FTD) and an additional 30% with behavioral, cognitive, or non-executive impairment[25].

FTD is a clinical disease characterized by progressive executive, language, and/or motor dysfunction most commonly linked to degeneration of frontal and temporal lobes and subcortical regions, known as frontotemporal lobar degeneration (FTLD)[1,26]. It is a leading cause of dementia in patients under 65 years old[1]. In 1892, Arnold Pick wrote the first description of FTD in a case study of a patient named August H.[27]; Pick linked the temporal lobe atrophy to the man's severe aphasia. In 1911, Alois Alzheimer described the histologic findings of swollen neurons, later called "Pick cells"[28]. From Alzheimer's description, it took nearly 100 years to detangle the clinical and neuropathologic features of "Pick's disease" from the more studied Alzheimer's disease[29]. A consensus for diagnostic criteria for clinical FTD was established in the late 1990s[30] and pathological criteria for FTLD a decade later[31].

Under the umbrella of FTD there are three clinical syndromes: behavioral-variant FTD (bvFTD), semantic dementia, and progressive non-fluent aphasia[30,32]. bvFTD is characterized by indolent decline in executive and interpersonal skills resulting in abnormal behaviors (i.e., disinhibition, impulsivity, stereotyped behaviors, social unawareness). Semantic dementia is a form of primary progressive aphasia (semantic variant, svPPA) characterized by progressive loss of semantic memory—the vocabulary of objects and concepts in the world. Speech will remain fluent but can be circumlocutory and imprecise. More severe impairments in sense memory can include prosopagnosia (face blindness) and visual agnosia. Non-fluent/agrammatic primary progressive aphasia (naPPA) is characterized by progressive loss of language output resulting in effortful, dysarthric speech often accompanied by apraxia of orofacial movements (i.e., yawning on command). These

syndromes also have variable overlap with atypical parkinsonism and motor neuron disease. An estimated 15% of FTD patients meet clinical criteria for ALS[33].

The clinical course for each of these syndromes is steadily progressive with variable survival duration. Patients with concurrent motor neuron disease typically survive less than five years after symptom onset, whereas patients with semantic dementia can survive more than a decade; however, there is a general convergence over time of these syndromes[34]. Unlike ALS, FTD is not considered a fatal disease. Average age of onset is approximately 58 years old, and patients can live many decades with the disease[35].
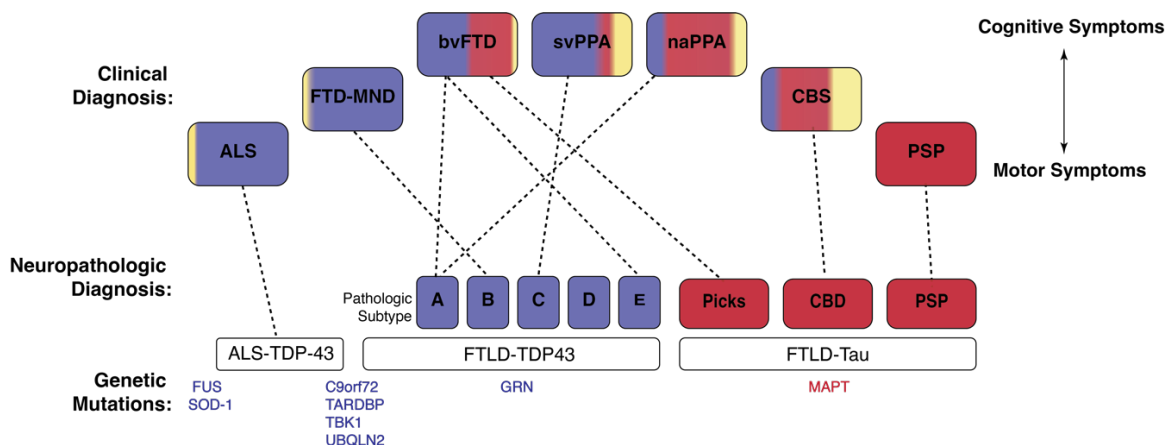
Figure 1.1. Schematic of clinicopathologic correlates in TDP-43 and Tau proteinopathies. Schema shows clinical diagnosis (top), relative frequency of associated neuropathologic subtypes (middle), and associated genetic mutations (bottom). ALS and PSP are predominantly motor syndromes; bvFTD, svPPA, and naPPA are predominantly cognitive syndromes; FTD-MND and CBS are characterized by mixed cognitive and motor symptoms. TDP-43 proteinopathies are shaded in blue, tauopathies are shaded in red, and other protein etiologies (including FUS and SOD-1 associated ALS, Alzheimer's disease, and rarer diseases) in yellow. Dashed lines represent the predominant clinicopathologic correlate. Figure adapted from [36,37]. *ALS* amyotrophic lateral sclerosis, *bvFTD* behavioral variant frontotemporal dementia, *CBD* corticobasal degeneration, *CBS* corticobasal syndrome, *FTD-MND* frontotemporal dementia-motor neuron disease, *naPPA* nonfluent/agrammatic primary progressive aphasia, *PSP* progressive supranuclear palsy, *svPPA* semantic variant primary progressive aphasia.

1.2   Neuropathologic and genetic links between ALS and FTLD

In addition to clinical overlap with FTD, ALS also shares some neuropathologic and genetic overlap with FTLD, the most neuropathologic correlate of the clinical syndrome FTD (Figure 1.1). Grossly, patients with pure FTLD may show atrophy of the frontal and/or temporal lobes accompanying cognitive or behavioral deficits. Pure ALS nervous system may show atrophy of the precentral gyrus and spinal cord anterior nerve roots or may show no gross abnormalities accompanying voluntary motor deficits. Those with an overlap of symptoms may show both patterns[38].

Microscopically, ALS spinal cord is demyelinated within the lateral corticospinal and anterior gray matter tracts. Large motor neurons of the spinal cord anterior horn, cranial neuron motor nuclei within the brainstem, and Betz cells in layer V of the motor cortex experience selective degeneration resulting in gliosis, vacuolization, and spongiosis[38]. FTLD-affected cortical gray matter show loss of pyramidal neurons of layers II/III, vacuolization, and gliosis; affected white matter shows demyelination and gliosis[1].

Early immunohistochemical studies identified ubiquitin-positive structures in both ALS and FTLD, where differentiation between ubiquitin- or tau-positive inclusions was a critical diagnostic criteria[31,39,40]. Before the introduction of ubiquitin and TDP-43 immunohistochemistry, FTLD without evidence of tau aggregates was classified as "dementia lacking distinctive histology[41]. ALS and FTLD were further linked neuropathologically with the breakthrough discovery that the RNA binding protein TDP-43 (transactivation response element DNA-binding protein 43) was the key component of these ubiquitin-positive structures in both diseases[42,43]. Approximately 97% of all ALS cases and 45% of FTLD cases involve aggregated, hyperphosphorylated TDP-43 (pTDP-43)[3,44].

In FTLD-TDP43, neuronal and glial pTDP43 inclusion pattern and biochemical profile can roughly segregate cases into subtypes[44,45] (Table 1.1). How these subtypes translate to clinical presentation or prognosis has yet to be elucidated.

Table 1.1. FTLD TDP-43 pathological subtypes

	Dystrophic Neurites	Inclusions	Pathology Depth
Type A	Short	Neuronal including ring inclusions	Superficial cortex White matter
Type B		Neuronal	Superficial and deep White matter
Type C	Long		Superficial
Type D	Short	Lentiform intranuclear	Superficial and deep
Type E		Granulofilamentous neuronal Oligodendroglial Grains	Superficial and deep White matter

Adapted from [45]

Because of shared clinical, genetic, and pathological features, FTLD is thought to exist on a spectrum with ALS[46]. Genetically, autosomal dominant mutations account for more than 10% of ALS[47]. In FTLD, up to 40% of patients have a history suggesting familial transmission, and over 10% of patients with autosomal dominantly inherited mutations[1]. Mutations in the genes such *C9ORF72* (hexanucleotide repeat expansion), *TARDBP* (encodes TDP-43)*, TBK1* (encodes TANK-binding kinase 1), and *UBQLN2* (encodes biquilin-2) are associated with TDP-43 proteinopathies in both ALS and FTLD patient cohorts. The hexanucleotide repeat expansion within the non-coding region of the *C9ORF72* gene is the most common inherited cause of both ALS and FTLD[47]. The clinical phenotype driven by these genetic lesions can be variable, but most commonly patients have bvFTD or FTD with motor neuron disease[26]. Mutations in the RNA binding protein *FUS* (encodes fused in sarcoma DNA/RNA binding protein) are not associated with TDP-43

pathology in ALS or FTLD. Likewise, *SOD1* (encodes Cu/Zn superoxide dismutase type 1) mutations do not cause TDP-43-related ALS.

Mutations in *MAPT* (microtubule associated protein, tau) cause also cause FTLD, but the key microscopic finding within these cases are aggregates of hyperphosphorylated tau within cortical and subcortical areas[2]. FTLD-tau is rarely associated with motor neuron disease, but can otherwise phenocopy FTLD-TDP43—differentiating the underlying microscopic pathology antemortem using symptomatology can be difficult[26].

Table 1.2. Most common FTLD-Tau pathological subtypes

	pTau findings
Pick's disease	3R Tau: round cytoplasmic inclusions in neurons
Progressive supranuclear palsy	4R Tau: globose neurofibrillary tangles Tufted astrocytes Predominantly brainstem pathology
Corticobasal degeneration[8]	4R tau: Astrocytic plaques Threads in gray and white matter Frontal, parietal, and striatal pathology

Adapted from [48]

1.3   The RNA binding protein ELAVL3: structure, function, and dysfunction

The ELAVL (embryonic lethal, abnormal visual system-like) family of RNA binding proteins was first identified in humans in relation to paraneoplastic neurological disorder secondary to small cell lung cancer[49,50]. In these patients, ectopic expression of family member ELAV4/HuD (anti-Human antibody antigen D) triggered production of anti-Hu antibodies and subsequent paraneoplastic encephalomyelitis. The errantly expressed HuD was homologous to the Drosophila proteins Elav, which shows conservation in vertebrates[51,52].

Structurally from N- to C-terminus, ELAVL family members have two classic RNA recognition motifs (RRMs) closest to the N-terminus, a hinge region, and one poly(A) binding RRM closest to the C-terminus[53]. ELAVL1 (HuR) is expressed ubiquitously throughout body tissues, whereas ELAVL2, ELAVL3, and ELAV4 are mostly restricted to expression in the central and peripheral nervous systems and are referred to as the neural ELAVLs (nELAVLs). There is high sequence homology between the nELAVLs (~80%) (Figure 1.2), especially within the RNA-binding domains (>90%)[54]. Regions with lowest homology include the N-terminus and the hinge domain, which are the common targets for immunolabeling.
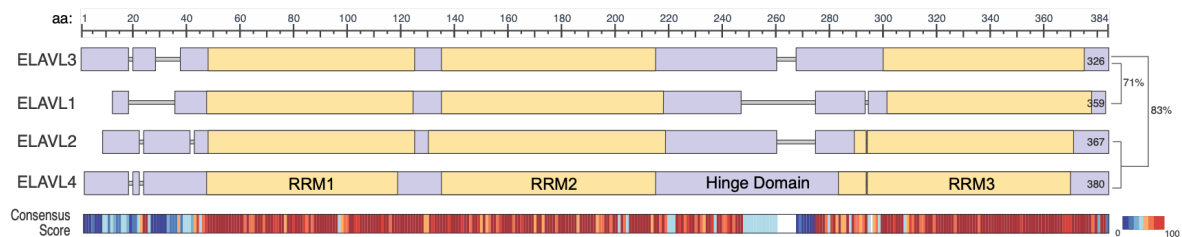
Figure 1.2. **Schematic of ELAVL protein family sequence homology**. ELAVL proteins contain 3 RNA binding domains containing RNA recognition motifs (RRM, in yellow) that are highly homologous across family members (high consensus score). The N-terminus and hinge domain are domains with the lowest sequence homology (low consensus score). ELAVL3 shares roughly 83% sequence homology with the other neurally-expressed family members, ELAVL2 and ELAVL4. Figure generated with SnapGene software.

Functionally, all three RRMs are involved in transcript stability, either through direct RNA interaction (RRM1 and 2), steric hinderance of the poly(A) (RRM3), or association with RNA stabilizing factors and ribosomal machinery (RRM3)[55]. The hinge domain is also involved in protein-protein interaction. *In vitro* data demonstrate ELAVL proteins form multimers in the presence of RNA to enhance binding[54,56]. In a HeLa cells, RRM1 and RRM2 of ELAVL3 are critical for splice regulation and the hinge domain critical for ELAVL3-

ELAVL3 protein interaction[54]. In ELAVL1, the hinge domain contains functional nuclear localization signals which allow the protein to bind target RNAs in the nucleus and shuttle them through the nuclear pore to the cytoplasm[57]. The protein is mainly found in the nucleus but can shuttle to the cytoplasm. ELAVL2 and ELAVL4 are predominantly cytosolic, whereas ELAVL3 is found in both the cytosolic and nuclear fractions[54]. Removal of the hinge domain in ELAVL3 does not change the pattern of subcellular localization in the nucleus or cytoplasm[54].

During development, nELAVL proteins are sequentially activated, indicating unique roles amongst the family members[58,59] In a study of mouse neural development, the ELAVL2 homologue *mHuB* was expressed at the earliest stage of neural development and found throughout ventricular and intermediate zones; ELAVL4 homologue *mHuD* had intermediate expression, strongest in intermediate zone; ELAVL3 homologue *mHuC* expressed predominantly and robustly in mature cortical plate neurons[60]. In adult mouse brain, mouse *mHuB* had scattered expression; *mHuC* was strongly expressed throughout the neocortex; and *mHuD* was strongest in large projection neurons within layer V. Neurons of the spinal cord predominantly expressed *mHuC.* Overall, *mHuC* had the highest expression of the family members throughout the adult brain[60].

Multiple phenotypes have been described in mouse *Elavl3* knockout models. Particular attention has been paid to cell populations that exclusively express Elavl3 so there can be no redundancy or functional compensation from family members upon *Elavl3* knockout. Cerebellar Purkinje cells and hippocampal dentate gyrus are such populations. Aged *Elavl3* null mice showed signs of progressive cerebellar ataxia, including worse performance on Rotarod, wider gait, and increased tremor[61,62]. Microscopically, cerebellar

Purkinje cells showed disrupted synaptic formation, abnormal axonal morphology, and impaired anterograde transport. Functionally, in the absence of Elavl3, there is alternative splicing shift in *AnkG* (ankyrin G), a gene that is essential for neuronal polarity[60]. In the presence of nElavl proteins, *AnkG* exon 34 is preferentially excluded. Inclusion of *AnkG* exon 34 is associated with immature neurons—mature neurons preferentially exclude this exon. With *Elavl3* knockout in cerebellar Purkinje cells, there is a shift in splicing in mature cells to include *AnkG* exon 34. Consequently, AnkG does not perform its role in creating a diffusion barrier between the soma and axon, and the cerebellar Purkinje cell loses its neuronal polarity[60]. By EEG, *Elavl3* null and haploinsufficent mice show seizure activity, which may be due to a shift in the RNA isoforms of the glutaminase, an essential enzyme for neuronal glutamate synthesis, driven by alternative splicing or by transcript stabilization and abundance level[62]. *In vitro*, *ELAVL3* knockdown results in preferential usage of proximal polyA+ sites, reduction in overall 3' untranslated region (UTR) length, and delayed differentiation into inhibitory GABAergic cells[63]. Combining these data, ELAVL3 likely functions to maintain an adult neuron phenotype through control of the abundance of particular transcript isoforms.

1.4 RNA binding protein dysfunction in motor neuron diseases and related dementias

There is substantial evidence to support disruption of RNA binding protein homeostasis as a pathomechanism in ALS, FTLD-TDP43, and FTLD-Tau. Tau is involved in the formation of stress granules—membraneless cytoplasmic organelles made from assemblies of RNA and proteins as part of the cell's response to stalled protein translation[64]. The cross-linking and eventual irreversible aggregation of deposited tau and RBPs in stress

10

granules may hinder RNA translation[65]. In addition, RBPs with essential nuclear functions like TIA1 and HNRNPA0 exit the nucleus response to stress and associate with tau in within stress granules[4].

The neuropathologic hallmark of nearly all ALS and half of FTLD cases is mislocalization of the RBP TDP-43 from the nuclear compartment and aggregation of hyperphosphorylated species in the cytoplasm within neurons and glia[3,44]. Still to be elucidated with whether loss of TDP-43 nuclear function or the presence of phosphorylated TDP-43 cytoplasmic aggregates is the main contributor to disease.

As an RBP, TDP-43 plays many roles throughout the life cycle of RNA, and loss of function could have far-reaching consequences on many targets. TDP-43 binds to nearly 30% of the transcriptome, with high affinity for UG repeats[8]. Intronic binding facilitates splice selection, generally as a splice repressor[8,66]. Binding on the 3'UTR influences mRNA stability and transport. *In vitro* data demonstrates that during cellular stress, TDP-43 is capable of assembling into stress granules that function to sequester mRNA and halt transcription[65].

Loss of TDP-43 splice function results in expression of splice variants containing non-conserved exonic sequences, "cryptic exons" (CEs)[9]. Inclusion of the CEs can introduce frameshifts, premature stop sequences, and/or premature polyadenylation sequences. There are multiple mechanisms by which these transcript variants could cause cellular disruption. Incorporation of premature stop codons upstream of the terminal exon will lead to downregulation of expression via nonsense-mediated mRNA decay pathways[67]. Introduction of an early polyadenylation sequence generates truncated transcripts[68]. Translated transcripts can generate de novo proteins with functional alterations[11].

Recent research efforts have identified two important TDP-43 targets that experience changes in splicing due to TDP-43 loss: *STMN2* (stathmin-2) and *UNC13A* (Figure 1.3). *STMN2* codes for a tubulin-binding protein involved in microtubule dynamics and is among the top twenty most enriched genes in anterior horn motor neurons; in ALS, it is significantly downregulated within these neurons[69]. Loss of TDP-43 nuclear function results in expression of frameshifted, truncated transcripts containing CE 2a produced by cryptic splicing. The truncated transcripts contain a premature stop signal as well as utilize a premature polyadenylation sequence. The truncated *STMN2* transcript has been described in cellular TDP-43 knockdown models, human ALS spinal cord and motor cortex, and human FTLD frontal cortex[10,70,71]. *In vitro,* only the premature stop signal is required to drive down expression of *STMN2*[72]. The functional consequence of CE-mediated downregulation is likely impaired axon regeneration in growth cones.
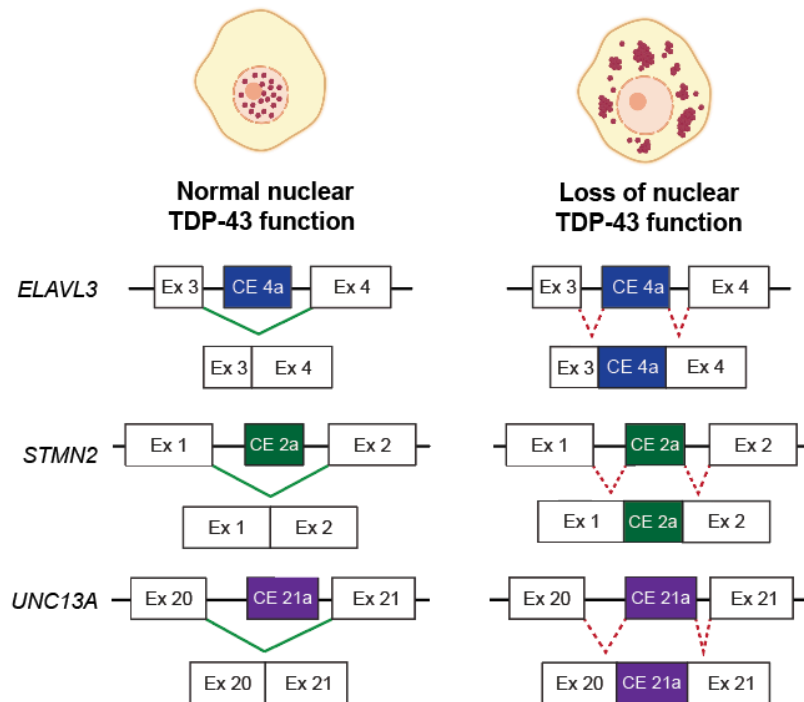
Figure 1.3. Schematic of cryptic splicing with loss of TDP-43 nuclear function. Left column demonstrates normal splicing that occurs in genes ELAVL3, STMN2, and UNC13A where cryptic exons are blocked from expression. **Figure 1.3.** Schematic of cryptic splicing with loss of TDP-43 nuclear function. **Left** column demonstrates normal splicing that occurs in genes ELAVL3, STMN2, and UNC13A where cryptic exons are blocked from expression. **Right** column demonstrates inclusions of ELAVL3 cryptic exon 4a, STMN2 cryptic exon 2a, and UNC13A cryptic exon 21a. Images created with Biorender.com

UNC13A belongs to a gene family named after *Caenorhabditis elegans Unc* gene and codes for a synaptic protein with a role in vesicle priming. Genome-wide association studies (GWAS) have routinely identified single nucleotide polymorphisms in *UNC13A* as top hits associated with ALS/FTD[73]. *In vitro* TDP-43 knockdown in iPSC-derived motor neurons and human FTLD frontal lobe demonstrated expression of CE 21a[74,75] (Figure 1.3). Improperly spliced *UNC13A* contains a premature termination sequence that likely leads to nonsense-mediated decay of transcripts containing the CE. The resulting CE-induced downregulation likely impairs synaptic function at the distal motor neuron axon.

Techniques used to detect either the *STMN2* CE and/or *UNC13A* CE include: (1) splice-aware analysis of sequencing datasets, (2) reverse transcription polymerase chain reaction (RT-PCR) coupled with Sanger sequencing to determine the transcript sequence and/or gel electrophoresis to detect size differences between amplicons containing or lacking CE sequences, (3) quantitative RT-PCR (qPCR) to measure expression level of CE-containing mRNA (4) *in situ* hybridization (ISH) of CE sequences, and (5) detection of peptides or proteins produced by CE-containing transcripts using mass spectrometry or Western immunoblotting (Figure 1.4).

ELAVL3 is another RBP implicated in ALS pathogenesis. Transcriptomic analysis of laser-captured spinal cord anterior horn motor neurons demonstrates that *ELAVL3* is consistently downregulated in these surviving neurons[5]. Analysis of whole ALS spinal cord sections also shows *ELAVL3* mRNA downregulation[5] and reduced overall immunoreactivity for ELAVL3 protein[6]. A previous study from the Ravits group demonstrated that loss of ELAVL3 from the nucleus is a common feature of ALS motor neurons—more than two-thirds of observed neurons lacked expression of nuclear ELAVL3[5]. Less than half of the observed ALS neurons showed nuclear TDP-43 loss. Two observations supported ELAVL3 nuclear displacement may occur earlier than TDP-43 pathology: (1) there were motor neurons that lacked nuclear ELAVL3, but retained normal nuclear TDP-43, and (2) with cellular stress, neuroblastoma cells experience loss of ELAVL3 from the nucleus before TDP-43. ELAVL3 also showed nuclear displacement in motor neurons from patients with familial ALS caused by mutations in *SOD1*, where there is no TDP-43 pathology.

In contrast, there is evidence to support the role of *ELAVL3* as a target mRNA of TDP-43 and, consequently, experience downstream consequences of TDP-43 loss of

nuclear function, namely cryptic splice events. There are binding sites for TDP-43 within intron 3 of the *ELAVL3*. Cellular depletion of TDP-43 causes production of *ELAVL3* containing CE 4a retained between exons 3 and 4 (Figure 1.4)[10,11]. In human, *ELAVL3* CE 4a has been identified in TDP-43 negative neuronal nuclei derived from two FTLD-TDP43 cortices with splice coordinates of hg38 chr19:11463662-11466172 and chr19:11458611-11463496[11]. Studies examining *STMN2*, *UNC13A,* and *ELAVL3* cryptic exon expression in TDP-43 depleted neural cellular models and/or human proteinopathy CNS tissue are summarized (Figure 1.4).
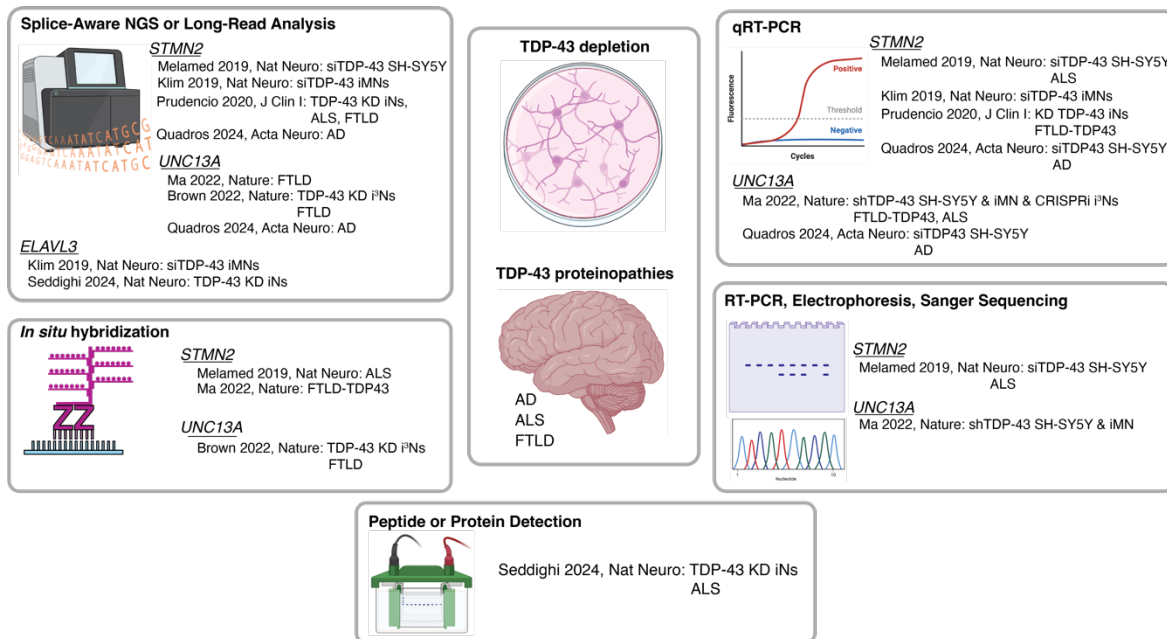
Figure 1.4. Studies identifying *STMN2, UNC13A,* and/or *ELAVL3* cryptic exons with TDP-43 dysfunction. Schematic showing recent studies that have identified cryptic exons in human neural cellular models that silence or knock-down TDP-43 and TDP-43 proteinopathy postmortem tissue from AD, ALS, or FTLD brain or spinal cord tissue. Categorized by methodology used.

In Chapter 2, we report evidence of *ELAVL3* cryptic exon (CE 4a) expression using RT-PCR, qPCR, and chromogenic *in situ* hybridization (CISH) in ALS spinal cord and motor

cortex. We confirm the reported splice junctions and show the cryptic exon sequence contains premature stop sequences that could lead to the production of truncated proteins, or more likely, doom the RNA transcripts to destruction by nonsense-mediated decay. We show expression of *ELAVL3* CE 4a is low but higher in motor cortex than spinal cord. We use CISH to visualize that CE 4a is exclusively expressed in motor neurons of the spinal cord and distributed in neurons throughout the cortical layers in motor cortex.

In chapter 3, we expand our previous neuropathic findings of ELAVL3 nuclear loss in spinal cord motor neurons. We examine level of nuclear expression and subcellular localization in ALS motor cortex as well as FTLD-TDP43 and FLTD-Tau frontal cortex. We describe normal expression patterns of ELAVL3 in motor and frontal cortex. We demonstrate reduction in ELAVL3 nuclear expression associated with the presence of intracellular protein aggregates in all diseases. We also show a pattern of reduced nuclear ELAVL3 in aggregate-containing cells, increased cells with intense granular cytoplasmic ELAVL3 staining, and ELAVL3 "balls on a string"-appearing neuropil aggregates.

CHAPTER 2: CRYPTIC MIS-SPLICING OF *ELAVL3* INTRON 3 IN ALS TDP-43 PROTEINOPATHY

2.1 Background

The mechanistic consequences of loss of TDP-43 nuclear function as an RNA binding protein (RBP) can be measured by splice perturbations in TDP-43's target genes, which comprise nearly a third of the transcriptome[9]. Generally, TDP-43 is a splice repressor; it binds to target mRNAs and represses inclusion of intronic sequences either through direct interaction with splice machinery or sterically blocking splice acceptor sites from interacting with the splice site[66]. The effects of inclusion of nonconserved exonic sequences, "cryptic exons" (CEs), can be ruinous. Within mRNA transcripts, CEs can induce frameshifts, generate premature stop or polyadenylation sequences, or create novel domains within protein coding sequences. Whether by expression of a truncated or nonfunctional protein or degradation of transcripts through nonsense mediated decay pathways, wild-type expression of genes is modulated because of the absence of TDP-43[11,67,68].

Two important targets of TDP-43 that suffer pathologic consequences with its loss are *STMN2* and *UNC13A*. *STMN2* is highly expressed in motor neurons of the spinal cord anterior horn and plays a critical part in maintaining the health of the long axons of these neurons[76]. When disturbed *in vitro*, motor neurons experience deficits in neurite and axon growth; after axon injury, regrowth is severely impacted[10]. When lost in mice, there are disturbances in axoplasm structure and axonal caliber driving tears in myelin layers; as a result, mice experience progressive motor deficits and muscle denervation[76]. With loss of nuclear TDP-43, cryptic splice and polyadenylation sites within intron 1 are utilized, and the resulting transcripts are truncated after CE 2a (Figure 1.3). The premature stop sequence

within CE 2a drives suppression of stathmin-2 protein within spinal cord motor neurons[72]. Expression of *STMN2* CE 2a with TDP-43 nuclear loss has been established *in vitro* and in *STMN2*-humanized murine models[10,72]. It has also been found in human TDP-43 proteinopathy CNS tissue, including ALS, FTLD-TDP43, and Alzheimer's disease (AD)[70,71,77]. As a result, protein STMN2 levels decrease in spinal cord/motor cortex, frontal/temporal cortex, and limbic regions, respectively.

UNC13A codes for a synaptic protein essential for calcium-triggered synaptic vesicle release, critical in signaling[78]. When disturbed in mice, action potential-induced neurotransmitter release from glutamatergic presynaptic terminals is mostly blocked[75]. Its pathogenic role in TDP-43 proteinopathies was suspected due to GWAS highlighting *UNC13A* as a high risk loci highly associated with ALS and FTD[73]. Absence of TDP-43 binding allows inclusion of CE 21a, which contains a premature termination sequence, likely dooming the transcript to nonsense mediated decay[67,68]. Strengthening the pathogenic role of UNC13A mis-splicing, high risk SNPs in *UNC13A* were found to promote inclusion of CE 21a[75]. Expression of *UNC13A* CE 21a has been shown *in vitro* and in human postmortem TDP-43 proteinopathy tissue, including ALS, FTLD-TDP43, and AD[74,75,77].

ELAVL3, a target of TDP-43 binding, is also an RBP. It contains binding domains for both TDP-43 and neurally-expressed ELAVL-family members (nELAVL) within intron 3 (Figure 2.1A). Like TDP-43, ELAVL3 also can function as a splice repressor, like when it binds *AnkG* to preferentially exclude exon 34 and create a transcript isoform associated with mature neurons[60]. When TDP-43 activity is lost *in vitro*, either by siRNA-induced knockdown of TDP-43 protein expression in human embryonic stem cells differentiated into motor neurons or by generating human motor neurons with induced pluripotent stem cells

derived from patients with TDP-43 mutations, *ELAVL3* expression significantly decreases and transcript isoforms containing CE 4a are detected[10] (Figure 2.1B). These data provide mechanistic evidence that TDP-43 acts as a splice repressor to block CE 4a expression. Intriguingly, we have provided evidence of ELAVL3 nuclear loss in ALS spinal cord motor neurons[5], and given there is a potential ELAVL3 binding site within intron 3 between canonical exon 3 and CE 4a, we cannot exclude the possibility that ELAVL3 dysfunction may drive some expression of its own CE sequence.

Prior to our study, expression of *ELAVL3* CE 4a in human tissue was identified in a single study that analyzed a dataset from human FTLD frontal cortex neuronal nuclei[11]. In three individuals, neuronal nuclei that did not contain TDP-43 expressed *ELAVL3* CE 4a with splice coordinates hg38 chr19:11463662-11466172 and chr19:11458611-11463496[11]. Given the known decrease of *ELAVL3* expression in ALS anterior horn motor neurons, we hypothesized that *ELAVL3* CE 4a was expressed in ALS spinal cord and motor cortex. We used three methods to detect expression (Figure 2.1A): (1) RT-PCR and Sanger sequencing to confirm the splice junction sequences previously reported in human tissue; (2) qPCR measurement of *ELAVL3* CE 4a expression levels; and (3) chromagenic *in situ* hybridization (CISH) to spatially localize CE 4a expression. Using these experimental approaches, we confirm expression of *ELAVL3* CE 4a in ALS spinal cord and motor cortex. Given the inserted sequence creates a premature stop sequence, we hypothesize *ELAVL3* expression in TDP-43 proteinopathies is driven down, in part or whole, because of CE 4a expression.

2.2 Results

2.2.1 *ELAVL3* structure and cryptic exon 4a sequence

Because there was a slight mismatch in reported length of the inserted *ELAVL3* cryptic exon *in vitro* (163 nucleotides)[10] and in human TDP-43 negative nuclei (166 nucleotides)[11]. We designed primers to amplify a short segment of RNA containing either the junction of canonical exon 3 and the 5' end of CE 4a or the junction of the 3' end of CE 4a and canonical exon 4 (Figure 2.1A-B, Table 2.4). Amplicons generated from ALS spinal cord RNA were size-selected, cloned, and Sanger sequenced. We confirmed the splice sites reported in human FTLD TDP-43-negative neuronal nuclei[11] were correct; *ELAVL3* cryptic exon 4a (hg38 chr19:11463662-11463496) inserts 166 nucleotides into mRNA transcripts, creating a frameshift and multiple premature stop sequences (Figure 2.1C).
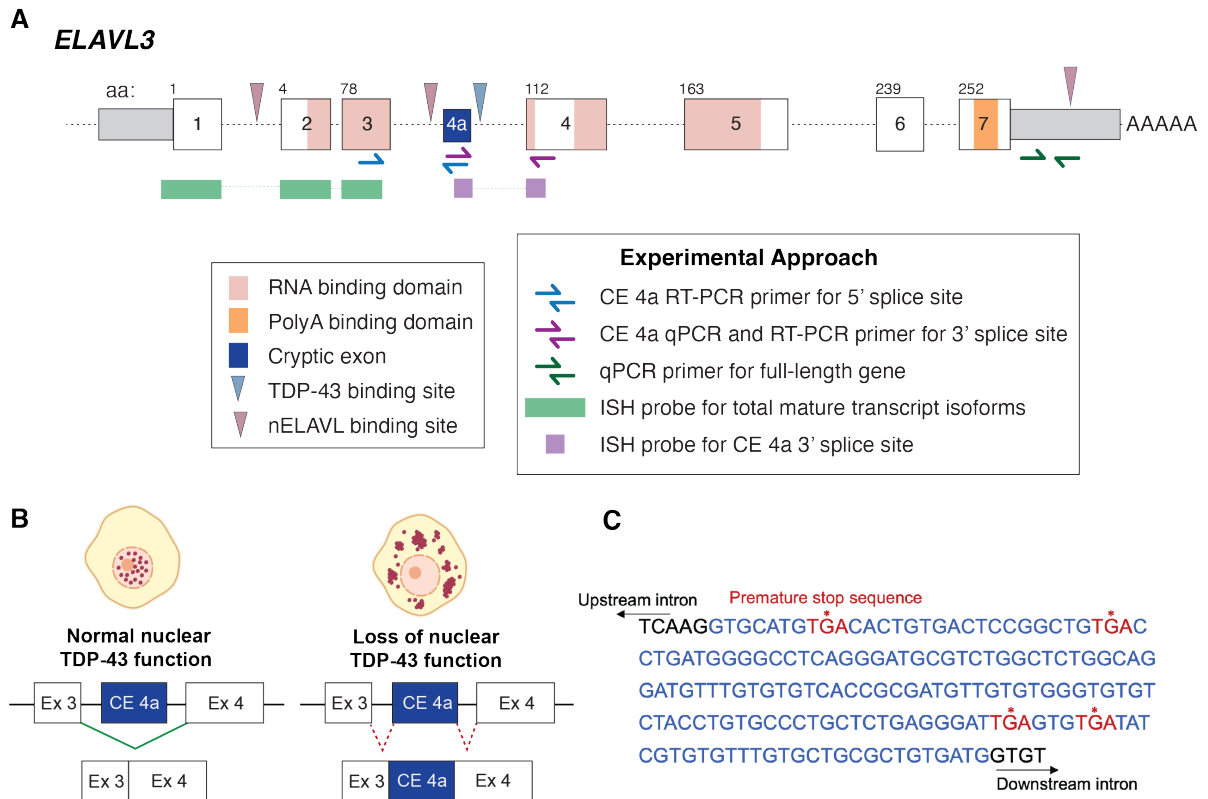
Figure 2.1. *ELAVL3* cryptic exon inclusion. (**A**) Schematic of *ELAVL3* mRNA and experimental methods for detection. TDP-43 and neurally-expressed ELAVL-family (nELAVL) member binding sites flank the sequence for cryptic exon 4a. (**B**) Schematic of *ELAVL3* cryptic exon splicing with loss of TDP-43 nuclear function. Left: with normal TDP-43 nuclear function, cryptic exon 4a is excluded. Right: with loss of TDP-43 from the nucleus, cryptic exon 4a is included within transcripts. Adapted from Figure 1.3. (**C**) Sanger sequence of *ELAVL3* cryptic exon 4a (blue), including multiple premature stop sequences (red).

2.2.2 Expression of ELAVL3 cryptic exon 4a and STMN2 cryptic exon 2a in ALS patient spinal cord and motor cortex

We utilized our repository of short postmortem interval ALS and control CNS tissue (Table 2.2) to measure the expression of *ELAVL3* and *ELAVL3* CE 4a using RT-qPCR. In the spinal cord, we selected regions in ALS cases with preserved numbers of motor neurons, reasoning that early molecular events at the neuronal level were more likely to be identified in regions of the nervous system with the highest numbers of residual motor neurons[79].

We re-confirmed our previous data[5] demonstrating downregulation of *ELAVL3* in ALS spinal cord, and we expanded these findings into motor cortex to show reduced *ELAVL3* mRNA in ALS relative to controls (Figure 2.2A). In both regions, *ELAVL3* is reduced by roughly 80% in ALS relative to controls. Our previous spinal cord study showed roughly 65% reduction in ALS relative to controls using qPCR and bulk spinal cord tissue[5].

Next, we used primers to detect expression of a small segment of RNA containing the 3' end of *ELAVL3* CE 4a and the 5' end of canonical exon 4 (Figure 2.1A). Within our cohort, we detected this segment in 43% of ALS spinal cord and 77% of ALS motor cortex samples (Figure 2.2B, Table 2.1). In ALS spinal cord, expression of transcripts containing CE 4a was very low relative to total *ELAVL3* mRNA (range: 0.0001-0.015-fold lower). In contrast, in the motor cortex, CE 4a is expressed at a level slightly higher than total splice *ELAVL3* transcripts (range: 1.0908 to 1.6537-fold higher). There is no correlation between spinal cord and motor cortex expression in any of our measured transcripts (Supplemental Figure S1). *ELAVL3* CE 4a was expressed significantly higher in ALS motor cortex relative to spinal cord ($P = 0.0005$).

We detected *ELAVL3* CE 4a in 2/15 control spinal cord cases (13%) but not in motor cortex tissue (Table 2.1). We do not anticipate spinal cord damage within these tissues, but these control cases were in the upper quartile of age within the control group (82 and 76 years versus a control mean of 62 years). In these samples, CE 4a was expressed at levels comparable to ALS cases. Using RT-PCR and primers detecting the junction between exon 3 and CE 4a, we confirmed expression of the cryptic exon in ALS samples as well as a control sample (case 65) that was positive for the cryptic exon by qPCR (Figure 2.2C). We also used primers generating amplicons from the 5'UTR to exon 4; amplicons containing

CE 4a were size separated from shorter wild-type amplicons imaged to demonstrate expression of long CE 4a-containing fragments in ALS spinal cord.

Given the evidence that *STMN2* cryptic exon 2a is expressed in ALS spinal cord, we explored whether our cohort of samples, some of which express *ELAVL3* CE 4a, also express other TDP-43-related cryptic exons. To detect full-length *STMN2*, we used primers that detect a short segment of the 3'UTR. To detect *STMN2* CE 2a, we used primers that detect the junction of canonical exon 1 and cryptic exon 2a (Table 2.4). In spinal cord, full-length *STMN2* was reduced by more than 90%, and in motor cortex it is reduced by 70% (Figure 2.3A). We detected *STMN2* CE 2a in 93% of ALS spinal cords (n=28/30) and motor cortices (n=14/15) and in no control cases (Figure 2.3B). We detected expression of both *ELAVL3* CE 4a and *STMN2* CE 2a in 12/30 ALS cases within our cohort (Figure 2.3C); the level of expression between the two genes is poorly correlated (r^2=0.2573 with outliers removed) (Figure 2.3D). Only one ALS case within our cohort expressed neither cryptic exon (case 87), and this case had moderate to severe motor neuron loss in the region we examined.
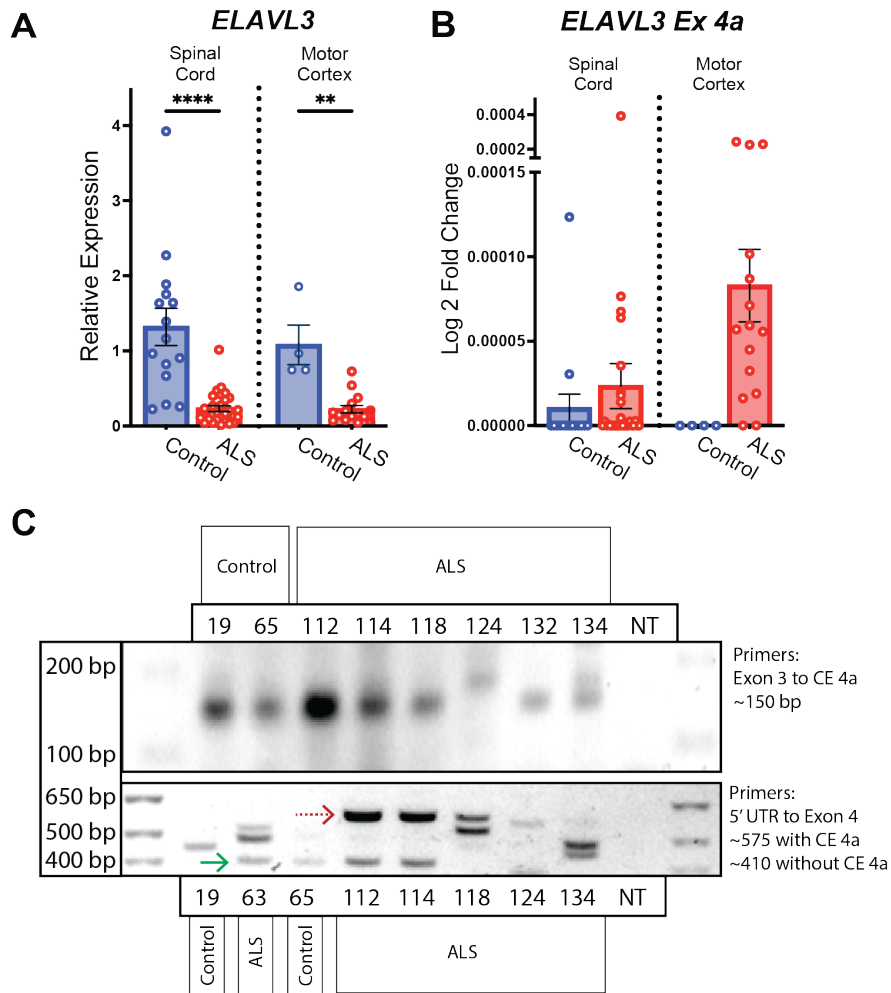
Figure 2.2. ELAVL3 CE 4a expression in ALS spinal cord and motor cortex by qPCR. (**A**) qPCR demonstrating higher expression of ELAVL3 mRNA in controls versus ALS in spinal cord (****$P<0.0001$) and motor cortex (**$P=0.0084$). Spinal cord control n = 15, ALS = 29. Motor cortex control n = 4, ALS = 15. (**B**) qPCR demonstrating cryptic exon 4a expression at low levels in ALS spinal cord and motor cortex. Spinal cord control n = 15, ALS = 30. Motor cortex control n = 4, ALS = 15. Data graphed as mean ± SEM and analyzed with Mann-Whitney tests. (**C**) **Top**: RT-PCR using primers designed to amplify a ~150 base pair segment containing the junction of exon 3 and cryptic exon 4a. Control cases 19 and 65 were positive for the cryptic exon by qPCR. **Bottom**: RT-PCR using primers designed to amplify a region from the 5'UTR to exon 4. If no cryptic exon is present, the amplicons are ~410 nucleotides (NTs), and with cryptic exon, amplicons are ~575 NTs. NT is a no-template control.
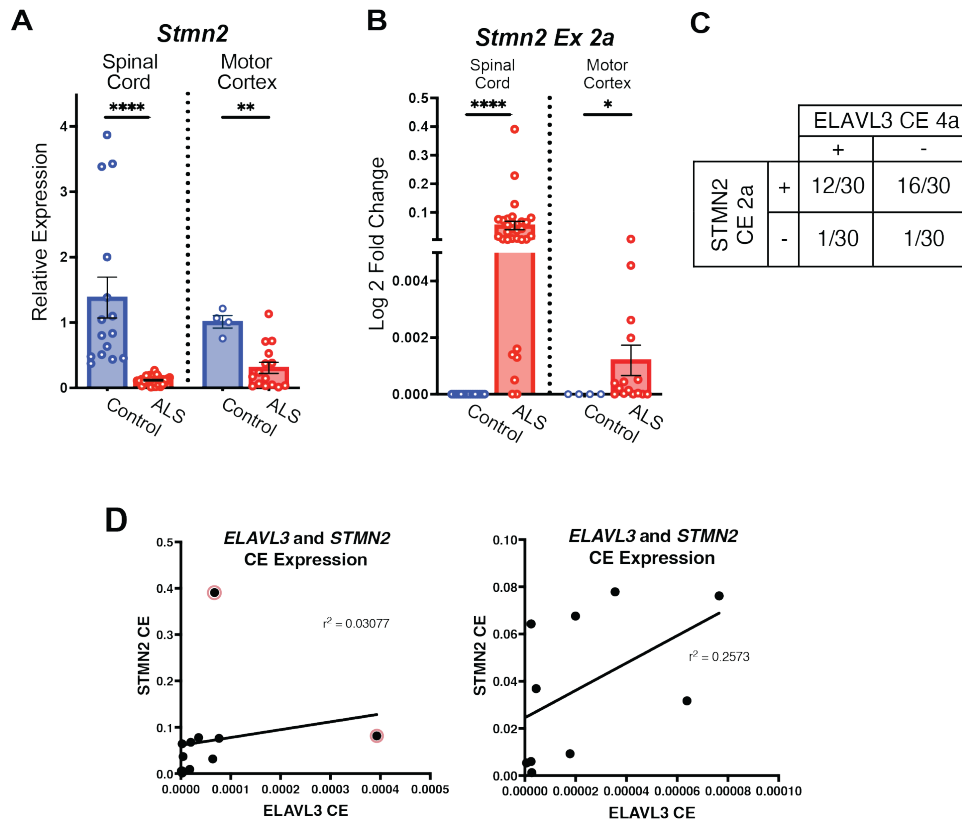
Figure 2.3. *STMN2* **CE 2a expression in ALS spinal cord and motor cortex by qPCR.** (**A**) qPCR demonstrating higher expression of *STMN2* mRNA in controls versus ALS in spinal cord (****P<0.0001) and motor cortex (**P=0.0036). Spinal cord control n = 15, ALS = 30. Motor cortex control n = 4, ALS = 15. (**B**) qPCR demonstrating *STMN2* cryptic exon 2a expression is reduced ALS spinal cord (****P<0.0001) and motor cortex (*P=0.0134). Spinal cord control n = 15, ALS = 30. Motor cortex control n = 4, ALS = 15. Data graphed as mean ± SEM and analyzed with Mann-Whitney tests. (**C**) Table of ALS spinal cord positive or negative for *ELAVL3* CE 4a and/or *STMN2* CE 2a. (**D**) **Left**: comparison of qPCR expression of the *ELAVL3* CE and the *STMN2* CE shows no linear correlation with two outliers highlighted in red. **Right**: With outliers removed, the linear correlation between expression remians weak.

2.2.3   Spatial expression of *ELAVL3* exon 4a and *STMN2* exon 2a in ALS spinal cord and motor cortex

To visualize expression of *ELAVL3* transcript variants, we performed chromogenic

in situ hybridization (CISH) using the BaseScope™ v2-RED assay. To detect total *ELAVL3*

RNA, we used a probe targeting a 300 base-pair region containing exons 1, 2, and 3; to

detect *ELAVL3* CE 4a, we used a probe that targets a 50-nucleotide RNA sequence containing the junction of exon 4a and exon 4 (Figure 2.1A, Table 2.5). We utilized formalin-fixed, paraffin embedded (FFPE) spinal cord and motor cortex sections from regions in ALS cases with preserved numbers of motor neurons[79]. We anticipate our signal was reduced in comparison to assays using frozen tissue because of RNA degradation associated with fixation. However, preservation of tissue morphology for microscopic observation is unmatched in FFPE tissue. The threshold of detection for semi-quantitation of this assay is 1 locus in 20 target cells.

We detect *ELAVL3* RNA loci in anterior horn motor neurons, small interneurons and bipolar neurons of the anterior horn, small interneurons of the posterior horn, and oligodendrocytes of white matter tracts (Figure 2.4). *ELAVL3* loci were found in nuclei, somas, and occasionally in proximal neurites. In ALS spinal cord, there were significantly fewer motor neurons positive for *ELAVL3* RNA loci compared to controls (Figure 2.5A-B), matching our qPCR observations. In controls, 68% of motor neurons contain 4 or more *ELAVL3* loci compared to 41% of motor neurons in ALS.

When probing for *ELAVL3* CE 4a, we found 46% of ALS spinal cord were positive for expression (Figure 2.6, Table 2.1). Although we detected loci in the cytoplasm, CE 4a loci were more common in the nucleus—a hint that nonsense mediated decay may be destroying transcripts that exit the nucleus. We did not detect *ELAVL3* CE 4a loci in glia of white matter tracts or in posterior horn neurons. When probing in the motor cortex, we found 67% of our ALS motor cortex cohort was positive for *ELAVL3* CE 4a (Table 2.1). The majority of Betz cells we observed did not show CE expression, which may be due to the low sampling number of these sparse cells. We did, however, identify one case that had

multiple Betz cells expressing *ELAVL3* CE 4a, all in the nucleus (Figure 2.7 A-D). In addition, we identified many examples of small neurons in superficial and deep layers with *ELAVL3* CE loci (Figure 2.7 E-J).

We also tested the sensitivity of our assay to detect changes in *STMN2* expression in ALS spinal cord and motor cortex. To detect the full-length protein, we used a CISH probe that targeted 300 nucleotides of the 3'UTR; to detect cryptic exon 2a, we used a probed targeting a 50-nucleotide sequence containing the junction of canonical exon 1 and CE 2a (Table 2.5). In ALS spinal cord, we detected reduction of *STMN2* loci in spinal cord (Figure 2.8A-B). We found an average of 40% of motor neurons do not have *STMN2* loci compared to only 6% in the control group. This assay also captures the high expression of *STMN2*— over 60% of motor neurons contain 10 or more *STMN2* loci. We detected expression of *STMN2* CE 2a in roughly one-quarter of ALS spinal cord motor neurons (Figure 2.8C-D). We did not detect *STMN2* CE 2a loci in small interneurons or bipolar neurons of the anterior horn, neurons of posterior horn, or glia of the white matter tracks. Distribution of *STMN2* CE 2a in ALS motor cortex is also reminiscent of *ELAVL3* CE 4a—loci were predominantly distributed in smaller neurons of both superficial and deep layers.

Because we assume loss of TDP-43 nuclear activity generates both *ELAVL3* CE 4a and *STMN2* CE 2a, we hypothesized that there would be a strong concordance between expression of the two molecules within neurons. For simultaneous detection of loci from the two cryptic exons, we used the chromogenic BaseScope™ Duplex Assay, which uses Fast Red development for its primary channel (*ELAVL3* CE) and Fast Green for its secondary channel (*STMN2* CE). We anticipated the second channel to be less sensitive, as there were fewer amplification steps. In the spinal cord, we observed high concordance of

expression between the CEs (Figure 2.9). In all motor neurons where we detected *ELAVL3* CE, we also detected *STMN2* CE. The expression of *ELAVL3* CE 4a was very high with the duplex assay relative to the single-channel assay (Figure 2.6). We do not believe this high expression is a technical artifact as we observed motor neurons with no staining within the same microscopic field (Figure 2.9A', C), and we did not observe staining in posterior horn neurons. Given the high expression of *ELAVL3* CE loci relative to *STMN2* CE loci and our qPCR data which indicates *STMN2* CE 2a is expressed much higher than *ELAVL3* CE 4a, we hypothesize the second channel has a lower sensitivity than the primary channel in this assay.

In the motor cortex, we observed CE loci distributed in superficial and deep cortical layers (Figure 2.10A). We visualized Betz cells and small neurons with both *ELAVL3* CE 4a and *STMN2* CE 2a loci (Figure 2.10B-B''''). We also visualized Betz cells and other neurons in the gray matter expressing either *ELAVL3* CE 4a (Figure 2.10C-C'''') or *STMN2* CE 2a (Figure 2.10D-D''''). We did not visualize loci in white matter or glial cells in the gray matter.
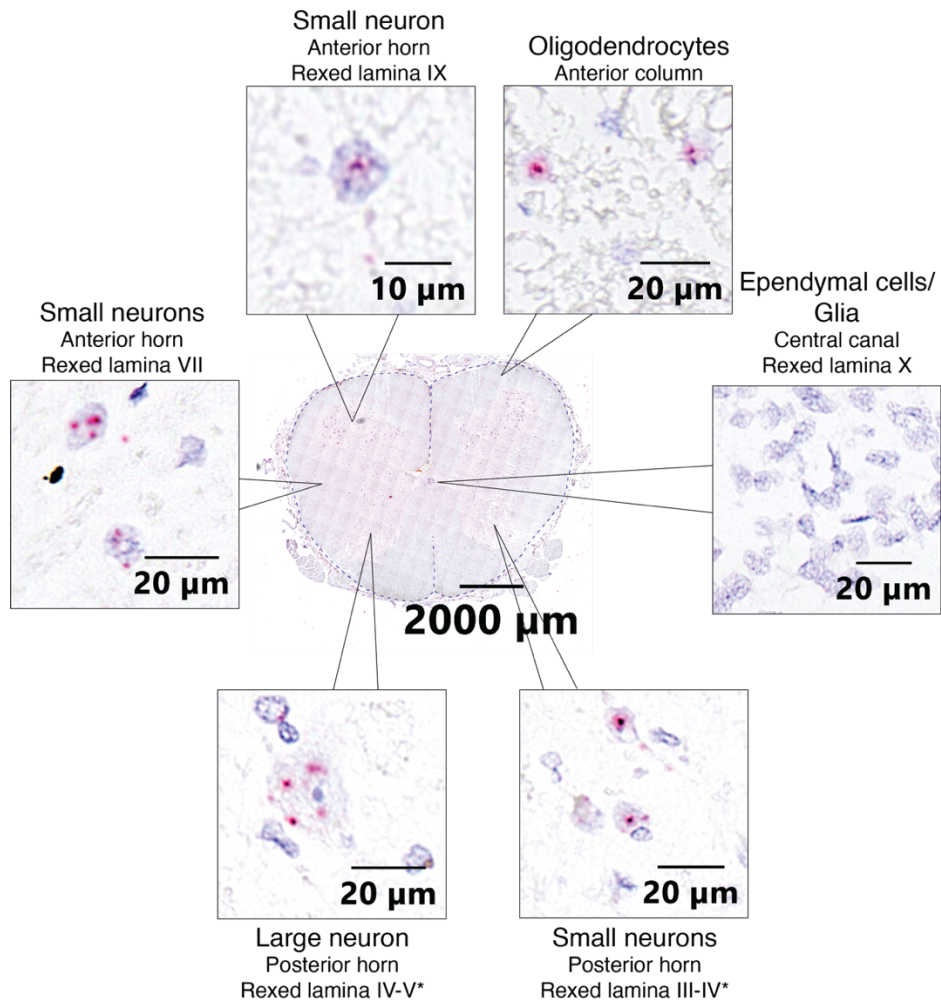
Figure 2.4. *ELAVL3* **spatial distribution in lumbar spinal cord.** *ELAVL3* is expressed in small and large neurons throughout the lamina of the anterior and posterior horns. It is also expressed in oligodendrocytes of the white matter tracts. *ELAVL3* is not expressed in the ependymal cells and neuroglia of the central canal. Signal in red, counterstain in purple. *Estimation of posterior horn Rexed lamina layer.

ELAVL3 Loci in SPC
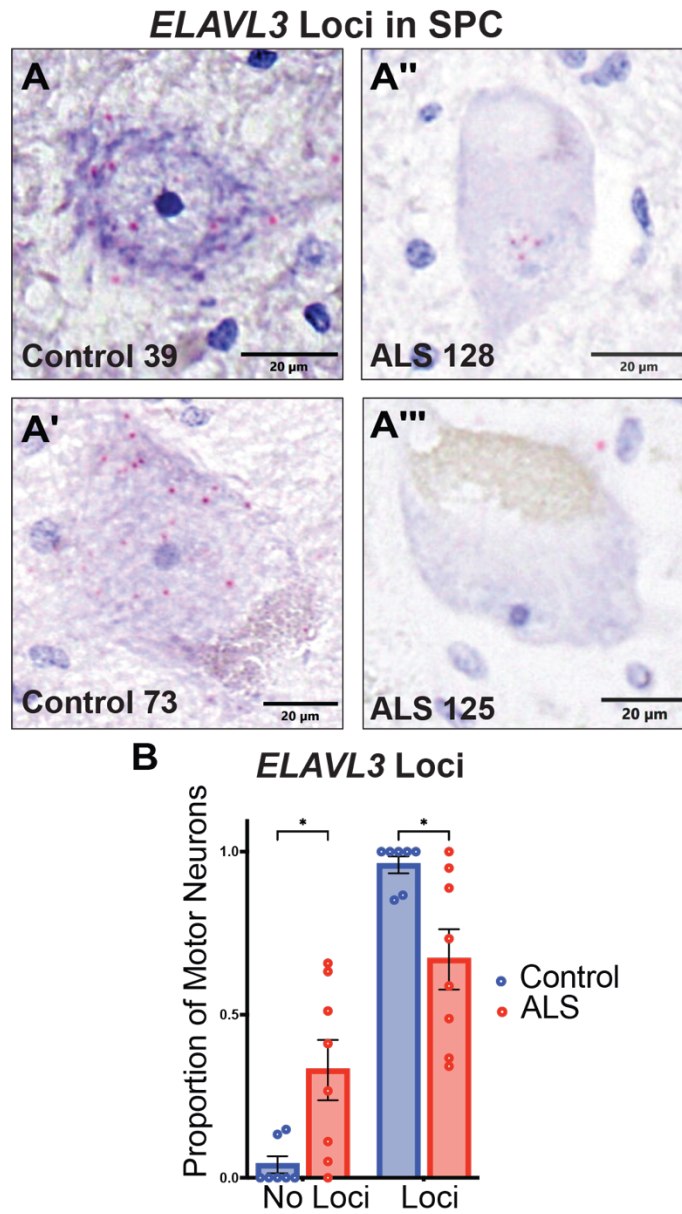
Figure 2.5. *ELAVL3* downregulation by CISH. (**A-A'''**) Representative images of *ELAVL3* mRNA loci in motor neurons of the spinal cord anterior horn. Signal in red, counterstain in purple. (**B**) Quantification showing the proportion of motor neurons with measured *ELAVL3* loci was significantly higher in controls (mean = 0.9600) compared to ALS (mean = 0.6698, *P = 0.03969) controls n=7, ALS n=8. Data graphed as mean ± SEM and analyzed with Mann-Whitney tests.
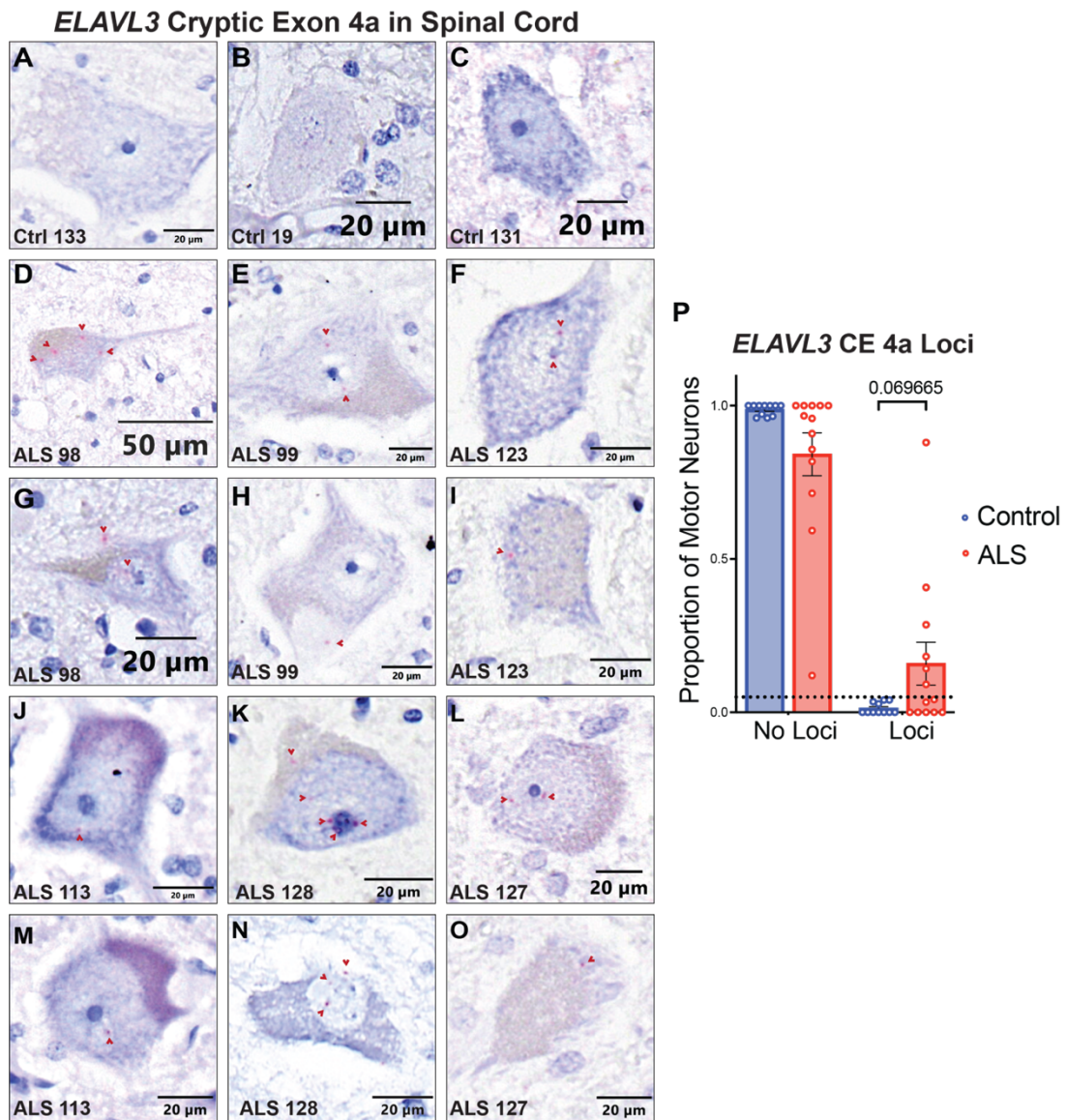
Figure 2.6. *ELAVL3* **CE 4a spatial expression in ALS spinal cord motor neurons.** (**A-C**) Representative images of control motor neurons without loci. (**D-O**) Representative images of ALS motor neurons with *ELAVL3* CE 4a loci. Signal in red and highlighted with red arrowhead, counterstain in purple. (**P**) Quantification showing of the proportion of motor neurons positive for *ELAVL3* CE 4a loci in ALS (mean 0.1587) trends higher than controls (mean 0.0129) ($P = 0.069665$). Only ALS cases showed loci expression above the threshold of detection (1 locus per 20 target cells). Data graphed as mean ± SEM and analyzed with Mann-Whitney tests.

ELAVL3 Cryptic Exon 4a in Motor Cortex
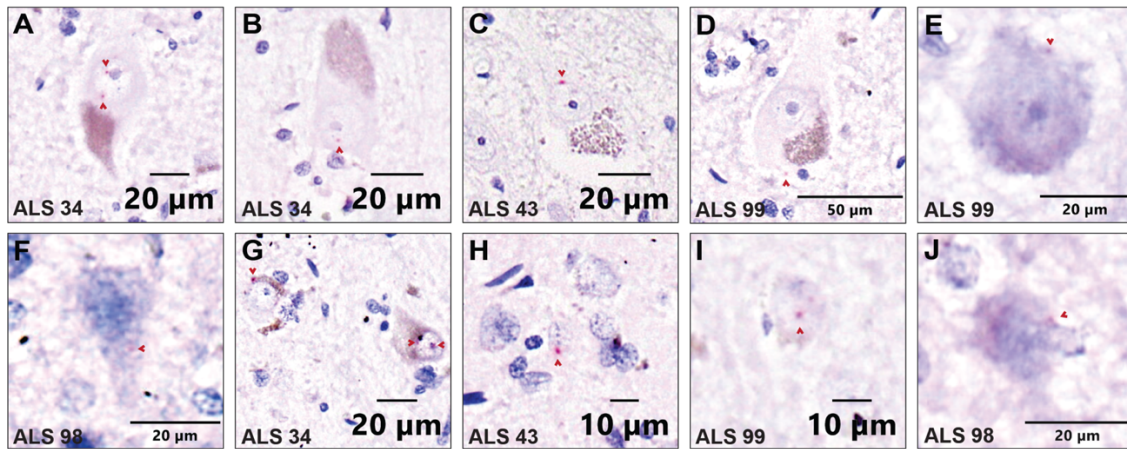
Figure 2.7. *ELAVL3* **CE 4a spatial expression in ALS motor cortex cells (A-E)** Representative images of Betz cells in ALS motor cortex with ELAVL3 CE 4a nuclear loci. (**F-J**) Small neurons in ALS motor cortex with ELAVL3 CE 4a loci. Signal in red highlighted by red arrowhead, counterstain in purple.
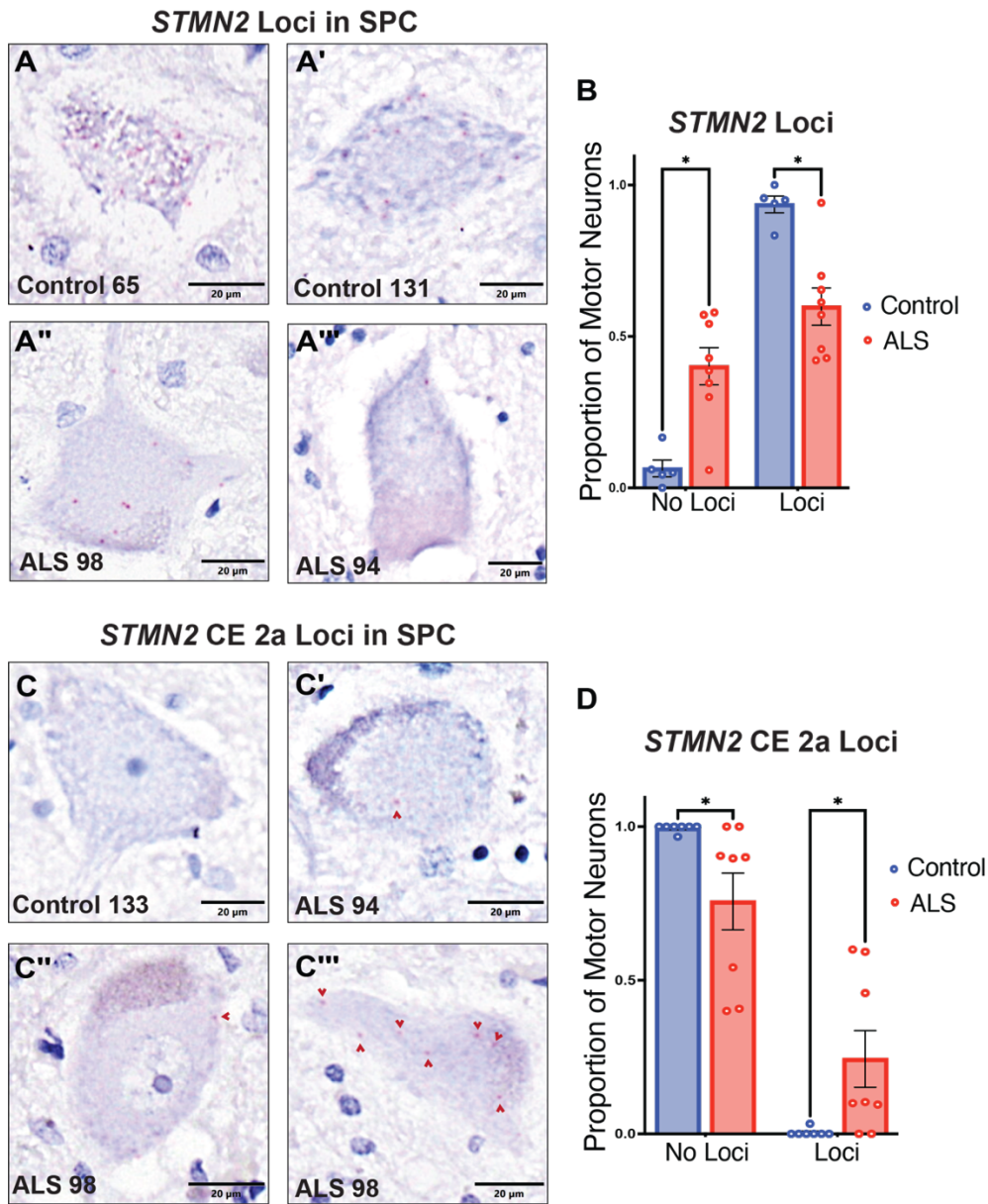
Figure 2.8. *STMN2* **downregulation and** *STMN2* **CE 2a expression by CISH.** (**A**) Representative images of chromogenic in situ hybridization (ISH) detecting *STMN2* loci in control (**A-A'**) and ALS (**A"-A'''**) anterior horn lower motor neurons. Signal in red, counterstain in purple. (**B**) The proportion of motor neurons with measured *STMN2* loci was significantly higher in controls (mean = 0.9358) compared to ALS (mean = 0.5984, *P = 0.012393), controls n = 5, ALS n = 8. (**C-C'''**) Representative images of ISH detecting alternatively spliced *STMN2* RNA containing an exon 1-exon 2a junction, which is absent in control motor neurons (**C**) and found in ALS spinal cord anterior horn motor neurons (**C'-C'''**). Signal in red and highlighted with red arrowhead, counterstain in purple. (**D**) The proportion of motor neurons with measured *STMN2* CE 2a loci was significantly higher in ALS (mean = 0.2437) compared to controls (mean = 0.0047, *P = 0.021330), controls n = 7, ALS n = 8). Data graphed as mean ± SEM and analyzed with Mann-Whitney tests.

ELAVL3 CE 4a and STMN2 CE 2a Loci in Spinal Cord
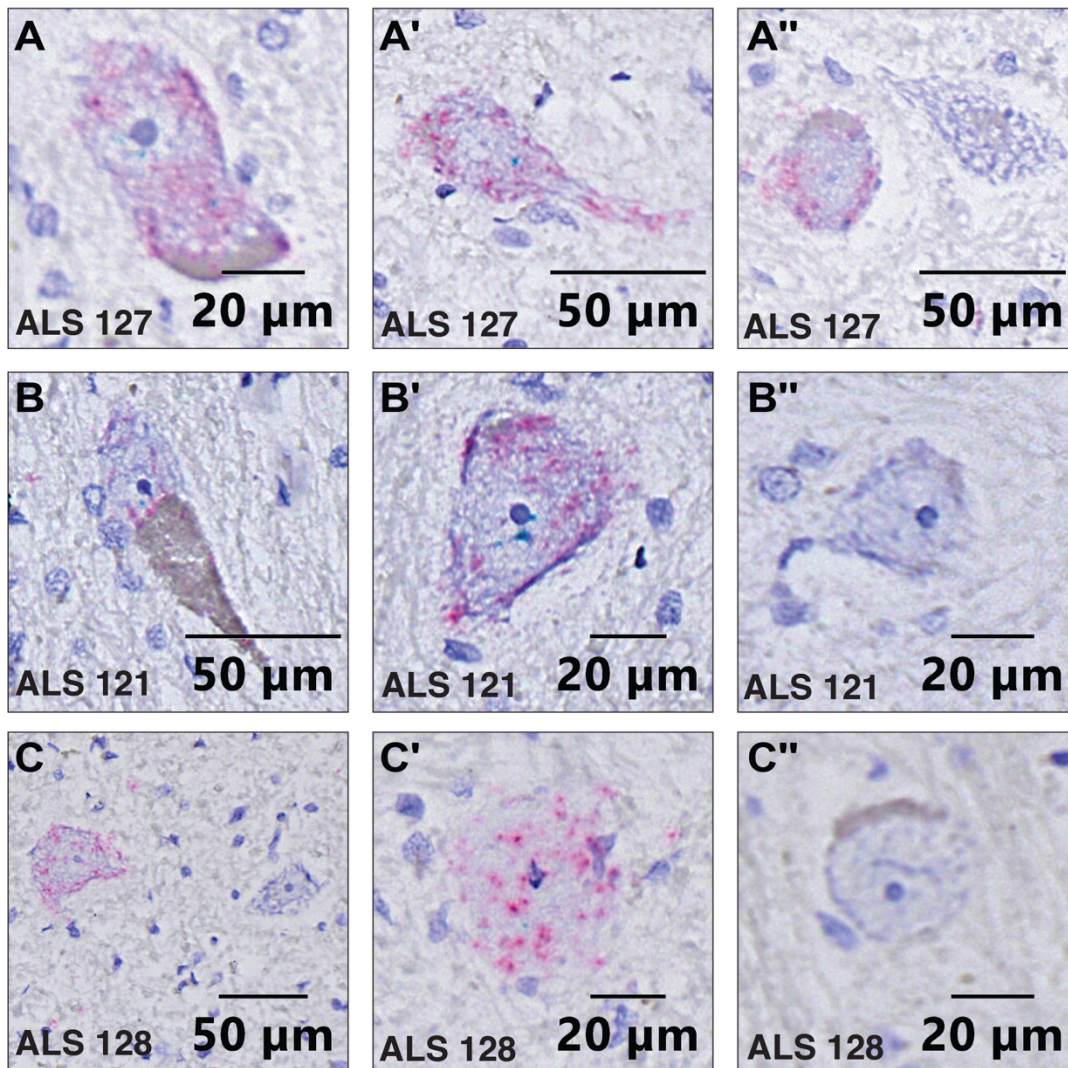
Figure 2.9. Visualization of *ELAVL3* and *STMN2* cryptic exons co-expression in ALS spinal cord motor neurons. (**A-C''**) Representative images from three ALS spinal cords showing motor neurons with expression of both *ELAVL3* CE 4a (red) and *STMN2* CE 2a (blue) in some motor neurons, but not all (A'', B'', C''). Counterstain in purple.
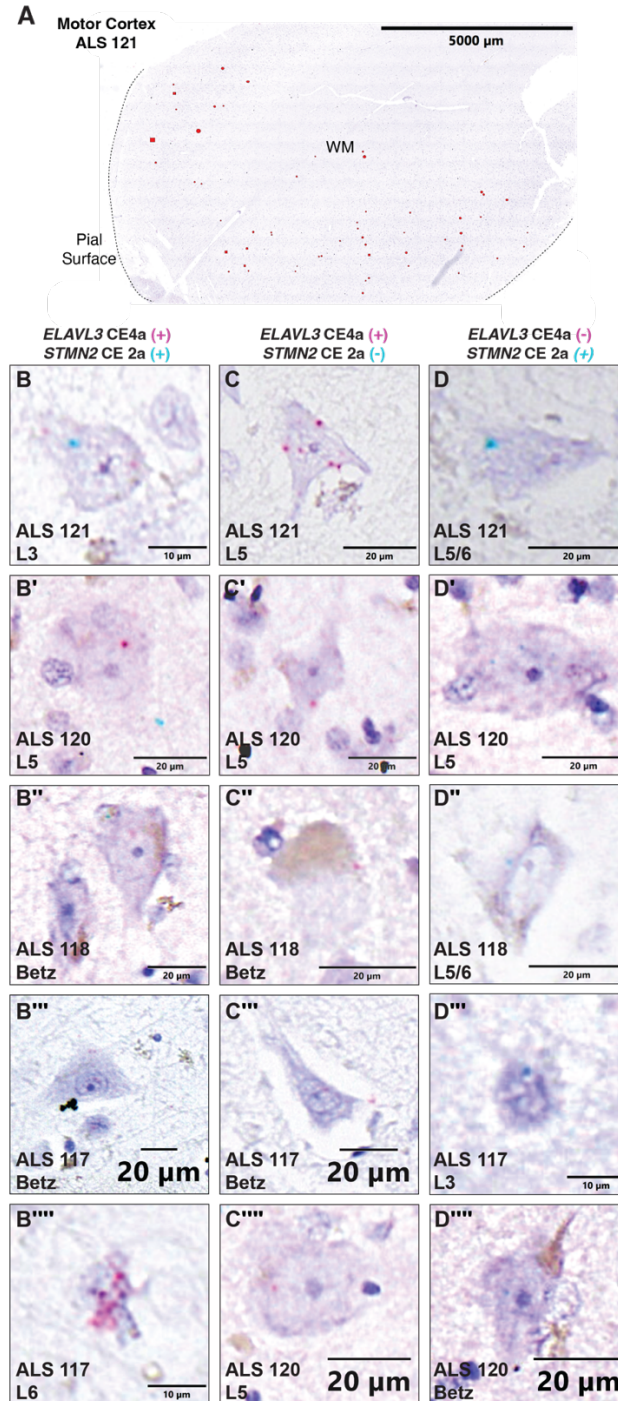
Figure 2.10. Visualization of *ELAVL3* and *STMN2* cryptic exon co-expression in ALS motor cortex (**A**): Low magnification image of motor cortex demonstrating distribution of CE-containing cells, highlighted in red. Pial surface drawn with dotted line, WM = white matter. Counterstained with hematoxylin. (**B-B''''**) Representative images of cortical cells with both *ELAVL3* CE 4a (red) and *STMN2* CE 2a (blue). (**C-C''''**) Representative images of cortical cells expressing *ELAVL3* CE 4a (red) only. (**D-D''''**) Representative image of cortical cells expressing only *STMN2* CE 2a (blue).

Table 2.1: Ratio of cases positive for *ELAVL3* cryptic exon 4a using different experimental modalities.

	RT-PCR			*In Situ*	
Diagnosis	Spinal Cord	Motor Cortex	Diagnosis	Spinal Cord	Motor Cortex
Control	2/15 (13.3%)	0/5 (0%)	Control	0/11 (0%)	0/3 (0%)
ALS	13/30 (43.4%)	7/9 (77.8%)	ALS	6/13 (46.2%)	4/6 (66.7%)

2.3. Discussion

In TDP-43 proteinopathies, loss of TDP-43 nuclear function results in expression of previously repressed CEs in its binding targets and often subsequent reduction in target protein levels. Reduction of the RBP ELAVL3 in the motor neurons of the spinal cord is a hallmark of ALS[5,6]. *ELAVL3* has binding intronic binding sites for TDP-43. Taking advantage of the heterogenous sites of onset between ALS cases, we were able to evaluate expression of *ELAVL3* CE 4a in regions with preserved numbers of motor neurons.

We confirmed *ELAVL3* CE 4a in ALS spinal cord has the splice coordinates reported in FTLD-TDP43 frontal cortex (hg38 chr19:11463662-11466172 and chr19:11458611-11463496)[11]. The inserted 163-nucleotide CE sequence creates a frameshift and a premature stop sequence within the first ten nucleotides. Given that ELAVL3 mRNA and protein expression is significantly downregulated in ALS anterior horn motor neurons, we hypothesize that expression of CE 4a-containing transcripts and subsequent destruction of those transcripts via non-sense mediated decay reduces expression of ELAVL3 protein in TDP-43 proteinopathy tissues, similar to what has been reported for *UNC13A* and *STMN2*.

We are confident that *ELAVL3* CE 4a is a common feature of TDP-43-related ALS. When ALS spinal cord and motor cord was interrogated with RT-qPCR, we detected *ELAVL3* CE 4a in 43% and 77%, respectively. A recent student examining CE expression in human frontal cortex TDP-43 negative nuclei found 43% of their cases (3/7) showed *ELAVL3* CE 4a[11]. Our detected expression levels of *ELAVL3* CE 4a are low, though significantly higher in the motor cortex than spinal cord; this may be explained by increased transcript production or differences in speed of nonsense-mediated decay. We do not have evidence of translation of truncated peptides, predicted at ~12 kDa, either by -omics in TDP-43 *in vitro* knockdown[11] or by immunoblotting with an antibody that targets an N-terminal epitope and is theoretically capable of detecting this peptide (Chapter 3, Figure 3.12).

Using CISH, we demonstrated that, in the spinal cord, *ELAVL3* CE 4a is exclusively expressed in spinal cord motor neurons of the anterior horn. It was not expressed in oligodendrocytes of the anterior or posterior white matter tracts or neurons of the posterior horn, though we confirmed these cells express *ELAVL3*. TDP-43 pathology is not described in these cells in ALS[80]. We did not detect of *ELAVL3* CE 4a expression in oligodendrocytes of anterior horn spinal cord, although this population can have TDP-43 pathology[80]. In the motor cortex, we occasionally detected *ELAVL3* CE 4a in Betz cells. There was noticeably more expression of the CE in small neurons distributed in superficial and deep cortical layers of ALS motor cortex. Our findings match the spread of TDP-43 pathology throughout the cortical layers of ALS motor cortex[81].We observed *STMN2* CE 2a is similarly distributed in this pattern.

In spinal cord, there was a strong linkage between expression of the CEs. Although we cannot compare levels of expression between different probe channels, in all spinal cord

anterior horn motor neurons with *ELAVL3* CE 4a, we also detected *STMN2* CE 2a. We anticipated concordance of expression between the two CEs in the motor cortex; however, we observed discordance in expression was a more common pattern—small neurons often expressed either *ELAVL3* CE 4a or *STMN2* CE 2a. Our observations may be confounded by weaker detection in the secondary channel or working at the threshold of detection for the assay. That acknowledged, we believe discordance of expression is a valid finding and represents differential sensitivity to disruptions of TDP-43 within different neuronal populations of the motor cortex.

We presume that *ELAVL3* CE 4a is generated because TDP-43 is no longer available in the nucleus to occupy its binding site in intron 3, allowing for inclusion of CE 4a. It is certainly true that knockdown of TDP-43 is sufficient to generate *ELAVL3* CE 4a *in vitro.* However, there is also a binding domain for nELAVL proteins within intron 3 as well. Loss of these proteins from the nucleus may also contribute to the generation of *ELAVL3* CE 4a. In ALS motor neurons, ELAVL3 is significantly depleted from the nucleus, and ELAVL2 and ELAVL4 can show variable nuclear expression and cytoplasmic aggregation[5]. Any of these proteins could potentially play the same steric role of blocking inclusion of CE 4a.

ELAVL3 reduction, whether by the contribution of CE 4a inclusion or by other mechanisms, results in the loss of ELAVL3 RNA binding. Like TDP-43, nuclear ELAVL3 loss creates splicing changes in its targets. *AnkG* (ankyrin-3) is one example that is well-studied[60]. In the absence of Elavl3 protein, *AnkG* expresses embryonic exons that are excluded past development[60]. Subsequently, there is a dissolution of axonal polarity. Motor neurons have long axons that require intact polarity for proper cargo transport; when perturbed, there could be a breakdown of motor signaling.

ELAVL3 reduction also results in loss of mRNA 3'UTR binding. With 3'UTR binding, ELAVL3 functions to increase transcript stability (e.g. working in synergism with miR-124 to stabilize *PTBP2* in primary human neurons[82]) and forcing selection of a particular poly(A)-site (e.g. promoting the proximal poly(A) site in adherent neural cells on genes such as *Pes1* and *Gng2* to promote differentiation into GABAergic cells[63]). *TARDBP* is another target of ELAVL3 binding, with binding sites on the 3'UTR that function to stabilize and lengthen the lifespan of the transcripts[63]. Whether *TARDBP* experiences compensatory changes in expression in response to pathology is unresolved. In mice, compensatory increases have been reported in *Tardbp* heterozygous knockout mice[83], but expression of human aggregate-prone TDP-43 in mice causes reduction in endogenous TDP-43[84]. In addition to autoregulation of *TARDBP* expression, there could also be regulation from its downstream target *ELAVL3*. This regulation would be disturbed with unregulated expression of *ELAVL3* CE 4a. Further studies are required to resolve the extent of *ELAVL3* CE 4a expression in TDP43- and other proteinopathies and the functional consequences of expression.

2.4 Materials and Methods

2.4.1 Human postmortem tissue

De-identified human tissues were obtained from two sources: the UCSD ALS tissue repository that was created following HIPAA-compliant informed consent procedures approved by Institutional Review Boards (either Benaroya Research Institute, Seattle, WA IRB# 10058 or University of California San Diego, San Diego, CA IRB# 120056).

Table 2.2: List of tissues used in study including diagnostic and clinical data and experiments completed.

Case	DX	UMN vs. LMN	Site of Onset	Age	Sex	PMI	Region	Experiments
3	Control			41	F	2	SPC	CISH -ELALVL3 CE CISH -STMN3 CISH -STMN2 CE
4	Control			75	F	3.5	MC	CISH ELAVL3 CE STMN2 CE
17	SALS	U=L	Arm	55	M	3	SPC	qPCR
18	SALS	L>U	Bulbar	80	F	4	SPC, MC	qPCR
19	Control			80	F	2.5	SPC	qPCR
20	Control			38	M	6	SPC, MC	SPC: qPCR MC: CISH ELAVL3 CE & STMN2 CE
27	SALS	L>U	Bulbar	74	M	4	SPC, MC	MC: qPCR SPC: CISH -ELALVL3 CE CISH -STMN2 CISH -STMN2 CE
31	Control					3.5	SPC	qPCR
32	SALS	L>U	Respiratory	71	M	4.5	MC	qPCR
34	SALS	U>L	Bulbar	81	F	3.5	SPC, MC	SPC: qPCR MC: CISH- ELAVL3 CE
36	SALS	U>L	Leg	73	M	5	MC	qPCR
37	Control					14	SPC	CISH -ELALVL3 CE
39	Control					2	SPC	CISH -ELALVL3 CE CISH -ELALVL3
40	Control					5	SPC	qPCR CISH -ELALVL3
43	SALS	U=L	Respiratory	74	M	6	SPC, MC	SPC: qPCR MC: CISH- ELAVL3 CE
54	Control					5	SPC	qPCR
58	Control					23	SPC	qPCR
59	Control					8	SPC	qPCR
62	SALS	L>U	Arm	52	M	6	MC, SPC	qPCR
63	SALS	U=L	Arm	68	M	5	SPC	qPCR
64	SALS	U>L	Arm	47	M	6.5	SPC	qPCR
65	Control			82	M	4	MC, SPC	MC: qPCR SPC: qPCR CISH- ELAVL3 CISH -ELALVL3 CE CISH -STMN2 CISH -STMN2 CE

Table 2.2: List of tissues used in study including diagnostic and clinical data and experiments completed (continued).

Case	DX	UMN vs. LMN	Site of Onset	Age	Sex	PMI	Region	Experiments
66	SALS	L>U	Arm	46	M	7	MC, SPC	qPCR
67	Control			77	M	4	SPC	qPCR CISH -ELALVL3
69	SALS	L>U	Generalized	60	M	5	MC, SPC	qPCR
70	Control			59	F	7	MC, SPC	qPCR
73	Control			74	M	5.5	MC, SPC	SPC: CISH -ELALVL3 CISH -ELALVL3 CE MC: CISH ELAVL3 CE STMN2 CE
76	Control			68	M		SPC	CISH -ELALVL3 CE CISH -STMN2 CISH -STMN2 CE
77	Control			72	M	5	SPC	qPCR
82	SALS	U>L	Bulbar	54	M	8	MC, SPC	MC: qPCR SPC: qPCR CISH- ELAVL3
83	Control			63	F	4	SPC	qPCR
86	SALS	L>U	Arm	61	M	4.5	SPC	qPCR
87	SALS	U=L	Leg	61	F	5	SPC	qPCR
88	Control			78	F		SPC	qPCR
94	SALS	U=L	Bulbar	62	M	4	MC, SPC	MC: qPCR SPC: qPCR CISH- ELAVL3 CE CISH- STMN2 CISH- STMN2 CE
98	SALS	U=L	Bulbar	69	F	5	SPC	CISH- ELAVL3 CISH -ELALVL3 CE CISH- STMN2 CISH-STMN2 CE
99	SALS	U>L	Bulbar	70	F	4	SPC	CISH -STMN2 CISH- STMN2 CE
103	Control			92	F	10	MC, SPC	SPC: CISH-ELAVL3 CISH -ELALVL3 CE MC: CISH ELAVL3 CE STMN2 CE
109	SALS	L>U	Leg	49	M	10	SPC	qPCR
111	SALS	U=L	Leg	59	F		SPC	qPCR
112	SALS	L>U	Leg	54	F	8	SPC	qPCR

Table 2.2: List of tissues used in study including diagnostic and clinical data and experiments completed (continued).

Case	DX	UMN vs. LMN	Site of Onset	Age	Sex	PMI	Region	Experiments
113	SALS	U=L	Leg	66	M		MC, SPC	MC: CISH ELAVL3 CE STMN2 CE SPC: qPCR CISH -ELALVL3 CE CISH -ELALVL3 CISH- STMN2 CE
116	SALS	L>U	Leg	72	M	4.5	SPC	qPCR
117	FALS C9	U>L	Bulbar	66	F	12	MC	MC: CISH ELAVL3 CE & STMN2 CE
118	SALS	U>L	Bulbar	56	F	4	MC	MC: qPCR CISH ELAVL3 CE STMN2 CE SPC: qPCR
120	FALS C9/FTLD	U>L	Bulbar	64	M	9	MC	CISH ELAVL3 CE STMN2 CE
121	SALS	U=L	Arm	67	M	3	SPC	qPCR CISH -ELALVL3 CISH -ELALVL3 CE CISH -STMN2 CISH -STMN2 CE
123	SALS	L>U	Trunk	57	M	9	SPC	CISH -ELALVL3 CISH -ELALVL3 CE
125	SALS	L>U	Arm	67	M	3	MC, SPC	MC: qPCR SPC: qPCR CISH -ELALVL3 CISH -ELALVL3 CE CISH -STMN2 CE
126	SALS	U>L	Arm	70	M	6	MC, SPC	qPCR
127	SALS	L>U	Arm/Resp	67	M	6	SPC	qPCR CISH -ELALVL3 CISH -ELALVL3 CE
128	SALS	L>U	Foot	69	F	5.5	SPC	qPCR CISH -ELALVL3 CISH -ELALVL3 CE
130	SALS	L>U	Leg	63	M	6.5	MC, SPC	qPCR
131	Control			56	M	2.5	MC, SPC	MC: qPCR SPC: qPCR CISH -ELALVL3 CISH -ELALVL3 CE CISH -STMN2 CISH -STMN2 CE
132	SALS	U=L	Arm	64	F	6.5	MC, SPC	qPCR CISH -ELALVL3 CE CISH -STMN2

Table 2.2: List of tissues used in study including diagnostic and clinical data and experiments completed (continued).

Case	DX	UMN vs. LMN	Site of Onset	Age	Sex	PMI	Region	Experiments
133	Control			76	M	7.5	SPC	qPCR CISH -ELALVL3 CE CISH -ELALVL3 CISH -STMN2 CISH- STMN2 CE
134	SALS/FTD	U>L	Bulbar/Leg	78	F	6.5	SPC	qPCR
135	SALS	L>U	Respiratory	77	M	9	MC, SPC	qPCR
142	SALS	U>L	Leg	79	M	18.5	MC, SPC	qPCR
146	Control			53	F	18.5	SPC	CISH -ELALVL3 CE

Table 2.3: Table of sample sizes for quantitative experiments

qPCR			
Probe	**Diagnosis**	**Spinal Cord**	**Motor Cortex**
ELAVL3	Control	15	4
ELAVL3	ALS	29	15
ELAVL3 CE	Control	15	4
ELAVL3 CE	ALS	30	15
STMN2	Control	15	4
STMN2	ALS	30	15
STMN2 CE	Control	15	4
STMN2 CE	ALS	30	15
ISH: Spinal Cord			
Probe	**Diagnosis**	**Cases**	**Cells**
ELAVL3	Control	6	156
ELAVL3	ALS	8	326
ELAVL3 CE	Control	13	276
ELAVL3 CE	ALS	12	344
STMN2	Control	5	156
STMN2	ALS	8	267
STMN2 CE	Control	5	169
STMN2 CE	ALS	9	248

2.4.2 RNA extraction, reverse transcription polymerase chain reaction, quantitative PCR, and Sanger sequencing

For RNA extraction, frozen nervous tissue was homogenized in TRIzol reagent (Invitrogen), chloroform used for phase separation, and RNA in the aqueous phase cleaned and concentrated with the RNeasy Mini Kit (Qiagen). For all experiments, 50 ng RNA was used as quantified by a NanoDrop Microvolume Spectrophotometer. For splice analysis using RT-PCR, amplicons were generated using the SuperScript IV One-Step RT-PCR System and visualized on a 2% polyacrylamide gel using gel electrophoresis GelGreen Nucleic Acid Stain (Biotium). Gels were imaged using a ChemiDoc XRS+ (Bio-Rad). Bands of interest were extracted using Zymoclean Gel DNA Recovery Kits (Zymo) and cloned using the pGEM®-T Easy Vector System (Promega). RT-qPCR was carried out in duplicates using iTaq Universal SYBR Green One-Step Kit (Bio-Rad) in a in a CFX384 real-time PCR machine. Expression of glyceraldehyde-3-phosphate dehydrogenase (*GAPDH*) was used as an internal control gene. All primers used are listed belwo (Table 2.4).

Table 2.4: Primers used in studies.

Primer Identity	Sequence 5' to 3'	Assay
ELAVL3 Exon 3 Forward	ACAAAGCCATCAACACCCTCA	RT-PCR
ELAVL3 Exon 5 Reverse	GAATCCCACACCCCGAGAGA	RT-PCR
ELAVL3 Exon 4a Forward	GGATGTTTGTGTGTCACCGC	qPCR
ELAVL3 Exon 4 Reverse	GAACTGGGTCTGGCATAGGA	qPCR
ELAVL3 3'UTR Forward	CACGCAGACAGTCACACCA	qPCR
ELAVL3 3'UTR Reverse	CCTGTCCACGTGTCTGAGTTT	qPCR
STMN2 Forward	AGCTGTCCATGCTGTCACTG	qPCR
STMN2 Reverse	GGTGGCTTCAAGATCAGCTC	qPCR
STMN2 Truncated Forward	GGACTCGGCAGAAGACCTTC	qPCR
STMN2 Truncated Reverse	GCAGGCTGTCTGTCTCTCTC	qPCR

2.4.3 Chromogenic *in situ* hybridization, imaging, and semi-quantitative analysis

To detect signal RNA molecules, chromogenic *in situ* hybridization was performed on 6 μm FFPE sections using BaseScope™ Red Assay kit v2 or Duplex Assay (ACDBio) and the target probes (Table 2.5) to manufactures' guidelines including an extended target retrieval (30 minutes) and Protease IV treatment (45 minutes). Sections were counterstained in hematoxylin and visualized using the Olympus VS200 Slide Scanner at 20X magnification (UCSD Microscopy Core NINDS P30NS047101). The threshold for background staining was 1 locus for every 20 counted cells.

Table 2.5. ACDBio *in situ* hybridization probes used in studies.

Target	Probe	Catalog No.	Targeting Information
Full-length *STMN2*	BA-Hs-STMN2-3zz-st	869311	3 ZZ probe pairs targeting base pairs 958-1111 of transcript NM_001199214.2
STMN2 CE 2a	BA-Hs_STMN2-E1cryptic-Junc	851401	1 ZZ probe pair targeting the junction of exon 1 and exon 2a in *Stmn2*
Spliced *ELAVL3*	BA-Hs-ELAVL3-cust-3zz-st	1072241	3 ZZ probe pairs targeting base pairs 431-758 of transcript NM_001420.4
ELAVL3 CE 4a	Ba-Hs-ELAVL3-CE3E4	1263651	1 ZZ probe pair targeting the junction of exon 4a and exon 4 in *ELAVL3*
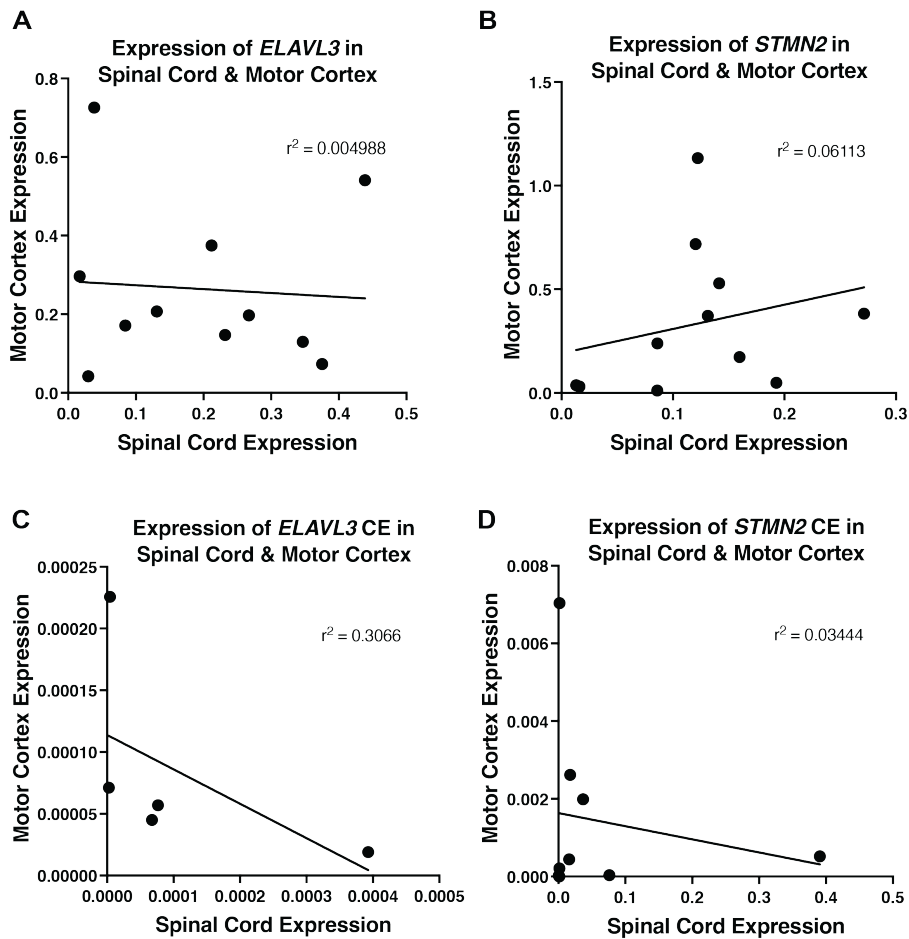
Supplemental Figure 2.1. Comparison of expression of ELAVL3 and STMN2 genes and their cryptic exons in spinal cord and motor cortex. (**A-D**) Plots comparing qPCR expression of (**A**) ELAVL3, (**B**) STMN2, (**C**) ELAVL3 CE 4a, and (**D**) STMN2 CE 2a in spinal cord and motor cortex. There was a poor correlation between the two regions for all genes.

2.5 Acknowledgements

CHAPTER 3: ELAVL3 NUCLEAR MISLOCALIZATION IN CORTICAL ALS & FTLD PROTEINOPATHIES

3.1 Background

ALS and FTLD exist on a spectrum of related clinical syndromes, autosomal dominant genetic lesions, and neuropathologic hallmarks (Figure 1.1). Considering neuropathology as the dividing schema, almost all sporadic ALS cases are characterized by misfunction of the RNA binding protein (RBP) TDP-43 connected to neuropathologic findings of nuclear TDP-43 loss and/or hyperphosphorylated TDP-43 aggregates in the cytoplasm[2,3]. Roughly half of patients with FTLD share this finding (FTLD-TDP43), with the other half marked by the presence of hyperphosphorylated tau aggregates (FTLD-Tau). Differentiating underlying molecular pathology (TDP-43 vs. tau) predominantly occurs after death during postmortem neuropathologic examination[26]. The clinical presentations of these diseases can be identical or can even phenocopy the amnestic syndrome associated most with Alzheimer's disease[48].

In ALS and FTLD-TDP43, the morphologic appearance (Figure 3.1) and distribution of pTDP-43 aggregates can vary widely between cases. A harmonized classification system for FTLD-TDP43 histologic subtypes was proposed in 2017 based on the presence/absence of pTDP43-associated dystrophic neurites and neuronal/glial inclusions within neocortex (Table 1.1)[45]. While some subtypes are more commonly associated with particular FTD clinical syndromes or genetic lesions (Figure 1.1), there is no indication of significant differences in disease duration, age of death, or age of onset between histologic groups[45]. Using the FTLD-TDP43 classification system as a reference point, a 2023 study divided pTDP43 pathology in the ALS motor cortex into three subtypes: Type E has predominantly

granulofilamentous neuronal inclusions and grains spread throughout the cortical layers; Type B has predominantly round neuronal cytoplasmic inclusions and some dystrophic neurites spread throughout the cortical layers; Type SC has scarce pTDP-43[81]. This study did not factor in upper motor neuron symptoms (spasticity, hyperreflexia, increased tone) versus lower motor neuron symptoms (flaccidity, hyporeflexia, muscle atrophy), but it did consider cognitive assessment data. Again, the histologic subtype was not related to disease duration, age of death, or age of onset.
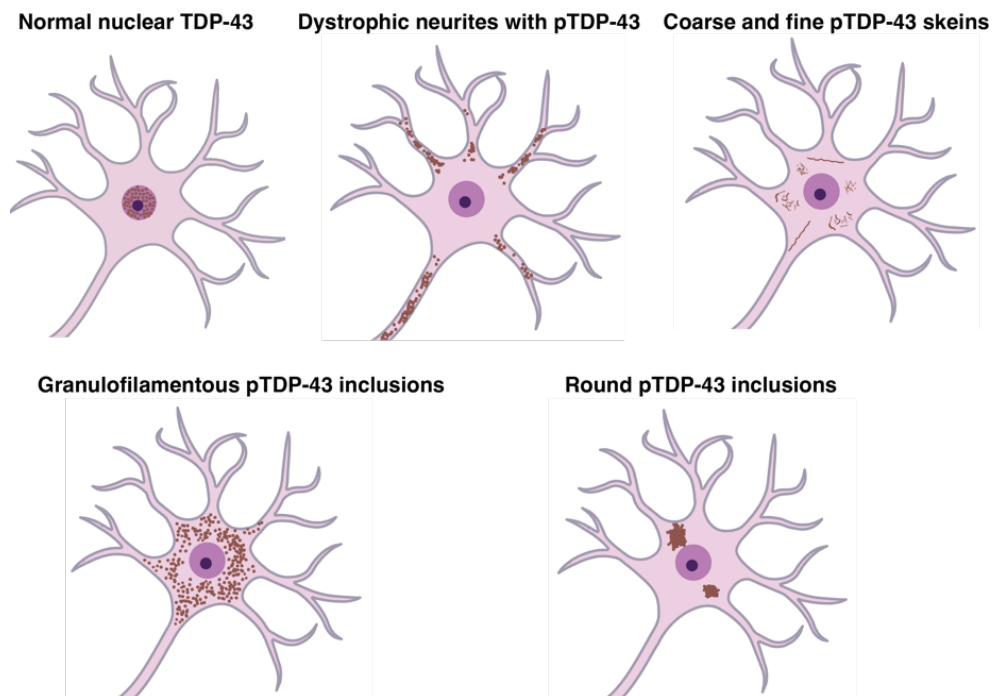
Figure 3.1*. **Schematic of key TDP-43 pathologic findings in ALS/FTLD neurons. Top left**: normal distribution of TDP-43 (brown) in the nucleus (purple, nucleolus- dark purple) of neurons. **Top middle**: swollen, bulbous neuronal processes filled with pTDP-43 that can be short or long. **Top right**: loose tangles/coils of pTDP-43 in the soma that can appear very fine or thick and coarse. **Bottom left**: pTDP-43 aggregates in the soma and proximal processes with a dot-like or fibrous appearance. **Bottom right**: pTDP-43 inclusions that appear dense and rounded within the cell's soma.

ALS and FTLD-TDP43 share genetic mutations that underlie TDP-43 misbehavior[2]. The most common genetic cause of ALS and FTD is a hexanucleotide repeat expansion in a non-coding region of the *C9ORF72* gene. The gene locus is transcribed bidirectionally, creating RNA foci observed in human tissues, which may function to pathologically sequester RBPs. The translated dipeptide repeat proteins are detected in human tissue as ubiquinated inclusions, but importantly, these inclusions do not include TDP-43[85–87]. The exact mechanisms of toxicity and the relationship to TDP-43 aggregation remains under investigation[88]. Less commonly, mutations in *TARDBP,* which encodes TDP-43, drive pathology. The majority of mutation sites lie within the C-terminal region, which is intrinsically disordered and aggregation-prone[89].

FTLD-Tau is defined by the presence of hyperphosphorylated tau aggregates, most often intracellular, in the neocortex and subcortical regions[36]. The biochemical composition and anatomical distribution of phosphorylated Tau (pTau) aggregates can be used to subclassify FTLD-Tau into pathologic subtypes (Table 1.2). One part of the dividing schema is the number of microtubule-binding domains within tau protein isoforms, which is driven by alternative splicing of exon 10 within *MAPT* mRNA transcripts[1]. In normal brain and AD, there is an equal proportion of tau with three microtubule-binding domains (3R tau) and tau with four microtubule-binding domains (4R tau). In contrast, the tau aggregates in Pick's disease contain primarily 3R tau; tau aggregates in corticobasal degeneration (CBD) and progressive supranuclear palsy (PSP) primarily contain 4R tau. Mutations in *MAPT* highlight the pathomechanism of tau dysfunction in disease—decreased affinity of tau for axonal microtubules when it is hyperphosphorylated and increased affinity toward self-aggregation[1].

There are a number of unifying features of FTLD-TDP43 and FTLD-Tau, in addition to overlap in clinical presentation. First, both are characterized by disturbances in RBPs. In response to TDP-43 or tau-associated cellular stress, nuclear RBPs such as TIA1 and HNRNPA0 exit the nucleus and localize to (and are perhaps trapped within) stress granules[4,65]. Second, there is evidence that biochemical strains of either TDP-43 or tau underlie seeding and spreading behavior and, ultimately, clinical manifestation of disease[90,91] Third, both the *TARDBP* and *MAPT* transcripts have binding sites for nELAVL proteins[92]. On the *TARDBP* transcript, there are ten binding sites on the 3' UTR. On the *MAPT* mRNA transcript, there are four intronic binding sites within exons 1 and 2 and six 3'UTR binding sites.

Previous work in the Ravits lab examined TDP-43 pathology in ALS spinal cord in in relation to the RBP ELAVL3, which is downregulated at the transcript level in anterior horn motor neurons in ALS[5]. Using immunofluorescence, less than one-half of the observed ALS motor neurons demonstrated nuclear loss of TDP-43 in contrast to over two-thirds of neurons which lacked nuclear ELAVL3. Granulofilamentous ELAVL3 cytoplasmic aggregates were detected, but these were less common in frequency than nuclear depletion. For both TDP-43 and ELAVL3, cytoplasmic inclusions only appear in the context of nuclear depletion. No other ELAVL family members demonstrated consistent ALS-related pathology but did show rare filamentous and granular inclusions.

Three observations demonstrated that ELAVL3 misbehavior be independent of TDP-43 disruption: (1) the observation of motor neurons with normal, nuclear TDP-43 but nuclear depletion of ELAVL3, (2) displacement of ELAVL3 from the nucleus in patient samples with SOD-1-mediated ALS where there is no TDP-43 pathology, and (3)

application of stress on neuroblastoma cells causes loss of nuclear ELAVL3 earlier than loss of TDP-43[5]. Given this, we hypothesize that ELAVL3 misbehavior may be a unifying feature of FTLD pathologies.

In this chapter, we expand our previous neuropathologic observations of ELAVL3 reduction and subcellular mislocalization in ALS spinal cord into ALS motor cortex, FTLD-TDP43 frontal cortex, and FTLD-Tau frontal cortex using immunofluorescent microscopy. We first describe efforts to validate the most specific and sensitive anti-ELAVL3 for our studies. We next describe patterns of ELAVL3 staining in adult human cortex and either pTDP-43 or pTau histologic pathology in disease groups. Finally, we demonstrate cortical ELAVL3 pathology is a unifying feature of cortical ALS, FTLD-TDP43, and FTLD-Tau.

3.2 Results

3.2.1 Quality control of ELAVL3-targeting primary antibodies

Because our study relied on antibody detection of ELAVL3, we tested the specificity and sensitivity of commercially available and custom-designed monoclonal and polyclonal anti-ELAVL3 antibodies. There is a high degree of homology among ELAVL family members, particularly within highly conserved RNA binding domains (Figure 1.2). Given our concern for cross-detection of nELAVL family proteins, we tested antibody detection of recombinant ELAVL2, ELAVL3, and ELAVL4 proteins (Figure 3.2). Tested antibodies were designed to detect a range of ELAVL3 peptides including short sequences at the N-terminus, segments within the first RNA binding domain, segments containing the hinge domain, and full-length protein (Figure 3.2A). The majority of commercially available anti-ELAVL3 antibodies detected recombinant ELAVL2 and/or ELAVL4 proteins, sometimes

with higher sensitivity than detection of ELAVL3. We selected a rabbit polyclonal antibody targeting the N-terminus (amino acids 19-36) for further evaluation (Proteintech 55047-1-AP) because it had the best specificity profile (Figure 3.2B). Although this antibody provided the best binding specificity to recombinant ELAVL3, we did occasionally detect faint binding to ELAVL4 recombinant protein in blots.

To evaluate antibody specificity in a biologic *ELAVL3* knock-out system, we developed CRISPR/Cas9-derived lines of *ELAVL3* knock-out Kelly neuroblastoma cells (Synthego, Redwood City, CA). We used these lines and corresponding un-edited Kelly cell *ELAVL3* wild-type control to measure antibody detection of ELAVL3 and nELAVL family members in a human neural cell model. Our selected antibody successfully detected ELAVL3 in *ELAVL3*^{+/+} wild-type cells (Figure 3.3A) and did not detect family member ELAVL4. Abcam ab184267 (rabbit monoclonal), designed to detect ELAVL3 and ELAVL4, also captured loss of ELAVL3 in Kelly *ELAVL3*^{-/-} cells (Figure 3.3B). Using Proteintech 55047-1-AP, the threshold of detection for recombinant ELAVL3 by Western blot was roughly 3 ng (Figure 3.3C). Because the antibody binds the N-terminus, we hypothesized it could be capable of capturing expression of truncated ELAVL3 protein isoforms if expressed above the sensitivity threshold (0.01% of total protein lysate). Previous aliquots of this antibody were utilized for our earlier study[5] but at a lower concentration (150 ug/uL versus 600 ug/uL) and with inconsistent Western blotting results between lots.

We confirmed our new concentrated antibody lots recapitulated our previously published observation of ELAVL3 nuclear mislocalization in roughly 50% of anterior horn spinal cord motor neurons (Figure 3.4A-B)[5]. However, we did not detect a significant population of neurons with nuclear TDP-43 and cytoplasmic ELAVL3 expression, compared

to nearly 25% in the previous study. Instead, we detected roughly that number of neurons

with cytoplasmic TDP-43 and nuclear ELAVL3. In these neurons, ELAVL3 is not enriched

in the nucleus, but rather has uniform staining between the nucleus and cytoplasm that may

have been captured by a more sensitive antibody lot (Figure 3.4C-E').

Figure 3.2. Specificity of antibodies targeting ELAVL3. (**A**) Schematic of ELAVL3 antibodies trialed and the region of ELAVL3 they are designed to target. RNA binding domains are highlighted in orange. Target amino acid sequences indicated in blue. (**B-J**) Western immunoblots loaded with 0.225 ng/lane recombinant protein of neural ELAVL family members (ELAVL2, ELAVL3, and ELAVL4). The most specific antibody was Proteintech 55047-AP, a rabbit polyclonal antibody targeting the N-terminus of ELAVL3 (**B**).
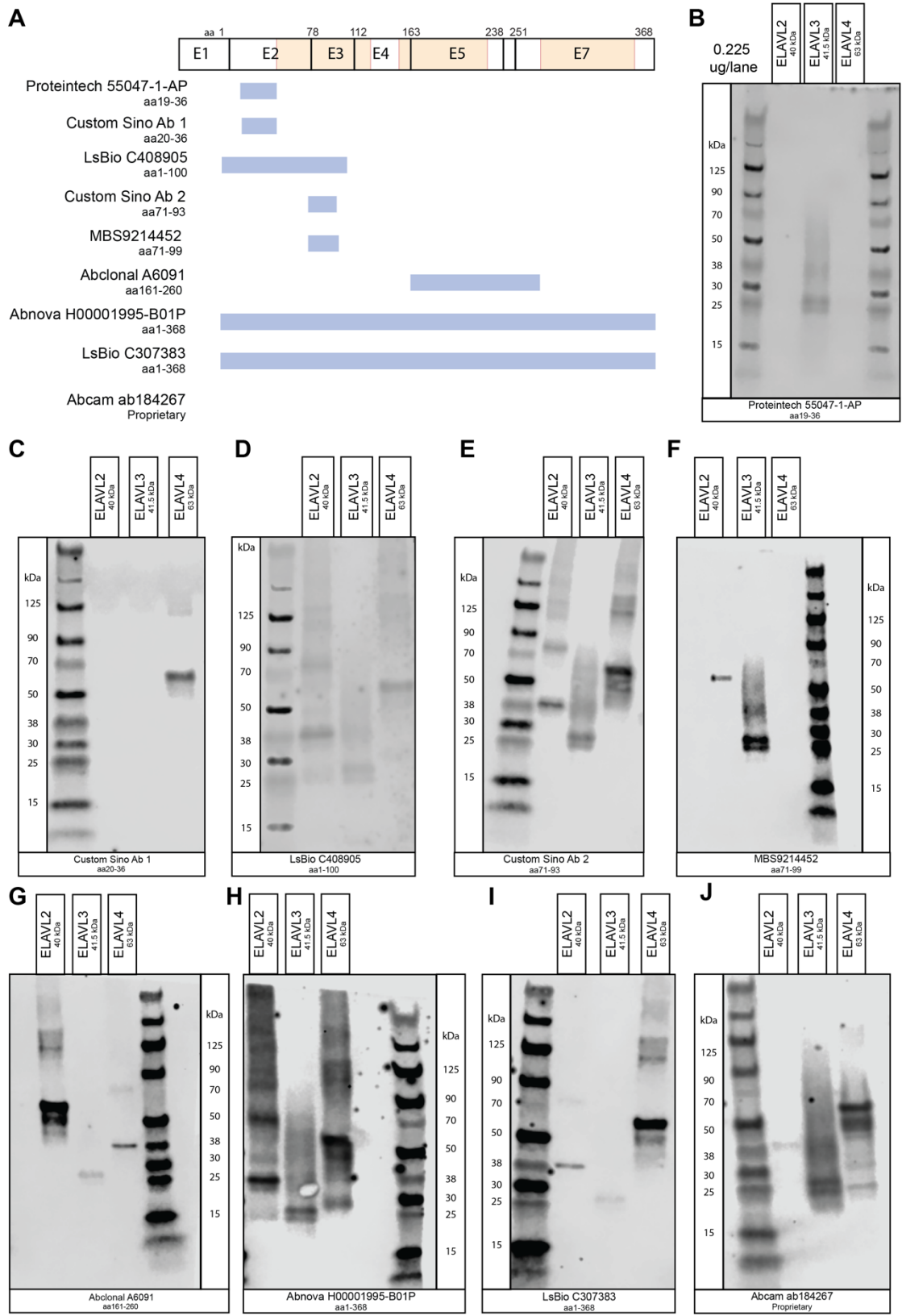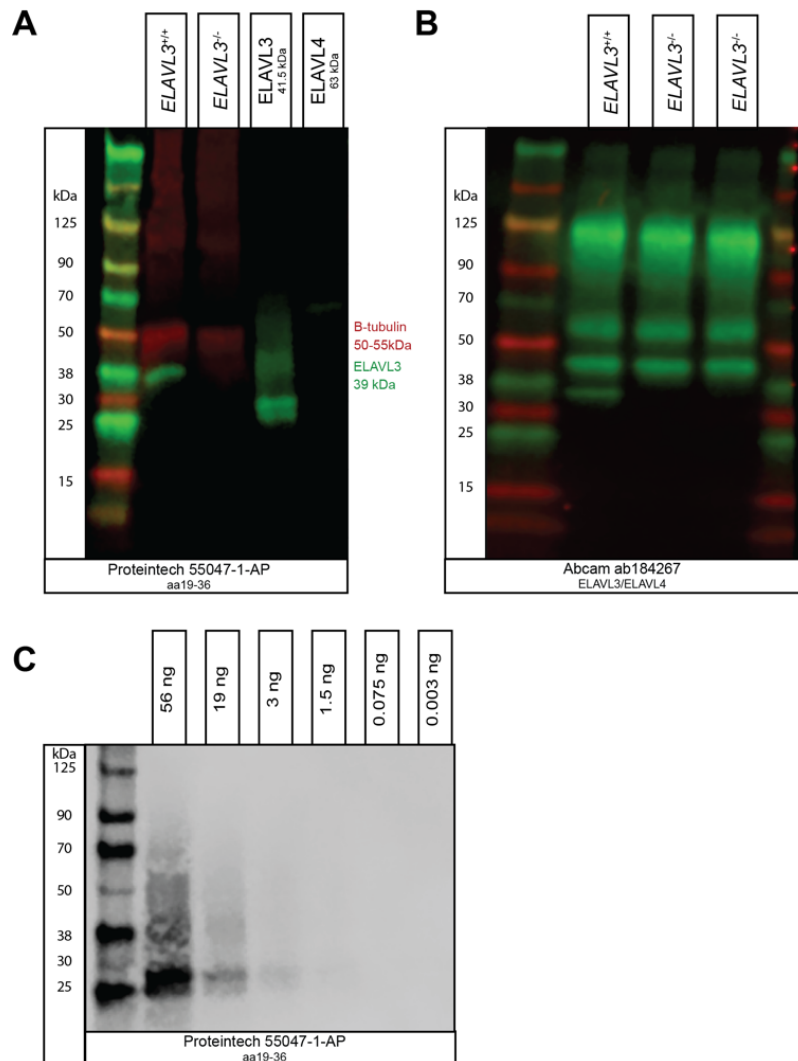
Figure 3.3. Sensitivity and specificity of select antibodies in detecting ELAVL3 in knock-out neuroblastoma cells. (**A**) The most specific anti-ELAVL3 antibody was Proteintech 55047-AP, a rabbit polyclonal antibody targeting the N-terminus of ELAVL3, which does not detect any nELAVL-family members in *ELAVL3* knockout cells. (**B**) Abcam ab154267 antibody is designed to detect ELAVL3 and ELAVL4 and can detect both proteins in neuroblastoma cells. (**C**) Threshold of detection for Proteintech 55047-AP using a dilution series of recombinant ELAVL3.
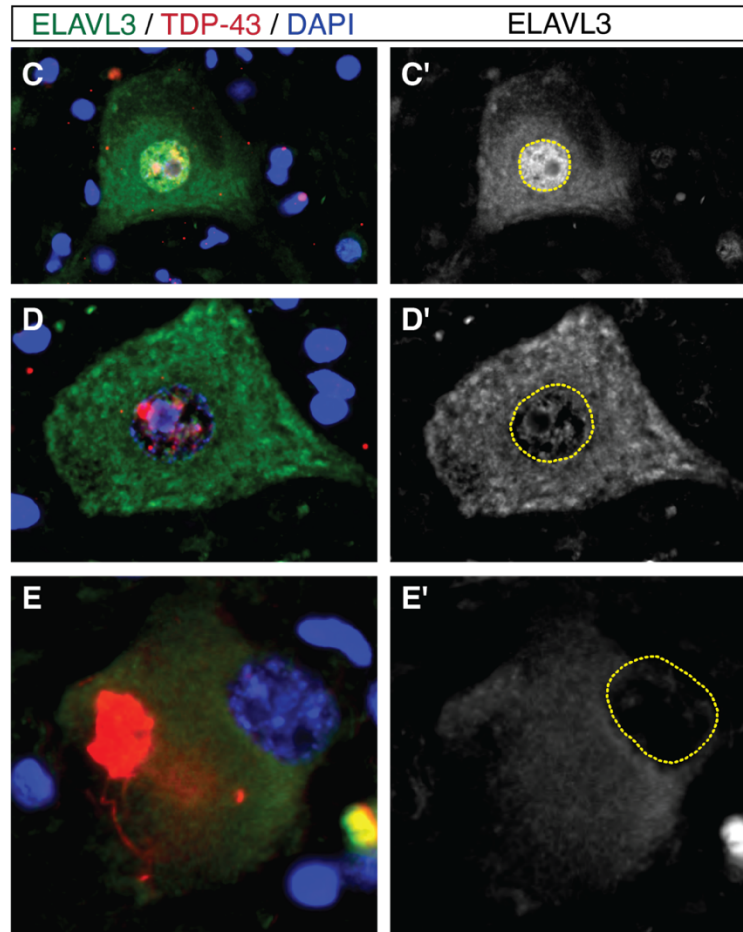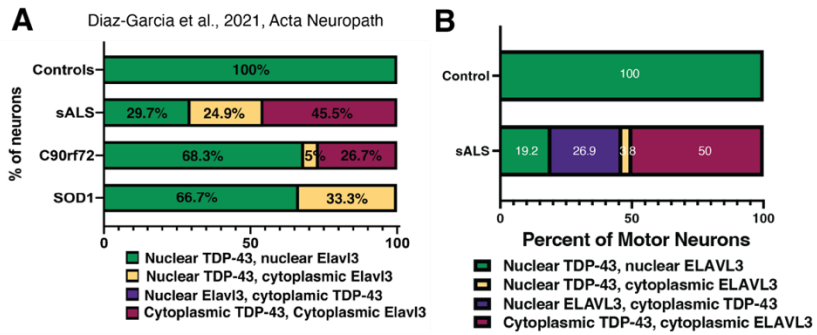
Figure 3.4. ELAVL3 and TDP-43 nuclear and cytoplasmic expression in anterior horn spinal cord motor neurons. (**A**) Figure panel from Diaz-Garcia et al., 2021, Acta Neuropath. Sporadic ALS (sALS) spinal cord showed roughly 50% of motor neurons with both ELAVL3 and TDP-43 nuclear mislocalization using Proteintech 55047-1-AP at 150 ug/uL. No control neurons showed ELAVL3 mislocalization. (**B**) Pilot cohort to test new lots of Proteintech 55047-1-AP at 600 ug/uL antibody demonstrated roughly 50% of neurons with both ELAVL3 and TDP-43 nuclear mislocalization. No control neurons showed nuclear mislocalization. (**C-E'**) Representative images of (**C-C'**) nuclear TDP-43 and enriched nuclear ELAVL3 staining, (**D-D'**) nuclear TDP-43 and uniform nuclear and cytoplasmic ELAVL3 staining, and (**E-E'**) absent TDP-43 nuclear staining and cytoplasmic aggregation and absent ELAVL3 nuclear staining. Nuclei are highlighted with a dotted yellow line.

3.2.2 ELAVL3 protein expression in adult human frontal and motor cortices

In adult human cortex, *ELAVL3* mRNA is highly expressed in most neuron and glia subpopulations (Figure 3.5A-B)[93,94]. The exceptions include microglia, astrocytes, and oligodendrocyte precursor cells (OPCs). In order to validate these findings at a protein level, we utilized immunofluorescent detection of ELAVL3 in formalin-fixed, paraffin embedded (FFPE) frontal and motor cortex tissue sections. For all ELAVL3 protein studies in FFPE, we utilized Proteintech 55047-AP rabbit polyclonal anti-ELAVL3 antibody.

We confirmed ELAVL3 is highly expressed in neurons throughout the cortical layers and enriched in the nucleus relative to the cytoplasm (Figure 3.6A-E). It is also highly expressed in the nuclei of oligodendrocytes of the gray and white matter. Like spinal cord motor neurons, Betz cells of motor cortex layer 5 had expression of ELAVL3 in both the nuclear and cytoplasmic compartments, with enrichment in the former compared to the latter. As predicted from mRNA data, expression of ELAVL3 is higher in neurons of cortical layers 2/3 relative to deeper layers 5/6. ELAVL4 is the nELAVL family member expressed the highest in excitatory neurons of cortical layers L4-L6, as predicted from mouse protein expression[7,95].

As anticipated from single-cell sequencing data, we did not detect expression of ELAVL3 in astrocytes co-labeled with glial fibrillary acidic protein (GFAP) (Figure 3.6F). Oligodendrocyte precurosor cells (identified by higher OLIG2 staining relative to oligodendrocytes[93,94]) also showed little ELAVL3 staining (Figure 3.6G). These findings are in contrast to TDP-43, which is expressed in the nuclues of both astrocytes and oligodendrocyte precursor cells.
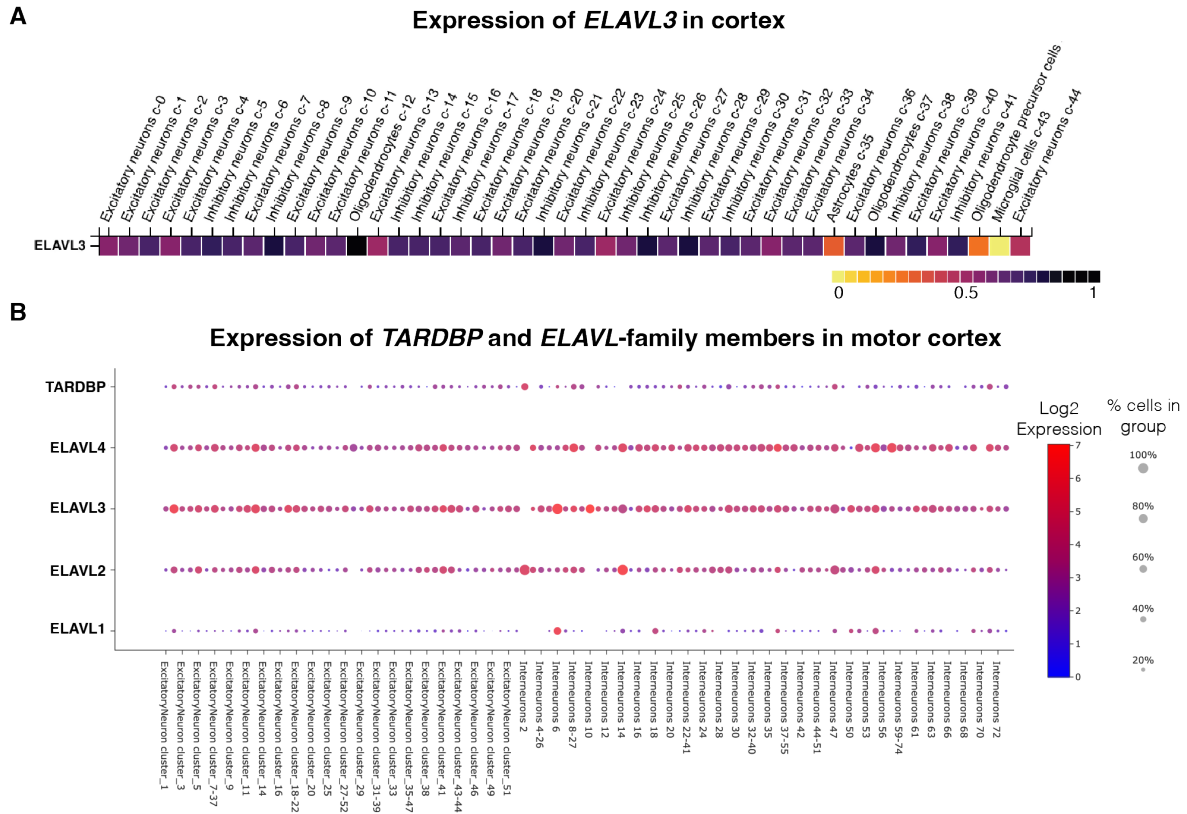
Figure 3.5. *ELAVL3* mRNA expression in neural subclusters. (**A**) Heatmap of *ELAVL3* expression in cell subclusters of human cortex. Heatmap values are normalized to the highest expression value (black) with low or no measured expression in yellow. Figure adapted from www.proteinatlas.org (**B**) Dot plot showing relative expression of *TARDBP*, *ELAVL3*, and other *ELAVL*-family members in cell subclusters of human motor cortex. Figure generated using Neuroscience Multi-Omic Analytics (NeMO).
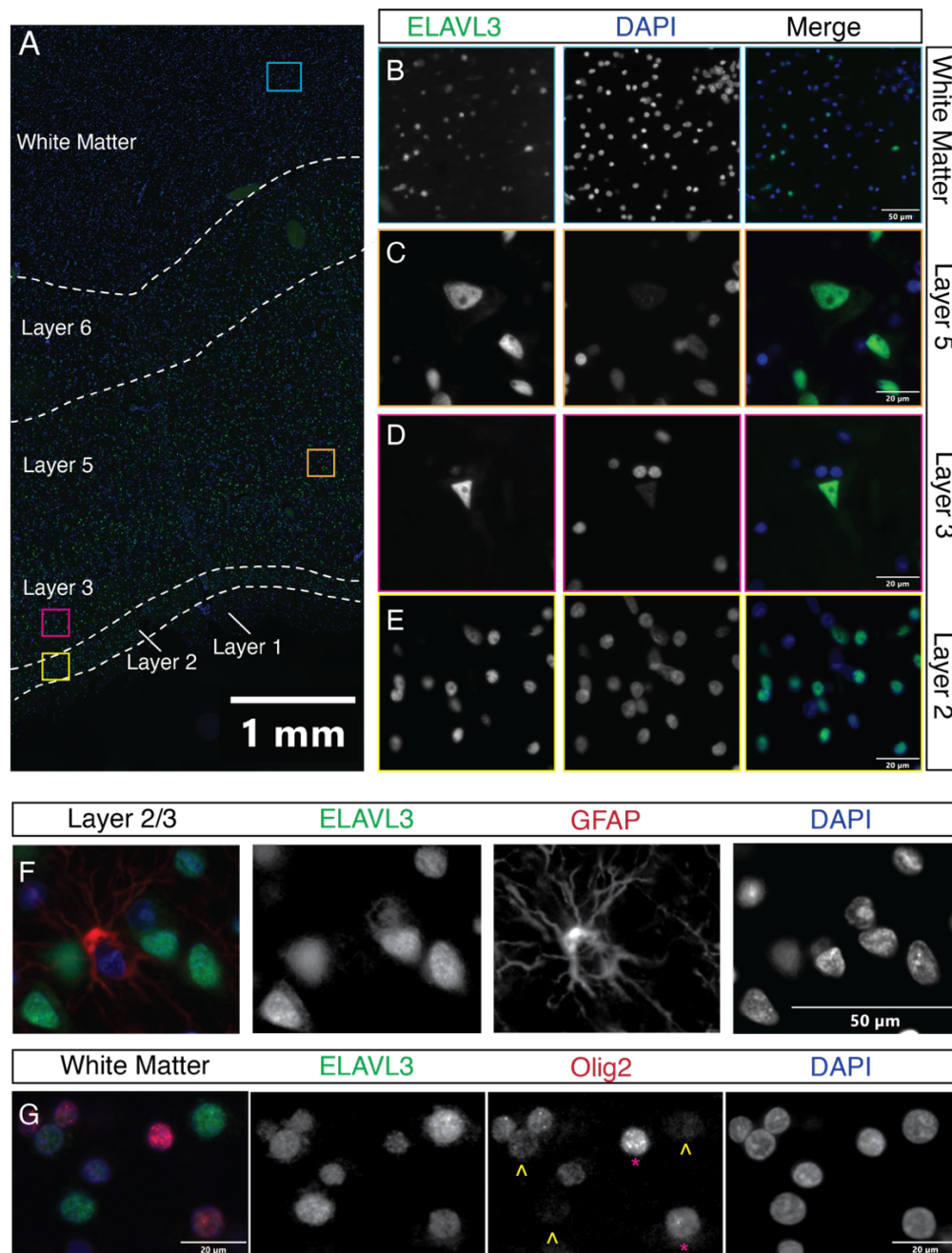
Figure 3.6. ELAVL3 is expressed in neurons and oligodendrocytes of all cortical layers, but not in astrocytes or oligodendrocyte precursor cells. (**A-E**) Representative images of expression of ELAVL3 in control motor cortex by cortical layer. ELAVL3 is enriched in the nucleus. (**F**) EELAVL3 is not expressed in astrocytes, which express GFAP in its processes. (**G**) ELAVL3 is expressed highly in oligodendrocytes, which express OLIG2 at low levels (yellow carrots), and is expressed lower in oligodendrocyte precursor cells, which express OLIG2 at higher levels (magenta asterisks).

3.2.3 Descriptions of motor cortex pTDP-43 pathology and pathologic subtype in ALS

For this study, FFPE sections of motor cortex from controls (n=5) and ALS (n=16) motor cortex were utilized (Table 3.6 for demographic data). The majority of ALS cases selected for this study had clinical features of UMN disease (i.e., spasticity, hyperreflexia, clonus). We hypothesized that UMN clinical findings would be a predictor of moderate or severe pTDP-43 burden within the motor cortex. To characterize pTDP-43 pathology, we used a mouse monoclonal antibody directed towards the phosphorylated 409/410 epitope. We described the key pTDP-43 pathology in the gray and white matter of motor cortex (Table 3.1). We observed frequent neuronal and glial inclusions, most often dense and round or small and granular. We also observed cases with small grains distributed throughout the gray matter. Less frequently, we observed short and long dystrophic neurites and skeins. In contrast to spinal cord, where surviving motor neurons frequently showed TDP-43 pathology (Figure 3.7A-B), precentral gyrus layer 5 motor neurons (Betz cells) rarely showed pTDP-43 aggregates or loss of TDP-43 from the nucleus (Figure 3.7C-E).

We subcategorized our ALS cohort into pathologic types B, E, and SC using the criteria described in a 2023 neuropathologic study categorizing motor cortex pTDP-43 in 61 ALS cases that excluded ALS-FTLD diagnoses and did not report upper or lower motor neuron clinical findings[81]. Types B and E are named after their pathologic equivalents in FTLD-TDP43 (Table 1.1), while type SC is novel to ALS motor cortex. Within our cohort of 16 ALS motor cortices, we found three-quarters of cases (9/12) with UMN clinical findings also had moderate or severe pTDP-43 aggregates driving a classification of Type B or Type E (Table 3.2). Both ALS patients with an unknown clinical phenotype were Type SC.

Table 3.1. Description of clinical phenotype and phosphorylated TDP-43 pathology in ALS motor cortices used in study.

Case	Clinical Phenotype	pTDP-43 pathology	Subtype
96	SALS/FTLD U>L, Bulbar	Sparse round inclusions in deep cortical layers and white matter	Type SC
104	SALS/FTLD	Sparse round inclusions in motor cortex and white matter	Type SC
34	SALS U>L, Bulbar	Moderate cortical granulofilamentous and round inclusions, occasional dystrophic neurites, sparse inclusions in white matter	Type B
99	SALS U>L, Bulbar	Moderate granulofilamentous inclusion in cortex, occasional dystrophic neurites, sparse white matter inclusions	Type B
118	SALS U>L, Bulbar	Severe granulofilamentous and round inclusions in gray matter and white matter	Type B
119	SALS U>L, Arm	Severe granulofilamentous inclusions, skeins and grains in gray matter, mild inclusions in white matter	Type E
48	SALS U=L, Bulbar	Sparse cortical round inclusions	Type SC
122	SALS U=L, Bulbar	Moderate granulofilamentous inclusions, occasional dystrophic neurites, skeins, and grains in gray and white matter	Type E
121	SALS U=L, Arm	Moderate/severe round inclusions in deep layers of gray matter, mild inclusions in white matter	Type B
132	SALS U=L, Arm	Severe round neuronal and glial inclusions spread throughout the cortical layers, occasional dystrophic neurites, mild white matter pathology	Type B
128	SALS L>U, Foot	Severe cortical and mild white matter pathology, common granulofilamentous inclusions and cortical grains; occasional dystrophic neurites	Type E
127	SALS L>U, Arm/Resp	Sparse round inclusions in white matter and motor cortex	Type SC
110	SALS	Sparse round inclusions in white matter and motor cortex	Type SC
120	FALS/FTLD C9 U>L Bulbar	Sparse round inclusions in white matter and motor cortex	Type SC
117	FALS C9 U>L, Bulbar	Severe granulofilamentous inclusions and grains, occasional dystrophic neurites and skeins, mild inclusions in white matter	Type E
98	FALS C9 U=L, Bulbar	Moderate cortical granulofilamentous and round inclusions, dystrophic neurites, and coarse skeins, sparse inclusions in white matter	Type B

Table 3.2. ALS motor cortex clinical and pathological correlates in ALS motor cortex.

Clinical Phenotype	Pathologic Subtype			
	Type B	Type E	Type SC	Total
UMN	6 (50% of UMN)	3 (25%)	3 (25%)	12 (100%)
LMN	0 (0% of LMN)	1 (50%)	1 (50%)	2 (100%)
?	0	0	2 (100%)	2 (100%)
Total	6	4	6	16

3.2.4 Nuclear mislocalization and downregulation of ELAVL3 in ALS motor cortex

In the spinal cord, we previously observed displacement of nuclear ELAVL3 in lower motor neurons with and without TDP-43 pathology[5]. We asked whether motor cortex upper motor neurons (Betz cells) experience the same patterns of ELAVL3 nuclear displacement in ALS. Using immunofluorescence, we did not observe Betz cells with ELAVL3 nuclear clearing in our ALS cohort (Figure 3.7C-E'''). Because we did not observe total nuclear ELAVL3 loss, we measured sublte changes in ELAVL3 nuclear fluorescent intensity in Betz cells (see 3.4.6 for quantification methods). We validated our analytical approach using ALS and control spinal cord motor neurons (Figure 3.7F). We re-capitulated key findings of reduced nuclear expression of both TDP-43 ($P<0.001$) and ELAVL3 ($P<0.001$) in ALS spinal cord motor neurons compard to control.

Using the same approach to analyze ELAVL3 nuclear expression in motor cortex Betz cells, we found a strong trend toward ELAVL3 downregulation in ALS cells compared to controls ($P=0.1114$) (Figure 3.7G). We may not have sufficient power capture significant downregulation. Alternatively, Betz cells are resilient to pathologic changes in ALS. We also did not detect a significant difference in TDP-43 nuclear staining in ALS Betz neurons relative to controls ($P=0.4526$). Again, we have low power to detect differences, but our analysis fits our observations of no TDP-43 nuclear clearance or cytoplasmic pTDP-43

aggregates. ELAVL4 is the family member expressed the highest in large projection neurons of cortical layer 5[60]. However, we also did not find differences in expression of ELAVL4 in ALS Betz cells relative to controls (data not shown).

In cells with TDP-43 pathology, marked by either loss of nuclear TDP-43 or presence of pTDP-43 aggregates, ELAVL3 showed variable patterns of expression (Figure 3.8A-E'''). Most often, ELAVL3 remained enriched in the nucleus relative to the cytoplasm. Occasionally, we observed notable ELAVL3 depletion. Measured nuclear fluorescent intensity of ELAVL3 was significantly lower in cells containing pTDP-43 aggregates compared to those without (P=0.0228) (Figure 3.8F). ELAVL3 nuclear expression was also lower in in cells adjacent to pTDP-43 aggregates (grains in neuropil, dystrophic neurites passing through the field, or other pTDP-43 signal that cannot be assigned to the cell being measured) (P=0.0072).

We completed a more global survey of nuclear ELAVL3 and TDP-43 expression in neurons from cortical layers 2-6 (Figure 3.9) (see 3.4.4 for selection criteria used for inclusion as a neuron). We excluded oligodendrocytes for this study. Our methods are sufficiently sensitive to detect higher expression of nuclear ELAVL3 in superficial layers 2/3 relative to deeper cortical layers 5/6 (P<0.0001). As predicted from single cell sequencing[93,94], TDP-43 neuronal nuclear expression does not follow this pattern of higher expression in superficial relative to deep cortical layers (P=0.1599). This finding gives us confidence the differences seen between ELAVL3 intensity in superficial and deep cortical layers is not an artifact of fluorescent FFPE staining. Neurons of cortical layers 3 and 5 (excluding Betz cells) have significantly reduced nuclear ELAVL3 fluorescent intensity in ALS relative to controls (layer 3 P=0.0006 and layer 5 P<0.0001). Similarly, we detected

significantly reduced nuclear TDP-43 fluorescent intensity in cortical layers 3 and 5 (both *P*<0.0001).

We observed two striking findings relating to ELAVL3 protein aggregates that we did not observe in control or ALS spinal cord: (1) cells with nuclear depletion of ELAVL3 coupled with intense, granular cytoplasmic ELAVL3 aggregates, and (2) elongated ELAVL3 neuropil structures with a "beads on a string" appearance.

First, we found small neurons and oligodendrocytes/OPCs, predominantly residing in gray matter, with depleted nuclear ELAVL3 and bright granular aggregates distributed throughout the soma and into proximal processes (Figure 3.10A-G'''). Because cells with this ELAVL3 aggregate staining pattern were heterogenous in nuclear size, soma/processes morphology, and spatial location, we believe they belong to multiple motor cortex cell types. Notably, we did not find Betz cells within this population. The majority of cells with this pattern did not show co-occurring TDP-43 pathology (Figure 3.10A-F'''), although we detect isolated examples of cells with low nuclear TDP-43 and/or pTDP-43 aggregates (Figure 3.10G-G'''). Although rare, the ELAVL3 granular aggregate cells were found at a higher frequency in ALS motor cortex relative to control (*P*=0.0364) (Figure 3.10H). They were detected in all ALS motor cortices (n=16/16) compared to less than half of controls (n=2/5). ELAVL3 granular aggregate-containing cells did not appear overtly sick—they did not show evidence of shrinkage artifact, nuclear defects or chromatin condensation, or pTDP-43 aggregates. They did not have elevated expression of phosphorylated histone H2AX (γH2AX), a marker of DNA double strand breaks associated with cell death.

Our second observation relating to ELAVL3 aggregates were sparsely distributed ELAVL3-positive neuropil threads with a "beads on a string" appearance (Figure 3.11A-E"). These strings were sparsely distributed in the gray matter and did not have a particular orientation relative to fibers diving into white matter. We measured strings ranging from less than 10 μm to more than 150 μm. Strings may be much longer, however we were limited to analyzing a limited cross-section of tissue contained within a single cut plane. ELAVL3 strings were more common in ALS motor cortex (14/16 cases) relative to control (1/5 cases), but we did not observe morphologic differences between ALS and control. We most commonly observed individual strings traversing through our visual field, however, we occasionally observed multiple strings bunched together (Figure 3.11E-E'''). We did not observe co-localization of pTDP-43 aggregates, including neuropil threads, with ELAVL3 strings. We also did not observe co-localization with vasculature, which had significant non-specific staining associated with the ELAVL3 antibody.

Figure 3.7. ELAVL3 nuclear depletion in ALS anterior horn lower motor neurons and retention in ALS precentral gyrus upper motor neurons. (**A-B'''**) ELAVL3 with nuclear depletion in spinal cord neurons containing pTDP-43 aggregates. (**C-E'''**) The majority of ELAVL3 and TDP-43 showed normal, nuclear expression in motor cortex Betz cells. Nuclei are highlighted with a dotted yellow line. (**F-G**) Nuclear fluorescent intensity of TDP-43 and ELAVL3 normalized to background staining motor neurons. (**F**) In spinal cord motor neurons, normalized fluorescent intensity of TDP-43 and ELAVL3 were significantly downregulated in ALS compared to control (P<0.0001). (**G**) In motor cortex Betz cells, there is no significant difference between normalized nuclear intensity of TDP-43 or ELAVL3 between ALS and controls. Results are graphed as mean ± SEM and analyzed with Holm-Šídák's multiple-comparisons test.
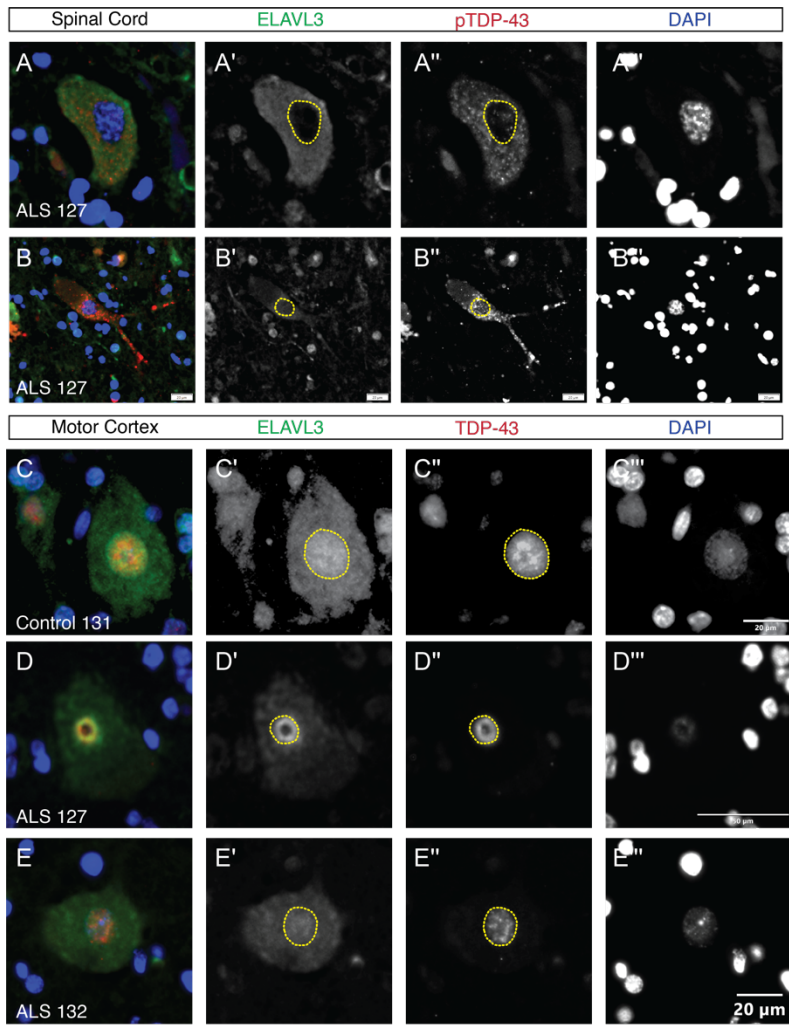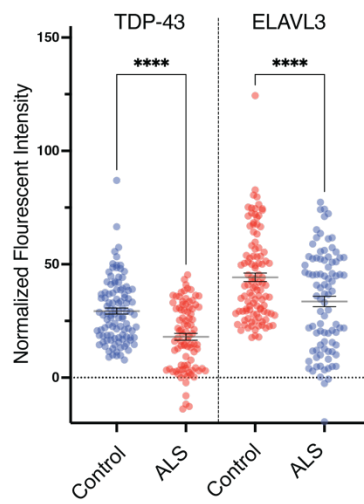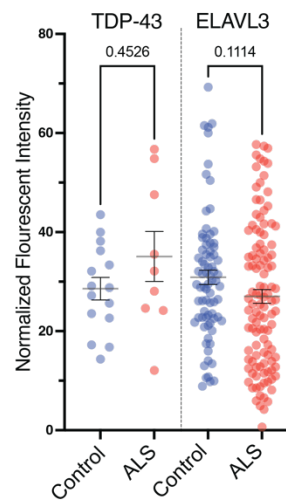
Figure 3.8. Nuclear expression of ELAVL3 in cortical cells with TDP-43 pathology. (**A-E'''**) Representative images of ELAVL3 nuclear expression in cortical cells with TPD-43 nuclear mislocalization and/or cytoplasmic aggregation. Nucleus highlighted with dotted yellow line. (**F**) Nuclear ELAVL3 expression (normalized to background neuropil staining) in cells with no pTDP-43 signal (-) is significantly higher than cells with pTDP-43 intracellular aggregates (*P = 0.0228) and cells proximal to pTDP-43 aggregates (**P = 0.0072)

| Gray Matter | ELAVL3 | TDP-43 | DAPI |

A ALS 132 L3 / A' / A'' / A''' 20 μm

B ALS 96 L2 / B' / B'' / B''' 20 μm

C ALS 122 L3 / C' / C'' / C''' 20 μm

D ALS 118 L3 / D' / D'' / D''' 10 μm

E ALS 119 L3 / E' / E'' / E''' 10 μm

F Nuclear ELAVL3 Expression

Normalized Flourescent Intensity

pTDP-43−   Proximal to TDP-43+   pTDP-43+

*
**

A

ELAVL3 Nuclear Expression by Cortical Layer

B
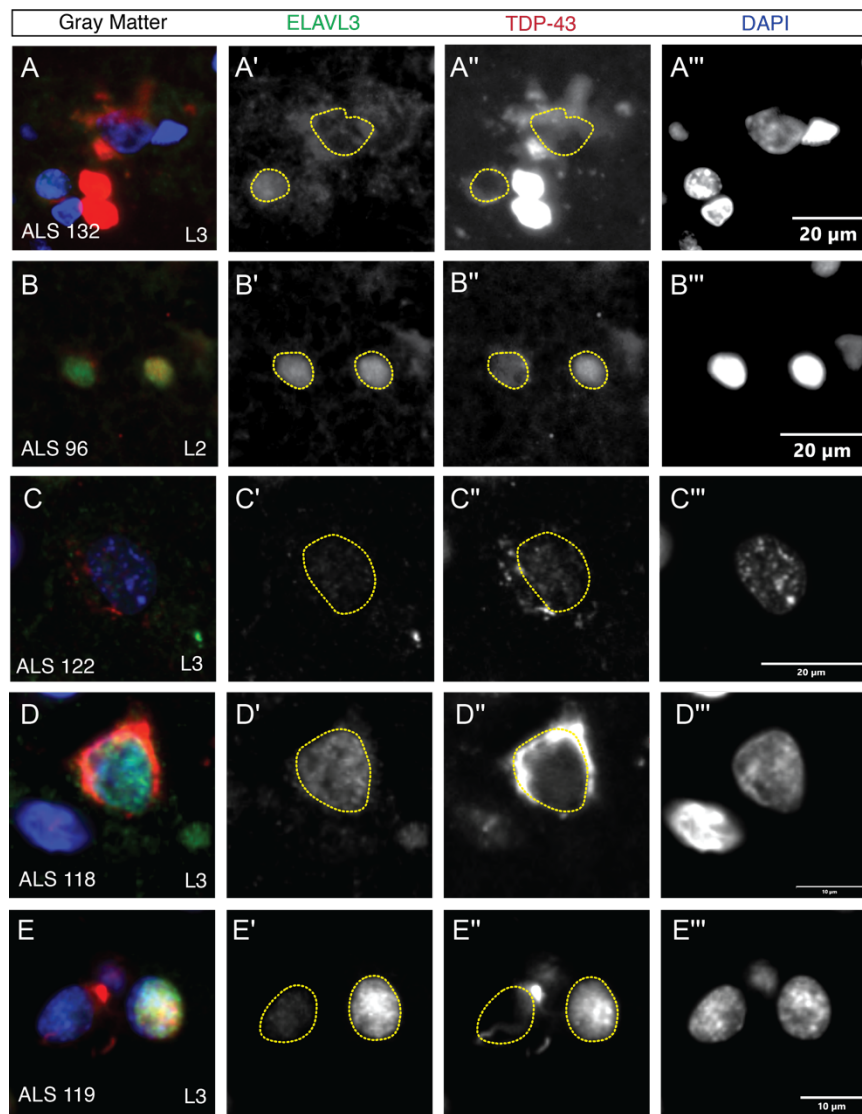
TDP-43 Nuclear Expression by Cortical Layer
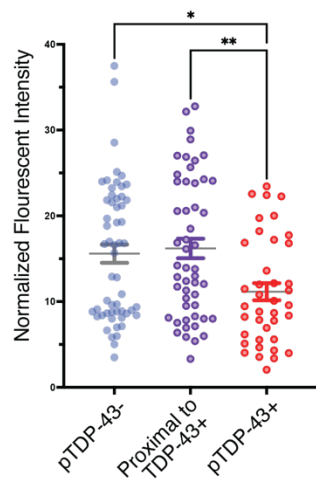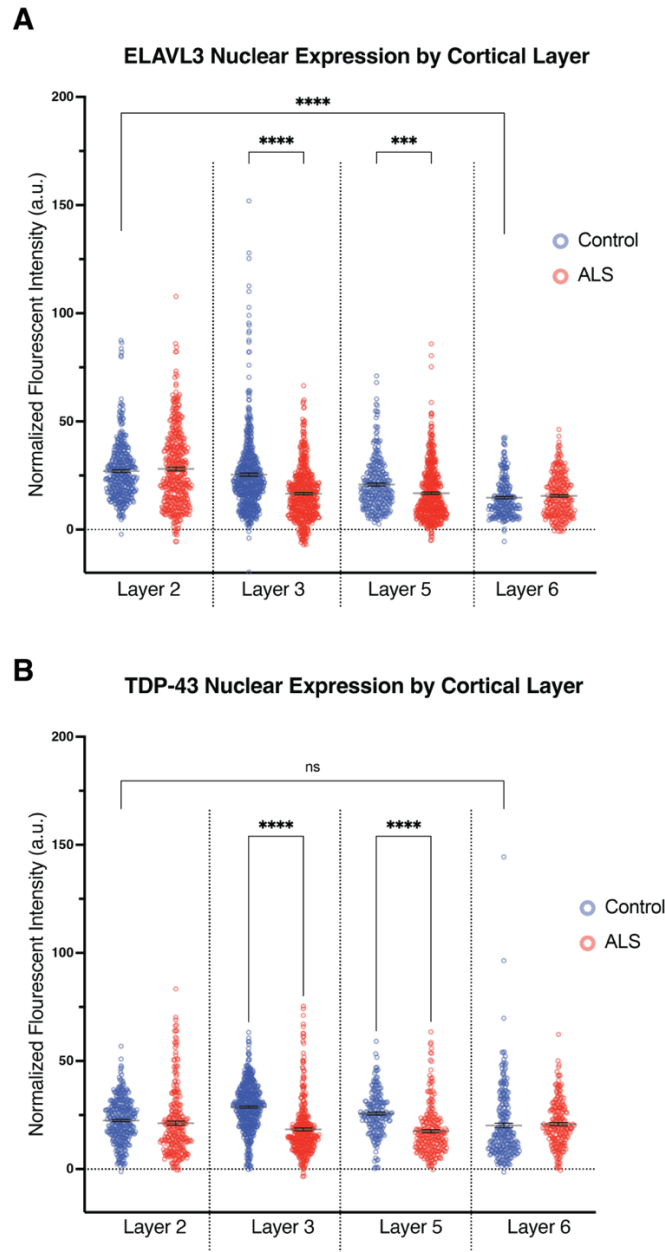
Figure 3.9. ELAVL3 and TDP-43 nuclear downregulation in ALS neurons of L3 and L5.
(**A-B**) Nuclear expression normalized to background staining in cortical layers 2, 3, 5 (excluding Betz cells) and 6 of ELAVL3 (**A**) and TDP-43 (**B**) in control and ALS motor cortex neurons. (**A**) Nuclear intensity of ELAVL3 was significantly higher in control layer 2 relative to control layer 6 ($P < 0.0001$). ELAVL3 was significantly downregulated in ALS compared to controls in cortical layers 3 ($P < 0.0001$) and 6 ($P = 0.0006$). (**B**) Nuclear intensity of TDP-43 was similar in control layer 2 relative to control layer 6 ($P = 0.8000$). TDP-43 was significantly downregulated in ALS compared to controls in cortical layers 3 ($P < 0.0001$) and 6 ($P < 0.0001$). Results are graphed as mean ± SEM and analyzed with a one-way ANOVA and post hoc Holm-Šídák multiple comparisons tests.

Figure 3.10. ELAVL3 nuclear depletion and granular cytoplasmic aggregation in neurons of motor cortex. (**A-G'''**) Representative images of ELAVL3 loss in the nucleus and intense, granular cytoplasmic expression in cortical neurons of control (**A-A'''**) and ALS (**B-G'''**) motor cortex. Nuclear TDP-43 is most often intact within these neurons, but rare examples (**G-G'''**) could be found. (**H**) Cells with abnormal, granular cytoplasmic ELAVL3 staining were more common in motor cortex from ALS (mean: 7.593 cells/tissue section) relative to controls (mean: 1.8 cells/tissue section) $P = 0.0364$. Results are graphed as mean ± SEM and analyzed with a Mann-Whitney U Test.

| Motor Cortex | ELAVL3 | TDP-43 | DAPI |

A | A' | A'' | A'''
Control 131 | | | 20 µm

B | B' | B'' | B'''
ALS 132 | | | 20 µm

C | C' | C'' | C'''
ALS 99 | | | 20 µm

D | D' | D'' | D'''
ALS 117 | | | 10 µm

E | E' | E'' | E'''
ALS 104 | | | 10 µm

F | F' | F'' | F'''
ALS 121 | | | 10 µm

G | G' | G'' | G'''
ALS 117 | | pTDP-43 | 10 µm
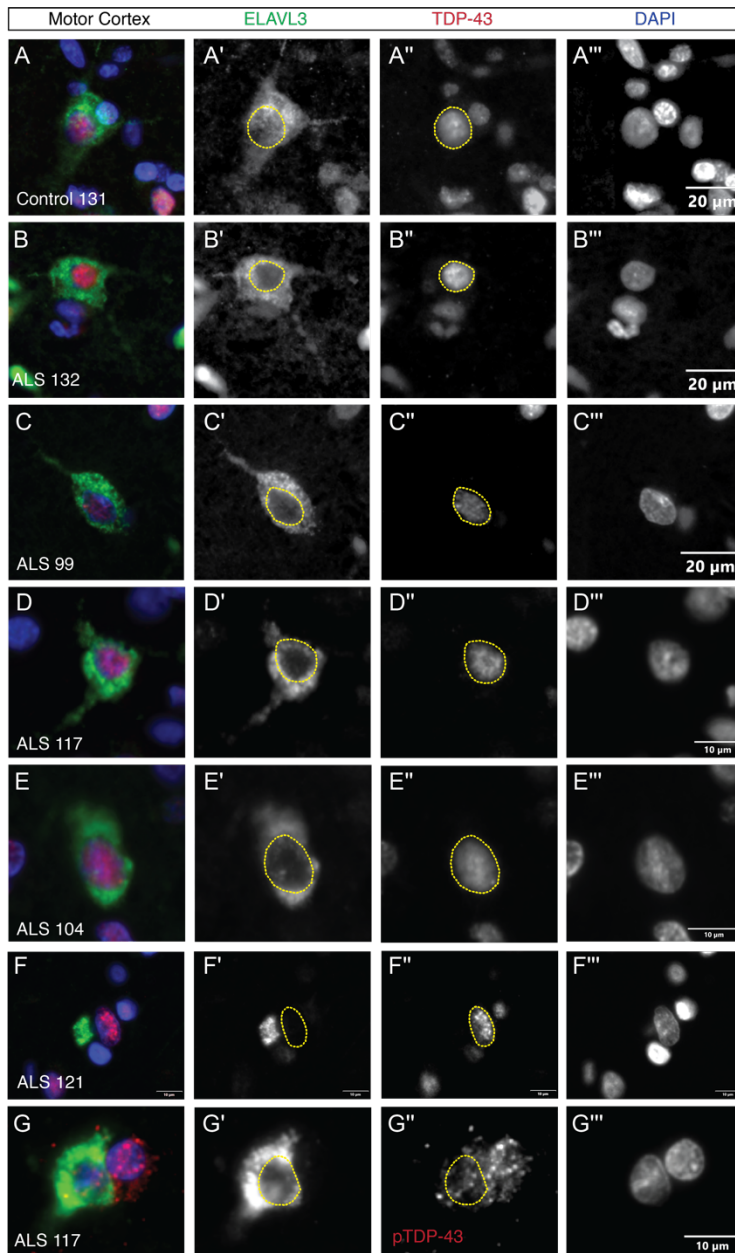
H Granular ELAVL3 Tranlocation in Motor Cortex

0.0364

Cells per section

Control   ALS
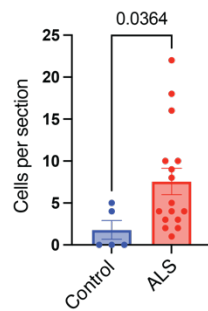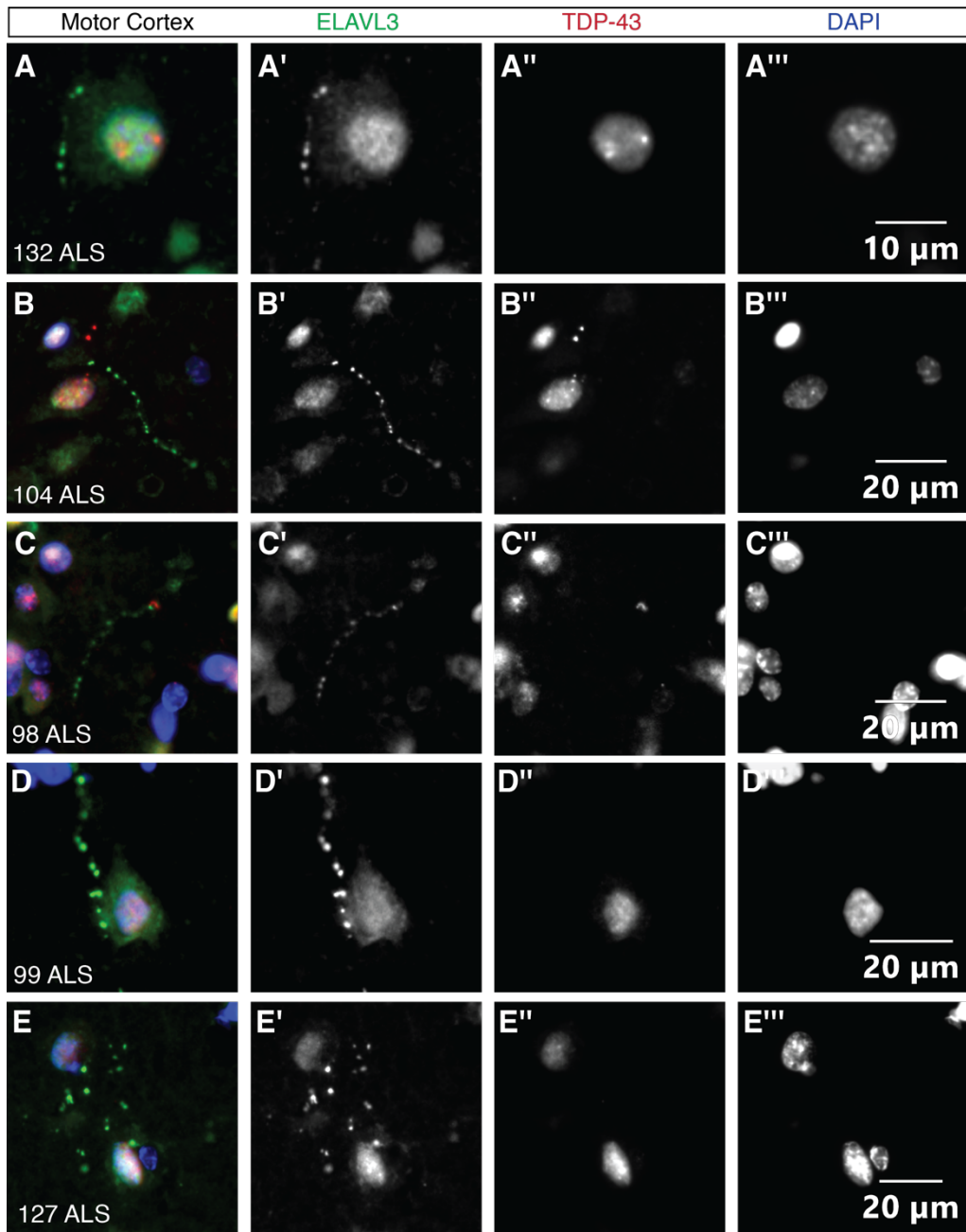
Figure 3.11. ELAVL3 threads within ALS motor cortex tissue. (**A-E'''**) Representative images of ELAVL3 string-like aggregates within the neuropil of ALS motor cortex tissue. Aggregates have a "beads on string" morphology and did not co-localize with TDP-43 aggregates.

3.2.5 Western immunoblotting of ELAVL3 in motor cortex shows trends in downregulation and novel protein isoform expression

In our previous study, we described reduction in ELAVL3 protein expression (39 kDa) in ALS spinal cord compared to controls using Western immunoblotting with anti-ELAVL3 N-terminus rabbit polyclonal antibody Proteintech 55047-AP (lot #09000021)[5]. Using this particular lot of antibody, we detected a 36kDa band enriched in ALS cases relative to controls, and it was hypothesized that this band represented a novel short ELAVL3 isoform. This isoform did not correspond to any known ELAVL3 variants or predicted truncated proteins generated from use of a premature stop sequence within cryptic exon 4a (predicted weight ~12 kDa). It also did not correspond to any known protein isoforms of the nELAVL family (ELAVL2: 43.6, 39.5, 38.0, 20.7, 10.1 kDa; ELAVL3: 39.5, 38.9, 9.7; ELAVL4: 42.4, 41.8, 40.4, 40.8 kDa[96]).

We repeated immunoblotting with the same processed spinal cord samples used in the previous publication[5] (control n = 5, ALS n = 5). We probed for ELAVL3 protein with new concentrated lots of Proteintech 55047-AP anti-ELAVL3 antibody (Figure 3.12A). We detected a narrow doublet around 39-40 kDa across all samples that we quantified together as a single band. Expression of these ELAVL3 isoforms was decreased in ALS spinal cord relative to controls (Figure 3.12B). However, this decrease was less dramatic than previously described (Figure 3.12C). We did not detect any smaller ELAVL3 isoforms, including the previously seen 36 kDa band or predicted truncated isoforms from cryptic exon expression.

In the motor cortex, we detected a 39 kDa band in all samples that corresponds to the major isoform of ELAVL3 (Figure 3.12D). This isoform trended toward downregulation

in UMN predominant ALS cases (UMN ALS) relative to controls (P=0.0846) more than LMN predominant ALS (LMN ALS) (P=0.1234) (Figure 3.12E). We also detected an isoform at approximately 49 kDa in nearly all samples (Figure 3.12F). There was a large variation in expression within the control group, precluding evaluation between groups.
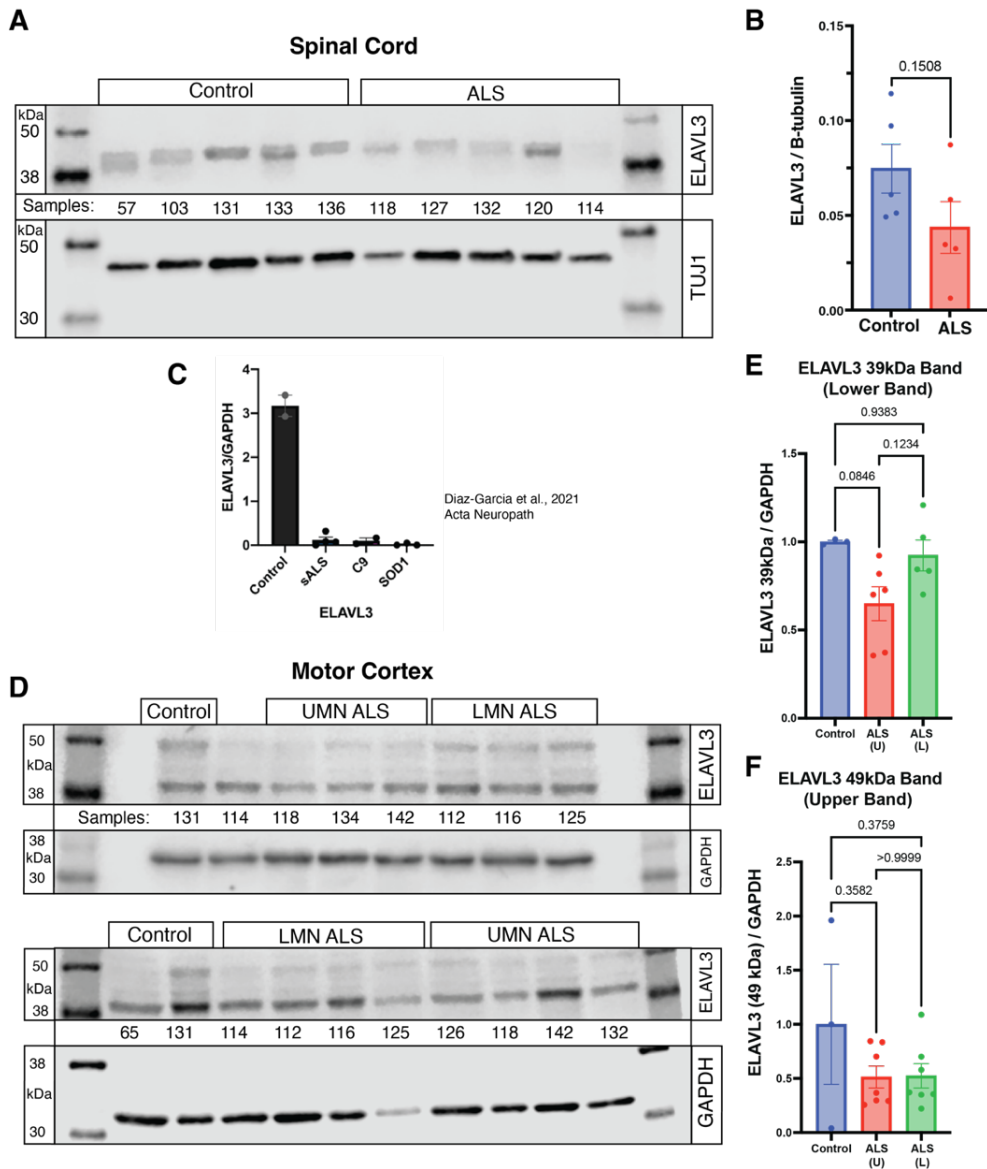
Figure 3.12. Immunoblotting for ELAVL3 in spinal cord and motor cortex show trends toward downregulation in ALS and expression of novel long isoforms. (**A-B**) Immunoblot for ELAVL3 in spinal cord (n = 5 controls, n = 4 ALS) using n-terminal-targeting Proteintech 55047-AP antibody demonstrates a trend in ELAVL3 reduction (P = 0.1508, Mann-Whitney U-test), (**C**) less strong than demonstrated in the previously published study[5]. (**D**) Western blot for ELAVL3 in motor cortex (n = 2 controls, n = 5 ALS upper-motor neuron predominant (UMN), n = 4 ALS lower-motor neuron predominant (LMN) show two bands, one expected at 39 kDa and a higher molecular weight 49 kDa band. (**E**) There is a nearly significant change in the 39 kDa band between controls and ALS UMN (P = 0.0846) and between ALS UMN and LMN (P = 0.1234). (**F**) The 49 kDa band does not show a significant difference between diagnoses.

3.2.6 Descriptions of aggregate pathology in FTLD-TDP43 and FTLD-Tau frontal cortices

For our study of ELAVL3 in FTLD frontal cortex, we examined FFPE sections from control (n=4), FTLD-TDP43 (n=5), and FTLD-Tau (n=5) cases. To characterize pTDP-3 pathology, we utilized the same antibody as previously (see 3.2.3) and assigned a pathologic subtype using 2017 criteria based on the presence of neuronal or glial inclusions and dystrophic neurites (Table 1.1)[45]. Our analyzed cases varied in pathologic subtypes and burden of pTDP-43 microscopic pathology (Table 3.3). We did not observe cases with pTDP-43 pathology matching pathologic subtypes C and D, corresponding to long neuritic dendrites and lentiform inclusions, respectively. pTDP-43 pathology, predominantly granulofilamentous inclusions or short dystrophic neurites, was spread throughout the cortical layers.

To characterize pTau pathology, we utilized an antibody capable of detecting both 3R and 4R hyperphosphorylated tau aggregate species (AT8 monoclonal antibody targeting Ser202/Thr205). With this antibody we can detect tau aggregates containing equal amounts of 3R and 3R tau (intracellular tangles in normal aging or Alzheimer's disease), aggregates containing predominantly 3R tau (Pick bodies in Pick's disease), or aggregates containing predominantly 4R tau (glial/neuronal inclusions in corticobasal degeneration and progressive supranuclear palsy). Within our cohort, we detected a variety of intracellular pTau aggregates in both neurons and glia including intraneuronal tangles, Pick bodies, tufted astrocytes/astrocytic plaques, and, most commonly, oligodendrocyte coiled bodies (Table 3.4).

We did not observe a difference in the range of aggregate burden (pTDP-43 or pTau), from sparse to severe, between disease groups (ALS motor cortex, FTLD-TDP43 frontal cortex, or FTLD-Tau frontal cortex). Between ALS and FTLD-TDP43, we did not observe differences in pTDP-43 aggregate morphologies. Given our small sample sizes, we do not have power to subdivide disease groups by histologic subtype and interpret changes in ELAVL3 pathology. However, can demonstrate similarities and differences across disease groups relative to control.

Table 3.3. FTLD-TDP43 frontal cortex pathological characteristics.

Case	pTDP-43 pathology description	Pathologic Subtype
5713	Sparse, small neuronal inclusions	Type B
5782	Sparse small, granular oligodendroglial inclusions in white matter	Type E
5869	Moderate/severe short dystrophic neurites in cortical gray matter, sparse neuronal inclusions	Type A
5880	Very sparse neuronal inclusions	Type A
5916	Moderate neuronal inclusions and short dystrophic neurites	Type A

Table 3.4. FTLD-Tau frontal cortex pathological characteristics.

Case	pTau pathology description
5734	Moderate neuronal intracellular tangles, moderate oligodendrocyte coiled bodies
5739	Moderate oligodendrocyte coiled bodies, moderate intracellular tangles, mild astrocytic plaques
5745	Sparse oligodendrocyte coiled bodies
5827	Severe astrocytic plaques, severe oligodendrocyte coiled bodies, mild neuronal intracellular inclusions
5860	Pick neurons with inclusions, mild short threads

3.2.7 Triad of ELAVL3 findings in FTLD-TDP43 and FTLD-Tau frontal cortices

Given the fluid spectrum between ALS and FTLD, we hypothesized ELAVL3 dysregulation would be a shared feature in disease-affected cortex. In our analysis of FTLD-TDP43 and FTLD-Tau frontal cortex, we observed three key findings that mirrored changes in ALS motor cortex: (1) measurable reduction in ELAVL3 nuclear intensity in pTDP-43-associated or pTau-associated neurons (without total ELAVL3 nuclear loss), (2) rare cells marked by loss of ELAVL3 nuclear staining and presence of intense, granular cytoplasmic staining, and (3) ELAVL3-filled dystrophic neurites with a "beads on a string" form.

In FTLD-TDP43 and FLTD-Tau frontal cortex, the majority of neurons and oligodendrocytes have enriched expression of ELAVL3 in the nucleus relative to the cytoplasm. Like ALS motor cortex, in cells that contain pathologic aggregates (pTDP-43 or pTau), we did not detect total depletion of ELAVL3 from the nucleus (Figures 3.13-3.14); in contrast, ALS spinal cord motor neurons most often experienced total loss of nuclear ELAVL3 with pTDP43 aggregates (Figure 3.4A-B). To capture subtle decreases in nuclear ELAVL3 expression, we measured the fluorescent intensity of nuclear ELAVL3 in cells with phosphorylated aggregates compared nearby neighbors without aggregates (methods described in 3.4.6). In both pTDP-43 aggregate containing cells and pTau aggregate containing cells, ELAVL3 has significantly reduced expression compared to non-aggregate containing cells (Figure 3.15).

Like ALS motor cortex, in FTLD-TDP43 and FTLD-Tau frontal cortex we observed examples of rare cortical cells characterized by depleted nuclear ELAVL3 and expression of granular cytoplasmic ELAVL3 aggregates in the soma and proximal processes (Figures 3.16-3.17). Across groups, this cellular population shared similar ELAVL3 morphology

(bright granules distributed throughout the soma and into proximal processes) and cortical distribution (predominantly in cortical layers 2-6 and less frequently in white matter). In both FTLD-TDP43 and FTLD-Tau, we detected a slight trend towards increased frequency compared to control frontal cortex (Figure 3.17F). Within our FLTD-TDP43 cohort, we did not observe co-localization of TDP-43 pathology with this granular cell population. However, we did observe examples of cells co-expressing intracellular pTau and ELAVL3 pathology within out FLTD-Tau cohort (Figure 3.17E-E'''). There was little overlap visualized between pTau structures and ELAVL3 granules, thus we hypothesize ELAVL3 is not sequestered within pTau aggregates.

Finally, we visualized ELAVL3-positive neuropil strings distributed sparsely throughout the gray and white matter in frontal cortex from both FTLD cohorts (Figure 3.18). As in ALS motor cortex, the ELAVL3 structures appeared as a thin string with swollen bulbous structures, giving a "beads on a string" appearance. The measured length was ranged from less than 10 μm to over 130 μm. In FLTD-TDP43, we did not detect co-localization with pTDP-43 aggregates (Figure 3.18 A-C'''). However, in many FTLD-Tau cases there was extensive pTau pathology spread throughout astrocytic arbors. While ELAVL3 strings did not localize to these pTau aggregates, we often observed the two pathologies in close proximity (Figure 3.18 D-G'''). We did observe co-localization of strings with vasculature or other notable features.

We summarized the ELAVL3 aggregate findings in Table 3.5.
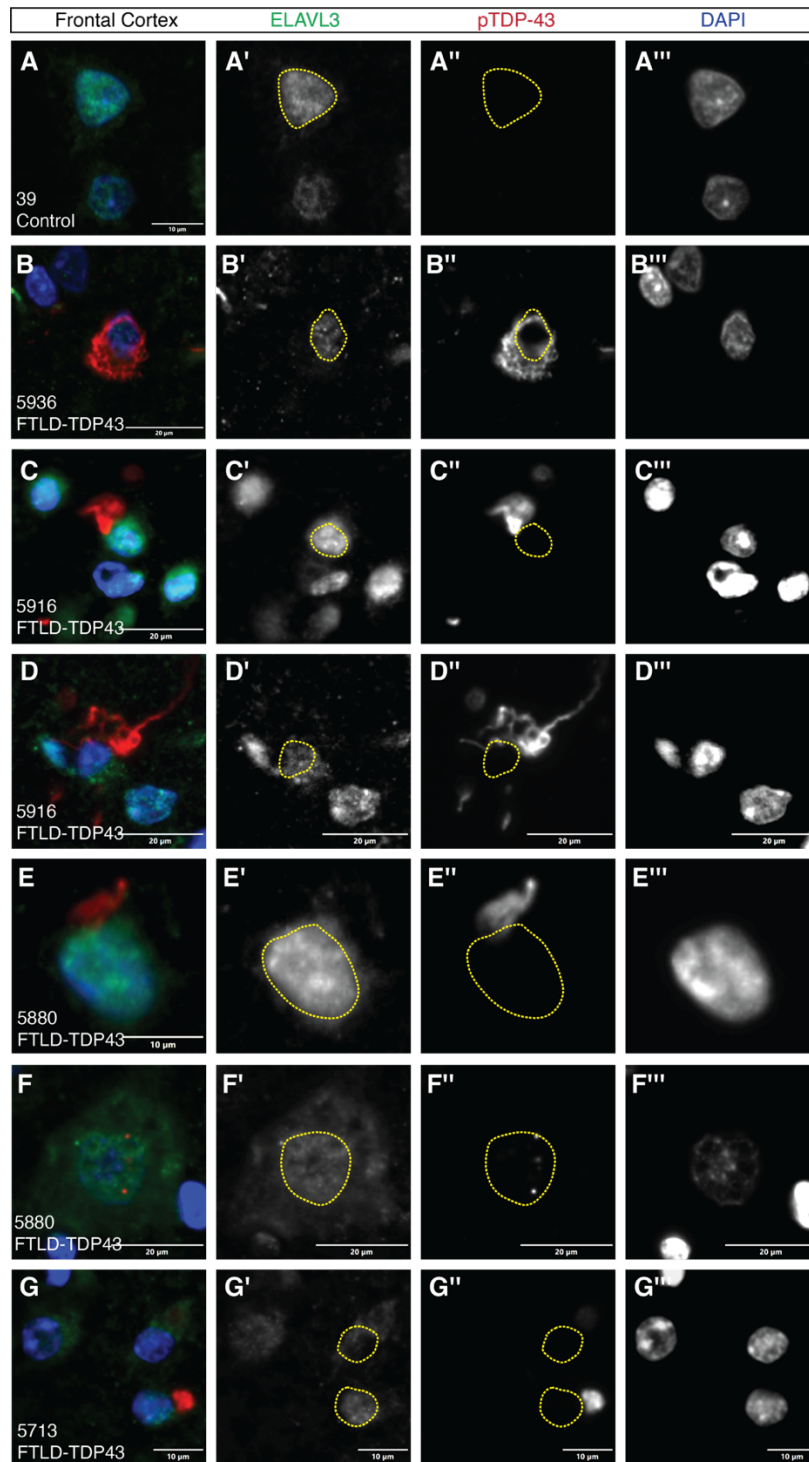
Figure 3.13. ELAVL3 staining in neurons and oligodendrocytes of frontal cortex with pTDP-43 cytoplasmic aggregates. (**A**) Control neuron with normal nuclear ELAVL3 and no pTDP-43 aggregates. (**B-F'''**) Neurons with pTDP-43 cytoplasmic aggregates and variable levels of nuclear ELAVL3. (**G-G'''**) Oligodendrocyte with pTDP-43 aggregate and normal levels of ELAVL3.
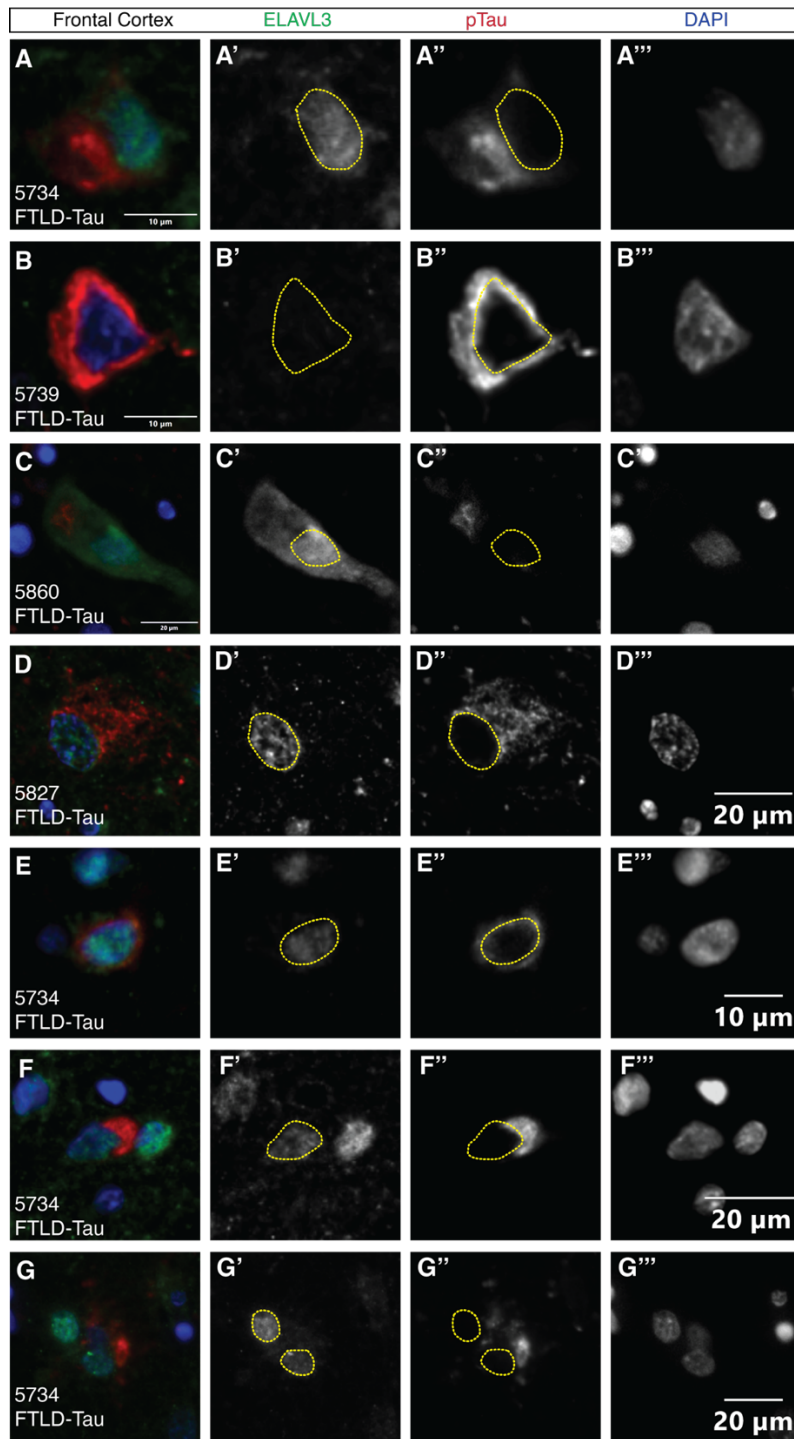
Figure 3.14. ELAVL3 staining in neurons and oligodendrocytes of frontal cortex with pTau cytoplasmic aggregates. (**A-G'''**) Representative images of cells with intracellular phosphorylated tau aggregates. Yellow dotted line indicates nuclear shape.

ELAVL3 Nuclear Expression
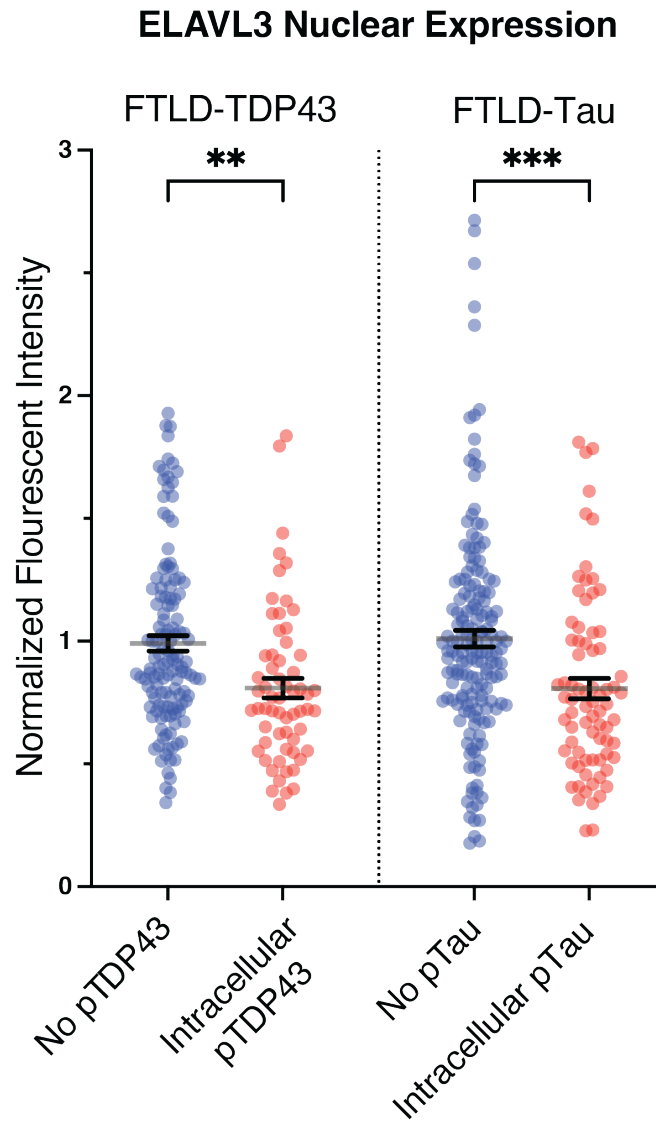
Figure 3.15. Nuclear fluorescent intensity of ELAVL3 is reduced in aggregate-containing cells of FTLD-TDP43 and FTLD-Tau cortex. Cells with intracellular pTDP43 aggregates have significantly lower nuclear ELAVL3 expression compared to cells with no aggregates (**$P = 0.0048$). Cells with intracellular pTau aggregates have significantly lower nuclear ELAVL3 expression compared to cells with no aggregates (***$P = 0.0003$). Results are graphed as mean ± SEM and analyzed with a Mann-Whitney U Test.
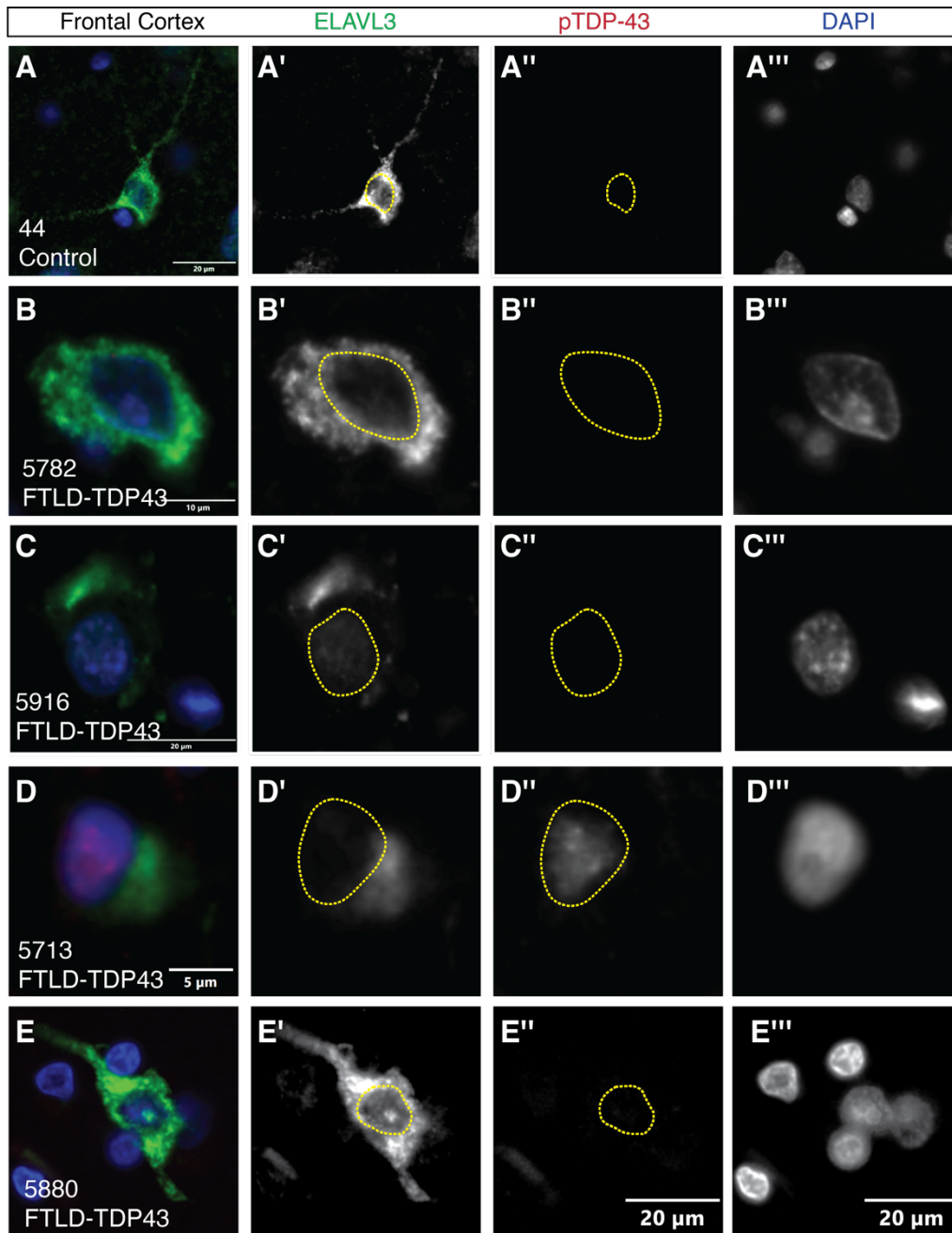
Figure 3.16. Granular, cytoplasmic ELAVL3 staining in cells from FTLD-TDP43 frontal cortex.
(A-A''') Control neuron demonstrating normal ELAVL3, which is enriched in the nucleus relative to the cytoplasm and can have a speckled appearance in the cytoplasm. **(B-E''')** FTLD-TDP43 neurons demonstrating nuclear loss of ELAVL3 and bright, granular staining distributed in the soma and into proximal processes. Yellow dotted line indicates nuclear shape.

Figure 3.17. Granular, cytoplasmic ELAVL3 staining in cells from FTLD-Tau frontal cortex. **(A-D''')** Representative images of FLTD-TDP43 cells with depletion of nuclear ELAVL3 and expression of granular ELAVL3 in the soma and proximal processes. **(E-E''')** Representative images of a cell with granular cytoplasmic ELAVL3 expression and pTau cytoplasmic aggregates. Yellow dotted line indicates nuclear shape. (**F**) ALS motor cortex (MC) has a significantly higher expression of granular ELAVL3 cells relative to control (*P = 0.0364). There was a slight trend towards increased frequency of these cells in FTLD-TDP43 frontal cortex (FR) (P = 0.2143) more than FTLD-Tau frontal cortex (P = 0.6190). Results are graphed as mean ± SEM and analyzed with a Mann-Whitney U Test.

| Frontal Cortex | ELAVL3 | pTau | DAPI |

A — 5860 FTLD-Tau
A' | A'' | A''' — 20 μm

B — 5827 FTLD-Tau
B' | B'' | B''' — 20 μm

C — 5734 FTLD-Tau
C' | C'' | C''' — 20 μm

D — 5734 FTLD-Tau
D' | D'' | D''' — 20 μm

E — 5739 FTLD-Tau
E' | E'' | E''' — 20 μm

F Granular Cytoplasmic ELAVL3

Number of Cells / Tissue Section

*

Control MC, Control FR, ALS MC, FTLD-TDP FR, FTLD-Tau FR
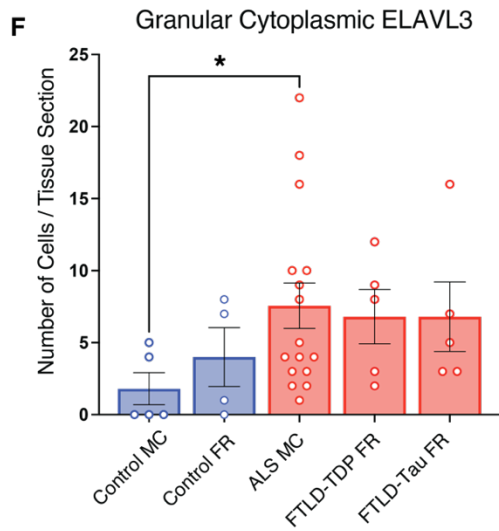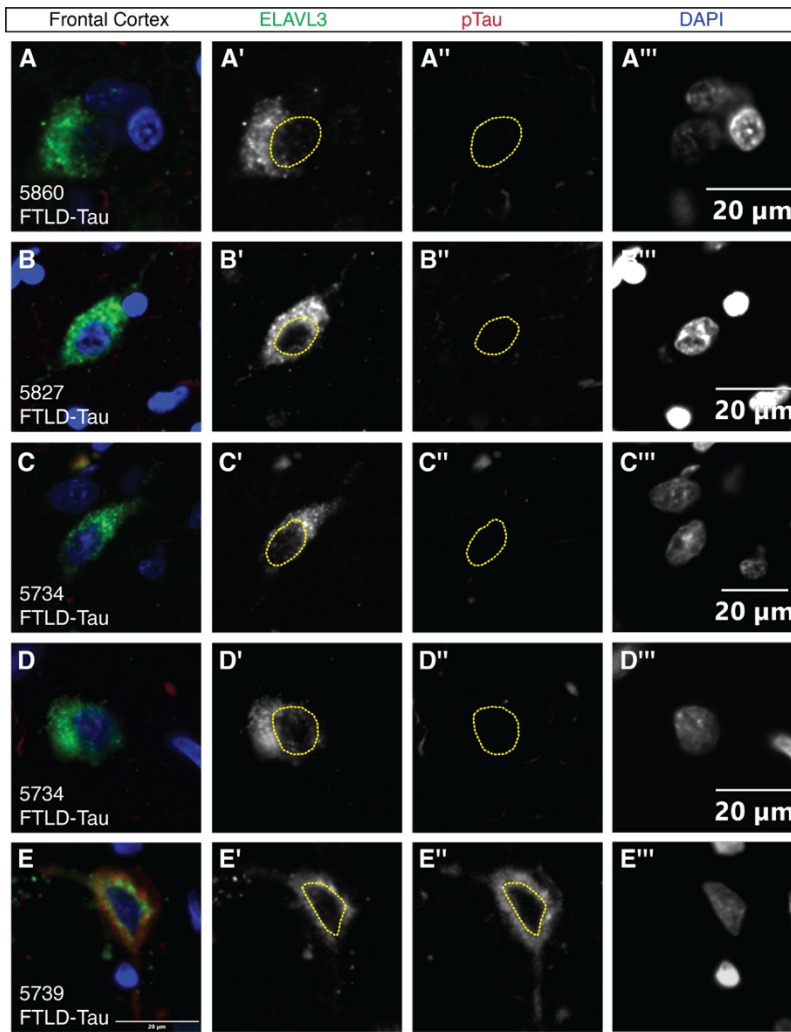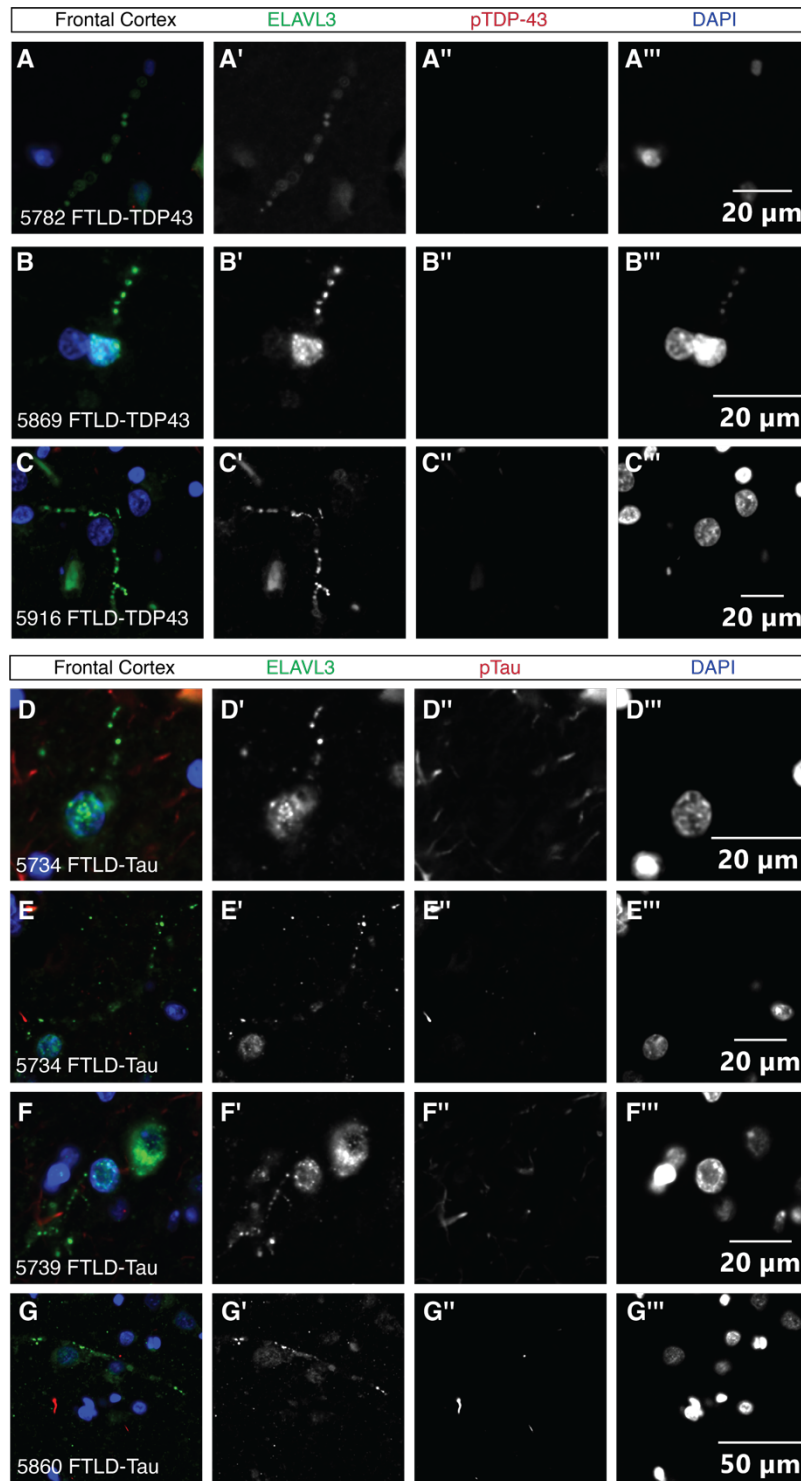
Figure 3.18. ELAVL3 strings are present in FTLD-TDP43 and FTLD-Tau frontal cortex. (**A-C'''**) Representative images of ELAVL3 strings in frontal cortex of FTLD-TDP43 without overlapping pTDP-43 pathology. (**D-G'''**) Representative images of ELAVL3 threads in FLTD-Tau, often in the same field as pTau aggregates within astrocytic processes.

Table 3.5. Burden of ELAVL3 pathology including cells with granular cytoplasmic ELAVL3 aggregates and ELAVL3 threads.

Cells with granular ELAVL3 aggregates
Frequency per section

0 5 10 15 20+

ELAVL3 string-like extracellular aggregates

Absent | Present

Region	Case	Diagnosis	Granular Aggregates	String Aggregates
Motor Cortex	40	Control		Absent
	44	Control	~5	Absent
	103	Control		Absent
	115	Control	~5	Present
	131	Control		Absent
	98	FALS C9	~10	Present
	117	FALS C9	~20+	Present
	120	FALS/FTLD C9	~10	Present
	110	SALS	~5	Present
	127	SALS	~20+	Present
	128	SALS	~5	Absent
	121	SALS	~5	Present
	132	SALS	~20+	Present
	48	SALS	~5	Present
	122	SALS	~15	Present
	119	SALS	~5	Absent
	34	SALS	~10	Present
	99	SALS	~20+	Present
	118	SALS	~5	Present
	104	SALS/FTLD		Present
	96	SALS/FTLD		Present
Frontal Cortex	33	Control	~10	Absent
	44	Control	~10	Present
	39	Control		Absent
	133	Control		Absent
	5869	FTLD-TDP43	~5	Present
	5880	FTLD-TDP43	~20+	Present
	5916	FTLD-TDP43	~10	Present
	5713	FTLD-TDP43	~5	Absent
	5782	FTLD-TDP43	~10	Present
	5734	FTLD-Tau	~20+	Present
	5739	FTLD-Tau	~10	Present
	5745	FTLD-Tau	~5	Absent
	5827	FTLD-Tau	~10	Absent
	5860	FTLD-Tau	~5	Present

3.3 Discussion

ELAVL3 is an RBP that experiences major disturbances in ALS spinal cord at the level of transcript, protein, and subcellular localization[5]. Total nuclear loss of ELAVL3 is a common feature of anterior horn motor neurons, and it appears to be unlinked to, or perhaps upstream of, TDP-43 pathology. We used antibody detection of ELAVL3 in postmortem tissue to determine if it experiences similar downregulation or nuclear depletion in related proteinopathies: ALS motor cortex, FTLD frontal cortex with TDP-43 proteinopathy, and FTLD frontal cortex with tau proteinopathy.

We described the morphology of phosphorylated TDP-43 or tau aggregates within our tissue cohorts, and, as possible, we assigned pathological subtypes. In ALS motor cortex, we used recently published criteria for pTDP-43 subtypes[81] to demonstrate that upper motor neuron findings (increased tone, spastic paralysis, increased deep tendon reflexes, etc.) are predominantly associated with subtypes B and E, which have a higher pTDP-43 burden than subtype SC. To our knowledge, this is the first report combining upper vs lower motor neuron clinical phenotype with motor cortex pTDP-43 subtype. ALS-TDP type B and E resemble FTLD-TDP type B and E (for which they are named) and are characterized by round neuronal cytoplasmic inclusions in superficial and deep cortical layers (type B) and granulofilamentous neuronal inclusions, grains, and oligodendroglial inclusions (type E).

The majority of our FTLD-TDP43 frontal cortex cohort was assigned subtype A, characterized by short dystrophic neurites and neuronal inclusions in the superficial layers and white matter. Less commonly, we identified subtype B and E, both of which have pathology spread through superficial and deep cortical layers and white matter[44,45]. The

majority of FTLD-Tau cases (4/5) showed glial phosphorylated tau pathology more associated with corticobasal degeneration and/or progressive supranuclear palsy. However, we did not subcategorize our cases as we did not have access to the distribution of tau staining across the whole cortex and brainstem.

In our previous examination of ALS anterior horn lower motor neurons, total ELAVL3 loss was a clear and common feature. Nearly 75% of these neurons showed total loss of nuclear ELAVL3. We hypothesized that in Betz cells of the primary motor cortex would show similar dysregulation of ELAVL3. To our surprise, we found Betz cells were resilient to the presence of TDP-43 pathology and maintained enriched nuclear expression of ELAVL3. Given ELAVL4 is the family member expressed in the large projecting Betz cells, we also confirmed there is no changes in expression seen between ALS and control.

We did, however, identify populations of cells that show reduced nuclear ELAVL3 expression in ALS. Neurons within layer 3 (predominantly pyramidal neurons) and layer 5 (predominantly smaller non-Betz neurons) of ALS motor cortex had reduced nuclear ELAVL3 compared to control. Neurons and oligodendrocytes with pTDP-43 intracellular aggregates or proximal to pTDP-43 aggregates also show reduced nuclear ELAVL3. We conclude that, in ALS, motor cortex upper motor neurons are more resilient than spinal cord lower motor neurons to stimuli that induce nuclear depletion of ELAVL3. Spinal cord anterior horn motor neurons are unique in their sensitivity and common loss of nuclear ELAVL3 is a feature rare in cortex.

We described two unique aggregate findings in cortex not observed in spinal cord: (1) a population of cells with ELAVL3 nuclear loss and bright, intense staining filling the

soma and proximal process, and (2) ELAVL3 threads with a "beads on a string" appearance found in superficial and deep cortical layers as well as white matter.

We have confidence the ELAVL3 granular population is not a single, uniform subpopulation. The granular cell population is heterogenous and includes both oligodendrocytes and neurons, including small pyramidal neurons; Betz cells and other glia did not show this pattern of ELAVL3 staining. Nuclear ELAVL3 loss and granular aggregates in the cytoplasm was seen in ALS spinal cord[5]. Our granular cell population was similar; however, we noted two main differences: (1) the cortical granular population described in this study had an intensely bright fluorescent signal distributed throughout the soma relative to expression in neighboring cells, and (2) absence of TDP-43 pathology (nuclear loss or pTDP-43 cytoplasmic aggregates). We observed very rare examples of TDP-43 pathology overlapping with these granular cells. The ELAVL3 granular population does not appear unhealthy or dying. When examining nuclear morphology of these cells, we do not detect pyknosis, karyolysis, or karyorrhexis. We do not see shrinkage artifact or nearby reactive gliosis. They do not show nuclear DNA fragmentation associated with apoptosis. This population was present at a higher frequency in ALS motor cortex compared to control. In FTLD frontal cortex, there is a moderate trend toward increased frequency compared to control. FLTD-Tau, we identified rare examples of intracellular phosphorylated tau aggregates within a cell with bright ELAVL3 granular specks in the soma. Within the soma, there was little overlap of signal, which gives us confidence that ELAVL3 is not stuck within tau aggregates. We hypothesize that nuclear translocation and granularization of cytoplasmic ELAVL3 may be a response to cellular stress but not an indicator of active

apoptosis. Cortical cells of adult or aged frontal lobe may be especially vulnerable to this stress.

We also visualized an abundance of ELAVL3-positive strings distributed throughout the superficial and deep neuropil and occasionally white matter. The strings are consistent in appearance, but range in size. They resemble the granular appearance of the cell population we described above, and we have some visual evidence linking these cells to the strings. However, we cannot attribute all of the strings to the processes of the granular cells as the overall population is small, and we do not detect an increased density of strings surrounding the granular cells. Although they are reminiscnet of dystrophic neurites, we found no co-localization between the threads and pTDP-43 pathology.

By exploring FTLD-Tau frontal cortex, we confirmed that it shares many features of ELAVL3 misbehavior with ALS motor cortex and FTLD-TDP43 frontal cortex. Importantly, cells containing phosphorylated aggregates, whether TDP-43 or tau, had reduced ELAVL3 in the nuclues. ELAVL3 nuclear loss could be a unifying feature between the two disease phenotypes and points towards a uniform role for ELAVL3 in cells experiencing protein aggregate-related stress. Indeed, in ALS mediated by autosomal dominant mutations in SOD-1, which has protein aggregates other than TDP-43 or tau, there was ELAVL3 nuclear loss[5]—another indicator nuclear ELAVL3 translocation is a shared marker of proteinopathies. Further studies are required to confirm ELAVL3 pathology in other cortical proteinopathies including Alzheimers' disease (which can have amyloid beta, tau, and TDP-43 pathology) and Lewy Body Dementia/Parkinson's disease (which has synuclien aggregation).

We predict ELAVL3 nuclear depletion within cortical cells results in reduction of ELAVL3 splice function. *ANK3,* which encodes ankyrin-G, is one ELAVL3 target who requires nuclear binding to splice transcripts meant for mature neurons; with ELAVL3 loss, the phenotype of this protein is one meant for developing neurons and maintenance of axonal polarity is perturbed[60]. ELAVL3 has binding domains on both *MAPT* and *TARDBP*. Nuclear exit of ELAVL3 could mean that these targets, already part of an abberant protein production pathway, could be further deregulated at the transcript level. Given ELAVL3's role in stabilizing transcripts by binding on the 3'UTR, this could mean reduced transcript levels.

3.4 Materials and methods

3.4.1 Human postmortem tissue

De-identified human tissues were obtained from two sources. The UCSD ALS tissue repository was created following HIPAA-compliant informed consent procedures approved by Institutional Review Boards (either Benaroya Research Institute, Seattle, WA IRB# 10058 or University of California San Diego, San Diego, CA IRB# 120056) and the UCSD Shiley-Marcos Alzheimer's Disease Research Center (NIA P30 AG062429).

Table 3.6: Demographic data of tissue used in immunofluorescent studies.

Case	Pathologic Diagnosis	UMN, LMN predominance	Site of Onset	Age	Sex	PMI	Region Analyzed
31	Control			67	M	3.5	FR
34	SALS	U>L	Bulbar	81	F	3.5	MC
39	Control			-	-	-	FR
40	Control			76	F	5	MC
44	Control			80	F	5	MC, FR
48	SALS	U=L	Bulbar	67	M	6	MC
96	SALS/FTLD	U>L	Bulbar	67	F	3.5	MC
98	FALS, C9	U=L	Bulbar	69	F	5	MC
99	SALS	U>L	Bulbar	70	F	4	MC
103	Control			92	F	10	MC
104	SALS/FTLD			74	M	12	MC
110	SALS	SALS		53	M	9	MC
115	Control			94	M	>24	MC
117	FALS, C9	U>L	Bulbar	66	F	12	MC
118	SALS	U>L	Bulbar	56	F	4	MC
119	SALS	U>L	Arm	46	M	>24	MC
120	FALS/FTLD, C9	U>L	Bulbar	64	M	9	MC
121	SALS	U=L	Arm	67	M	3	MC
122	SALS	U=L	Bulbar	69	F	4.5	MC
127	SALS	L>U	Arm/Resp	67	M	6	MC
128	SALS	L>U	Foot	69	F	5.5	MC
131	Control			56	M	2.5	MC
132	SALS	U=L	Arm	64	F	6.5	MC
133	Control			76	M	7.5	FR
5713	FTLD-TDP43			81	F	12	FR
5782	FTLD-TDP43			68	M	33	FR
5869	FTLD-TDP43			66	M	-	FR
5880	FTLD-TDP43			75	F	-	FR
5916	FTLD-TDP43			70	M	-	FR
5739	FTLD-Tau			61	M	9	FR
5745	FTLD-Tau			72	F	13	FR
5827	FTLD-Tau (CBD)			80	M	7	FR
5860	FTLD-Tau			89	M	-	FR
5935	FTLD-Tau			77	M	3	FR

Table 3.7: Sample number for spinal cord immunofluorescence studies.

Immunofluorescence: Spinal Cord			
Region	Diagnosis	Cases	Number of Cells
Spinal Cord	Control	2	90
	ALS	2	106

Table 3.8: Sample number for motor cortex immunofluorescence studies.

	Immunofluorescence: Motor Cortex					
	Layer 2	Layer 3	Layer 5	Betz Cells	Layer 6	
Control 5 cases	389	605	288	78	226	No. of Cells
ALS 16 cases	445	550	525	112	269	

Table 3.9: Sample number for phospho-aggregate versus no aggregate cell analysis.

	Pathology	Cells
ALS MC	No pTDP	39
	pTDP Adjacent	51
	Intracellular pTDP	56
FTLD-TDP43	No pTDP-43	132
	Intracellular pTDP	62
FTLD-Tau FR	No pTau	171
	Intracellular pTau	76

3.4.2   Cell line acquisition

In collaboration with Synthego (Redwood City, CA), CRISPR/Cas9 was used to generate knockout *ELAVL3* in Kelly neuroblastoma cells (RRID:CVCL2092) with guide RNA sequences UGGCUUUGUCUGCAUCAUUG (cut location: chr19:11,466,233). Two lines were developed with either a +1-nucleotide insertion or a -7-nucleotide deletion in exon 3, resulting in frameshift that precludes normal ELAVL3 production. Sequence changes were confirmed with PCR and sequencing primers: CTTACAGGGCCTGGCTGAC,

ACACTGGCAGGTGTCAAGG, and CTTACAGGGCCTGGCTGAC. Modified Kelly cells were grown in RPMI 1640 (Themo Scientific), 10% fetal bovine serum, and 10% penicillin-streptomycin 37 °C, 5% CO2.

3.4.3 Immunoblotting

Frozen nervous tissue was weighed and homogenized in ice-cold N-PER Neuronal Protein Extraction Reagent (1 mL/100mg, Fisher) with HALT Protease & Phosphatase Inhibitor Cocktail (Fisher). Protein concentrations were determined with Pierce BCA Protein Assay (Thermofisher). Equal amounts of total protein were boiled in SDS sample buffer for 5 minutes before running in a 12% Mini-Protean TGX Precast Protein Gel (Bio-Rad 4561045). Chameleon Duo Pre-Stained Protein Ladder (Li-Cor) was used as a size standard. We used the following recombinant nELAVL proteins: ELAVL2-GST fusion (ProteinTech Ag28310), ELAVL3:Hs fusion (Creative BioMart ELAVL3-1006H), and ELAVL4:GST (ProteinTech Ag3678). Proteins were transferred to a PVDF membrane, the membranes blocked with Intercept Blocking Buffer (Li-Cor), and then incubated with primary antibody diluted in Intercept T20 Antibody Diluent (Li-Cor) overnight at 4°C. Secondary antibodies used include IRDye® 800CW Goat anti-Rabbit IgG Secondary Antibody (Li-Cor) and IRDye® 680RD Goat anti-Mouse IgG Secondary Antibody (Li-Cor). Images were acquired using the Odyssey® Fc Imaging System from Li-COR. Image Studio Lite software was used to measure target signal intensity.

3.4.4 Cortical region and neuron identification

Cortical layers were roughly differentiated using overall cytoarchitecture as distinguished primarily by DAPI signal and secondarily by background staining of RGB channels. Cells were chosen for analysis due to high suspicion of neuronal identity. The following guidelines were utilized: the external granular layer (layer 2) is densely populated with small stellate and pyramidal cells, which have slightly larger nuclei (>12 μm in diameter) and less dense DAPI signal than neighboring glia; the external pyramidal layer (layer 3) is more sparsely populated with a larger proportion of pyramidal neurons (often having a roughly triangular nuclear shape); the internal pyramidal layer (layer 5) is populated by medium and large-sized pyramidal cells, which have a very large (often >15 μm in diameter) and sparsely DAPI-stained nucleus; layer 5 Betz cells were identified by their large size, multipolar cytoplasm, presence of lipofuscin, and large nucleus with less dense DAPI staining; the multiform layer (layer 6) is closest to the densely populated white matter and itself contains a small proportion of large pyramidal cells and many smaller neurons that can be differentiated from glia by their larger nuclear diameter and fainter staining).

3.4.5 Immunofluorescence

6 μm-thick tissue sections were cut from blocks of formalin-fixed paraffin-embedded tissue. Sections were deparaffinized with CitriSolv and hydrated with a graded alcohol series. Antigen retrieval using a Tris-based unmasking solution (VectorLabs) was performed in an electric steamer for 20 minutes. Sections were permeabilized in 0.2% Triton X-100, blocked with 5% normal horse serum, and incubated with primary antibody overnight at 4°C. Slides were then incubated with DAPI (1 ug/mL) and the autofluorescence quenched

with TrueBlack Lipofuscin Autofluorescence Quencher (Biotium). Slides were coverslipped using Pro-Long Gold Antifade Mountant with DAPI (Fisher).

3.4.6 Imaging and digital processing, and quantitative analysis of IF

Sections of spinal cord, motor cortex, and frontal cortex were stained with the antibodies as described below. Immunofluorescence was visualized and digital photographs taken using the Olympus VS200 Slide Scanner at 20X magnification (UCSD Microscopy Core) for quantitative measurements. For quantitative evaluation of nuclear fluorescent intensity of ELAVL3 and TDP-43 within different cortical layers, Olympus OlyVIA 3.2 software was used to capture and export ~375 by 210 μm RBG snapshots. A minimum of twenty regions were exported. These exported .tif images were further processed with Fiji software. Nuclear regions of interest were drawn using the freehand tool of the software and the DAPI signal, and the nuclear area (pixels) and mean intensity of each channel was collected. For each .tif image, the background signal of each channel, defined using a region with no cell bodies was recorded. The nuclear signal for each channel was defined as the ROI mean gray value minus the measured background for that channel ($\text{Signal}_{\text{DAPI Channel}} = \text{Nuclear Intensity of ROI}_{\text{DAPI Channel}} - \text{Measured Background}_{\text{DAPI Channel}}$). To compare nuclear intensity of cells with and without aggregates in the same field, the same process was used to export images and collect the nuclear intensity values. Then, we divided nuclear intensity of a cell by the average nuclear intensity of all non-aggregate-containing cells.

3.4.7   Statistical analysis

Data were analyzed using GraphPad Prism 9.4 and graphed as a mean ± standard error. Significance was assessed using Wilcoxon-Mann-Whitney test or one-way ANOVA and a post hoc Holm-Šídák multiple comparisons test as indicated in the text. P-values less than 0.05 were considered significant.

3.4.8   Primary antibodies

Table 3.10: List of primary antibodies used.

Antibody	Target	Info
ProteinTech 55047-1-AP	ELAVL3 (aa:19-36)	Polyclonal rabbit
Sino A10289	ELAVL3 (aa: 20-36)	Polyclonal rabbit
LsBio C408905	ELAVL3 (aa: 1-100)	Polyclonal rabbit
Sino A10290	ELAVL3 (aa: 71-93)	Polyclonal rabbit
MBS9214452	ELAVL3 (aa:71-99)	Polyclonal rabbit
Abclonal A6091	ELAVL3 (aa:161-260)	Polyclonal rabbit
LsBio C307383	ELAVL3 (aa:1-368)	Polyclonal rabbit
Abcam ab184267	ELAVL3/ELAVL4	Mouse monoclonal
Calbiochem DR1075	TDP-43 (aa:1-261) 2E2-D3	Mouse monoclonal
ProteinTech 67345-1-Ig	TDP-43 C-term	Mouse monoclonal
BioLegend 829901	pTDP-43 409/410	Rat monoclonal
ProteinTech 66318-1-Ig	pTDP-43 409/410	Mouse monoclonal
Invitrogen MN1020	pTau Ser202/Thr205	Mouse monoclonal
ProteinTech 60004-1-Ig	GAPDH	Mouse monoclonal
ProteinTech 66240-1-Ig	Beta Tubulin	Mouse monoclonal
Millipore MAB377	NeuN A60 clone	Mouse monoclonal
Millipore MAB3402	GFAP GA5 clone	Mouse monoclonal
Millipore MABN50	Olig2 211F1.1 clone	Mouse monoclonal

REFERENCES

1. Rabinovici, G. D. & Miller, B. L. *Frontotemporal Lobar Degeneration: Epidemiology, Pathophysiology, Diagnosis and Management. CNS Drugs* vol. 24 (2010).

2. Ling, S.-C., Polymenidou, M. & Cleveland, D. W. Converging Mechanisms in ALS and FTD: Disrupted RNA and Protein Homeostasis. *Neuron* **79**, 416–438 (2013).

3. Mackenzie, I. R. A., Bigio, E. H., Ince, P. G., Geser, F., Neumann, M., Cairns, N. J., Kwong, L. K., Forman, M. S., Ravits, J., Stewart, H., Eisen, A., McClusky, L., Kretzschmar, H. A., Monoranu, C. M., Highley, J. R., Kirby, J., Siddique, T., Shaw, P. J., Lee, V. M. & Trojanowski, J. Q. Pathological TDP-43 distinguishes sporadic amyotrophic lateral sclerosis from amyotrophic lateral sclerosis with SOD1 mutations. *Ann. Neurol.* **61**, 427–434 (2007).

4. Maziuk, B. F., Apicco, D. J., Cruz, A. L., Jiang, L., Ash, P. E. A., da Rocha, E. L., Zhang, C., Yu, W. H., Leszyk, J., Abisambra, J. F., Li, H. & Wolozin, B. RNA binding proteins co-localize with small tau inclusions in tauopathy. *Acta Neuropathol. Commun.* **6**, 71 (2018).

5. Diaz-Garcia, S., Ko, V. I., Vazquez-Sanchez, S., Chia, R., Arogundade, O. A., Rodriguez, M. J., Traynor, B. J., Cleveland, D. W. & Ravits, J. Nuclear depletion of RNA binding protein ELAVL3 (HuC) in sporadic and familial amyotrophic lateral sclerosis. *Acta Neuropathol.* **142**, 985–1001 (2021).

6. Ho, R., Workman, M. J., Mathkar, P., Wu, K., Kim, K. J., O'Rourke, J. G., Kellogg, M., Montel, V., Banuelos, M. G., Arogundade, O. A., Diaz-Garcia, S., Oheb, D., Huang, S., Khrebtukova, I., Watson, L., Ravits, J., Taylor, K., Baloh, R. H., Svendsen, C. N., O'Rourke, J. G., Kellogg, M., Montel, V., Banuelos, M. G., Arogundade, O. A., Diaz-Garcia, S., Oheb, D., Huang, S., Khrebtukova, I., Watson, L., Ravits, J., Taylor, K., Baloh, R. H. & Svendsen, C. N. Cross-Comparison of Human iPSC Motor Neuron Models of Familial and Sporadic ALS Reveals Early and Convergent Transcriptomic Disease Signatures. *Cell Syst.* **12**, 159-175.e9 (2021).

7. Ravanidis, S., Kattan, F. G. & Doxakis, E. Unraveling the pathways to neuronal homeostasis and disease: Mechanistic insights into the role of RNA-binding proteins and associated factors. *Int. J. Mol. Sci.* **19**, 1–49 (2018).

8. Polymenidou, M., Lagier-Tourenne, C., Hutt, K. R., Huelga, S. C., Moran, J., Liang, T. Y., Ling, S.-C., Sun, E., Wancewicz, E., Mazur, C., Kordasiewicz, H., Sedaghat, Y., Donohue, J. P., Shiue, L., Bennett, C. F., Yeo, G. W. & Cleveland, D. W. Long pre-mRNA depletion and RNA missplicing contribute to neuronal vulnerability from loss of TDP-43. *Nat. Neurosci.* **14**, 459–468 (2011).

9. Ling, J. P., Pletnikova, O., Troncoso, J. C. & Wong, P. C. TDP-43 repression of nonconserved cryptic exons is compromised in ALS-FTD. *Science (80-.).* **349**, 650–

655 (2015).

10. Klim, J. R., Williams, L. A., Limone, F., Guerra San Juan, I., Davis-Dusenbery, B. N., Mordes, D. A., Burberry, A., Steinbaugh, M. J., Gamage, K. K., Kirchner, R., Moccia, R., Cassel, S. H., Chen, K., Wainger, B. J., Woolf, C. J. & Eggan, K. ALS-implicated protein TDP-43 sustains levels of STMN2, a mediator of motor neuron growth and repair. *Nat. Neurosci.* **22**, 167–179 (2019).

11. Seddighi, S., Qi, Y. A., Brown, A.-L., Wilkins, O. G., Bereda, C., Belair, C., Zhang, Y.-J., Prudencio, M., Keuss, M. J., Khandeshi, A., Pickles, S., Kargbo-Hill, S. E., Hawrot, J., Ramos, D. M., Yuan, H., Roberts, J., Sacramento, E. K., Shah, S. I., Nalls, M. A., Colón-Mercado, J. M., Reyes, J. F., Ryan, V. H., Nelson, M. P., Cook, C. N., Li, Z., Screven, L., Kwan, J. Y., Mehta, P. R., Zanovello, M., Hallegger, M., Shantaraman, A., Ping, L., Koike, Y., Oskarsson, B., Staff, N. P., Duong, D. M., Ahmed, A., Secrier, M., Ule, J., Jacobson, S., Reich, D. S., Rohrer, J. D., Malaspina, A., Dickson, D. W., Glass, J. D., Ori, A., Seyfried, N. T., Maragkakis, M., Petrucelli, L., Fratta, P. & Ward, M. E. Mis-spliced transcripts generate de novo proteins in TDP-43–related ALS/FTD. *Sci. Transl. Med.* **16**, 1–18 (2024).

12. Kiernan, M. C., Vucic, S., Cheah, B. C., Turner, M. R., Eisen, A., Hardiman, O., Burrell, J. R. & Zoing, M. C. Amyotrophic lateral sclerosis. *Lancet* **377**, 942–955 (2011).

13. Bell, C. *The Nervous System of the Human Body: Embracing the Papers Delivered to the Royal Society on the Subject of the Nerves.* (London: longman, rees, orme, brown, and green, 1830).

14. Aran, F. A. Recherches sur une maladie non encore décrite du systéme musculaire (atrophie musculaire progressive). *Arch Gen Med* **24**, 172 (1850).

15. Cruveilhier, J. Sur la paralysie musculaire progressive atrophique. *Arch. Générales Médecine* **5**, 561–603 (1853).

16. Drouin, E. & Péréon, Y. Paralysis with muscle atrophy. *Lancet Neurol.* **14**, 1157 (2015).

17. Charcot, J. M. De la sclérose latérale amyotrophique. *Prog Med* **2**, 341–453 (1874).

18. Gowers, W. R. *A Manual of Diseases of the Nervous System.* (J. & A. Churchill, London, 1886).

19. Turner, M. R., Swash, M. & Ebers, G. C. Lockhart Clarke's contribution to the description of amyotrophic lateral sclerosis. *Brain* **133**, 3470–3479 (2010).

20. Grad, L. I., Rouleau, G. A., Ravits, J. & Cashman, N. R. Clinical Spectrum of Amyotrophic Lateral Sclerosis (ALS). *Cold Spring Harb. Perspect. Med.* **7**, 1–16 (2017).

21. Ravits, J. M. & La Spada, A. R. Als motor phenotype heterogeneity, focality, and spread: Deconstructing motor neuron degenerationsymbol. *Neurology* **73**, 805 (2009).

22. Logroscino, G., Traynor, B. J., Hardiman, O., Chio, A., Mitchell, D., Swingler, R. J., Millul, A., Benn, E. & Beghi, E. Incidence of amyotrophic lateral sclerosis in Europe. *J. Neurol. Neurosurg. Psychiatry* **81**, 385–390 (2010).

23. Lee, J. W., Kang, S.-W. & Choi, W. A. Clinical Course of Amyotrophic Lateral Sclerosis according to Initial Symptoms: An Analysis of 500 Cases. *Yonsei Med. J.* **62**, 338 (2021).

24. Connolly, O., Le Gall, L., McCluskey, G., Donaghy, C. G., Duddy, W. J. & Duguez, S. A systematic review of genotype–phenotype correlation across cohorts having causal mutations of different genes in ALS. *J. Pers. Med.* **10**, 1–27 (2020).

25. Chiò, A., Moglia, C., Canosa, A., Manera, U., Vasta, R., Brunetti, M., Barberis, M., Corrado, L., D'Alfonso, S., Bersano, E., Sarnelli, M. F., Solara, V., Zucchetti, J. P., Peotta, L., Iazzolino, B., Mazzini, L., Mora, G. & Calvo, A. Cognitive impairment across ALS clinical stages in a population-based cohort. *Neurology* **93**, E984–E994 (2019).

26. Olney, N. T., Spina, S. & Miller, B. L. Frontotemporal Dementia. *Neurol. Clin.* **35**, 339–374 (2017).

27. Pick, A. Uber die Beziehungen der senilen Hirnatrophie zur Aphasie. *Prag Med Wchnschr* **17**, 165–167 (1892).

28. Pearce, J. Pick's disease. *J. Neurol. Neurosurg. Psychiatry* **74**, 169 (2003).

29. Thibodeau, M.-P. & Miller, B. L. 'Limits and current knowledge of Pick's disease: its differential diagnosis' A translation of the 1957 Delay, Brion, Escourolle article. *Neurocase* **19**, 417–422 (2013).

30. Neary, D., Snowden, J. S., Gustafson, L., Passant, U., Stuss, D., Black, S., Freedman, M., Kertesz, A., Robert, P. H., Albert, M., Boone, K., Miller, B. L., Cummings, J. & Benson, D. F. Frontotemporal lobar degeneration: A consensus on clinical diagnostic criteria. *Neurology* **51**, 1546–1554 (1998).

31. Cairns, N. J., Bigio, E. H., Mackenzie, I. R. A., Neumann, M., Lee, V. M.-Y., Hatanpaa, K. J., White, C. L., Schneider, J. A., Grinberg, L. T., Halliday, G., Duyckaerts, C., Lowe, J. S., Holm, I. E., Tolnay, M., Okamoto, K., Yokoo, H., Murayama, S., Woulfe, J., Munoz, D. G., Dickson, D. W., Ince, P. G., Trojanowski, J. Q. & Mann, D. M. A. Neuropathologic diagnostic and nosologic criteria for frontotemporal lobar degeneration: consensus of the Consortium for Frontotemporal Lobar Degeneration. *Acta Neuropathol.* **114**, 5–22 (2007).

32. Warren, J. D., Rohrer, J. D. & Rossor, M. N. Frontotemporal dementia. *BMJ* **347**, f4827–f4827 (2013).

33. Ringholz, G. M., Appel, S. H., Bradshaw, M., Cooke, N. A., Mosnik, D. M. & Schulz, P. E. Prevalence and patterns of cognitive impairment in sporadic ALS. *Neurology* **65**, 586–590 (2005).

34. Brodaty, H., Seeher, K. & Gibson, L. Dementia time to death: a systematic literature review on survival time and years of life lost in people with dementia. *Int. Psychogeriatrics* **24**, 1034–1045 (2012).

35. Johnson, J. K., Diehl, J., Mendez, M. F., Neuhaus, J., Shapira, J. S., Forman, M., Chute, D. J., Roberson, E. D., Pace-Savitsky, C., Neumann, M., Chow, T. W., Rosen, H. J., Forstl, H., Kurz, A. & Miller, B. L. Frontotemporal Lobar Degeneration. *Arch. Neurol.* **62**, (2005).

36. Irwin, D. J. Tauopathies as clinicopathological entities. *Park. Relat. Disord.* **22**, S29–S33 (2016).

37. Kawakami, I., Arai, T. & Hasegawa, M. The basis of clinicopathological heterogeneity in TDP-43 proteinopathy. *Acta Neuropathol.* **138**, 751–770 (2019).

38. Saberi, S., Stauffer, J. E., Schulte, D. J. & Ravits, J. Neuropathology of Amyotrophic Lateral Sclerosis and Its Variants. *Neurol. Clin.* **33**, 855–876 (2015).

39. Leigh, P. N., Anderton, B. H., Dodson, A., Gallo, J.-M., Swash, M. & Power, D. M. Ubiquitin deposits in anterior horn cells in motor neurone disease. *Neurosci. Lett.* **93**, 197–203 (1988).

40. Lowe, J., Lennox, G., Jefferson, D., Morrell, K., McQuire, D., Gray, T., Landon, M., Doherty, F. J. & Mayer, R. J. A filamentous inclusion body within anterior horn neurones in motor neurone disease defined by immunocytochemical localisation of ubiquitin. *Neurosci. Lett.* **94**, 203–210 (1988).

41. Knopman, D. S. & Roberts, R. O. Estimating the Number of Persons with Frontotemporal Lobar Degeneration in the US Population. *J. Mol. Neurosci.* **45**, 330–335 (2011).

42. Neumann, M., Sampathu, D. M., Kwong, L. K., Truax, A. C., Micsenyi, M. C., Chou, T. T., Bruce, J., Schuck, T., Grossman, M., Clark, C. M., McCluskey, L. F., Miller, B. L., Masliah, E., Mackenzie, I. R., Feldman, H., Feiden, W., Kretzschmar, H. A., Trojanowski, J. Q. & Lee, V. M.-Y. Ubiquitinated TDP-43 in Frontotemporal Lobar Degeneration and Amyotrophic Lateral Sclerosis. *Science (80-.).* **314**, 130–133 (2006).

43. Arai, T., Hasegawa, M., Akiyama, H., Ikeda, K., Nonaka, T., Mori, H., Mann, D., Tsuchiya, K., Yoshida, M., Hashizume, Y. & Oda, T. TDP-43 is a component of

ubiquitin-positive tau-negative inclusions in frontotemporal lobar degeneration and amyotrophic lateral sclerosis. *Biochem. Biophys. Res. Commun.* **351**, 602–611 (2006).

44. Mackenzie, I. R. A., Neumann, M., Baborie, A., Sampathu, D. M., Du Plessis, D., Jaros, E., Perry, R. H., Trojanowski, J. Q., Mann, D. M. A. & Lee, V. M. Y. A harmonized classification system for FTLD-TDP pathology. *Acta Neuropathol.* **122**, 111–113 (2011).

45. Lee, E. B., Porta, S., Michael Baer, G., Xu, Y., Suh, E. R., Kwong, L. K., Elman, L., Grossman, M., Lee, V. M. Y., Irwin, D. J., Van Deerlin, V. M. & Trojanowski, J. Q. Expansion of the classification of FTLD-TDP: distinct pathology associated with rapidly progressive frontotemporal degeneration. *Acta Neuropathol.* **134**, 65–78 (2017).

46. Burrell, J. R., Kiernan, M. C., Vucic, S. & Hodges, J. R. Motor Neuron dysfunction in frontotemporal dementia. *Brain* **134**, 2582–2594 (2011).

47. Chen, S., Sayana, P., Zhang, X. & Le, W. Genetics of amyotrophic lateral sclerosis: an update. *Mol. Neurodegener.* **8**, 28 (2013).

48. Irwin, D. J., Cairns, N. J., Grossman, M., McMillan, C. T., Lee, E. B., Van Deerlin, V. M., Lee, V. M.-Y. & Trojanowski, J. Q. Frontotemporal lobar degeneration: defining phenotypic diversity through personalized medicine. *Acta Neuropathol.* **129**, 469–491 (2015).

49. Posner, J. B. & Furneaux, H. M. Paraneoplastic syndromes. *Res. Publ. Assoc. Res. Nerv. Ment. Dis.* **68**, 187–219 (1990).

50. Furneaux, H. F., Reich, L. & Posner, J. B. Autoantibody synthesis in the central nervous system of patients with paraneoplastic syndromes. *Neurology* **40**, 1085–1085 (1990).

51. Szabo, A., Dalmau, J., Manley, G., Rosenfeld, M., Wong, E., Henson, J., Posner, J. B. & Furneaux, H. M. HuD, a paraneoplastic encephalomyelitis antigen, contains RNA-binding domains and is homologous to Elav and Sex-lethal. *Cell* **67**, 325–333 (1991).

52. Good, P. J. A conserved family of elav-like genes in vertebrates. *Proc. Natl. Acad. Sci.* **92**, 4557–4561 (1995).

53. Ma, W. J., Chung, S. & Furneaux, H. The Elav-like proteins bind to AU-rich elements and to the poly(A) tail of mRNA. *Nucleic Acids Res.* **25**, 3564–3569 (1997).

54. Hinman, M. N., Zhou, H.-L., Sharma, A. & Lou, H. All three RNA recognition motifs and the hinge region of HuC play distinct roles in the regulation of alternative splicing. *Nucleic Acids Res.* **41**, 5049–5061 (2013).

55. Scheiba, R. M., De Opakua, A. I., Díaz-Quintana, A., Cruz-Gallardo, I., Martínez-Cruz, L. A., Martínez-Chantar, M. L., Blanco, F. J. & Díaz-Moreno, I. The C-terminal RNA binding motif of HuR is a multi-functional domain leading to HuR oligomerization and binding to U-rich RNA targets. *RNA Biol.* **11**, 1250–1261 (2014).

56. Kasashima, K., Sakashita, E., Saito, K. & Sakamoto, H. Complex formation of the neuron-specific ELAV-like Hu RNA-binding proteins. **30**, 4519–4526 (2002).

57. Fan, X. C. & Steitz, J. A. HNS, a nuclear-cytoplasmic shuttling sequence in HuR. *Proc. Natl. Acad. Sci. U. S. A.* **95**, 15293–15298 (1998).

58. Wakamatsu, Y. & Weston, J. A. Sequential expression and role of Hu RNA-binding proteins during neurogenesis. *Development* **124**, 3449–3460 (1997).

59. Okano, H. J. & Darnell, R. B. A hierarchy of Hu RNA binding proteins in developing and adult neurons. *J. Neurosci.* **17**, 3024–3037 (1997).

60. Ogawa, Y., Yamaguchi, J., Yano, M., Uchiyama, Y. & Okano, H. J. Elavl3 regulates neuronal polarity through the alternative splicing of an embryo-specific exon in AnkyrinG. *Neurosci. Res.* **135**, 13–20 (2018).

61. Ogawa, Y., Kakumoto, K., Yoshida, T., Kuwako, K. ichiro, Miyazaki, T., Yamaguchi, J., Konno, A., Hata, J., Uchiyama, Y., Hirai, H., Watanabe, M., Darnell, R. B., Okano, H. H. J. & Okano, H. H. J. Elavl3 is essential for the maintenance of Purkinje neuron axons. *Sci. Rep.* **8**, 2722 (2018).

62. Ince-Dunn, G., Okano, H. J., Jensen, K. B., Park, W. Y., Zhong, R., Ule, J., Mele, A., Fak, J. J., Yang, C. W., Zhang, C., Yoo, J., Herre, M., Okano, H., Noebels, J. L. & Darnell, R. B. Neuronal Elav-like (Hu) Proteins Regulate RNA Splicing and Abundance to Control Glutamate Levels and Neuronal Excitability. *Neuron* **75**, 1067–1080 (2012).

63. Grassi, E., Santoro, R., Umbach, A., Grosso, A., Oliviero, S., Neri, F., Conti, L., Ala, U., Provero, P., DiCunto, F. & Merlo, G. R. Choice of Alternative Polyadenylation Sites, Mediated by the RNA-Binding Protein Elavl3, Plays a Role in Differentiation of Inhibitory Neuronal Progenitors. *Front. Cell. Neurosci.* **12**, (2019).

64. Koren, S. A., Galvis-Escobar, S. & Abisambra, J. F. Tau-mediated dysregulation of RNA: Evidence for a common molecular mechanism of toxicity in frontotemporal dementia and other tauopathies. *Neurobiol. Dis.* **141**, 104939 (2020).

65. Wolozin, B. & Ivanov, P. Stress granules and neurodegeneration. *Nat. Rev. Neurosci.* **20**, 649–666 (2019).

66. Tollervey, J. R., Curk, T., Rogelj, B., Briese, M., Cereda, M., Kayikci, M., König, J., Hortobágyi, T., Nishimura, A. L., Župunski, V., Patani, R., Chandran, S., Rot, G., Zupan, B., Shaw, C. E. & Ule, J. Characterizing the RNA targets and position-

dependent splicing regulation by TDP-43. *Nat. Neurosci.* **14**, 452–458 (2011).

67. Gomez, N., Hsieh, C., Li, X., Dykstra, M., Waksmacki, J., Altheim, C., Bechar, Y., Klim, J., Zaepfel, B., Rothstein, J., Tank, E. E. M., Barmada, S. J., Rna, C., Klim, J., Zaepfel, B., Rothstein, J., Tank, E. E. M. & Barmada, S. J. Counter-regulation of RNA stability by UPF1 and TDP43. *bioRxiv Prepr. Serv. Biol.* (2024) doi:10.1101/2024.01.31.578310.

68. Alessandrini, F., Wright, M., Kurosaki, T., Maquat, L. E. & Kiskinis, E. ALS-Associated TDP-43 Dysfunction Compromises UPF1-Dependent mRNA Metabolism Pathways Including Alternative Polyadenylation and 3'UTR Length. *bioRxiv Prepr. Serv. Biol.* (2024) doi:10.1101/2024.01.31.578311.

69. Krach, F., Batra, R., Wheeler, E. C., Vu, A. Q., Wang, R., Hutt, K., Rabin, S. J., Baughn, M. W., Libby, R. T., Diaz-Garcia, S., Stauffer, J., Pirie, E., Saberi, S., Rodriguez, M., Madrigal, A. A., Kohl, Z., Winner, B., Yeo, G. W. & Ravits, J. Transcriptome–pathology correlation identifies interplay between TDP-43 and the expression of its kinase CK1E in sporadic ALS. *Acta Neuropathol.* **136**, 405–423 (2018).

70. Melamed, Z., López-Erauskin, J., Baughn, M. W., Zhang, O., Drenner, K., Sun, Y., Freyermuth, F., McMahon, M. A., Beccari, M. S., Artates, J. W., Ohkubo, T., Rodriguez, M., Lin, N., Wu, D., Bennett, C. F., Rigo, F., Da Cruz, S., Ravits, J., Lagier-Tourenne, C. & Cleveland, D. W. Premature polyadenylation-mediated loss of stathmin-2 is a hallmark of TDP-43-dependent neurodegeneration. *Nat. Neurosci.* **22**, 180–190 (2019).

71. Prudencio, M., Humphrey, J., Pickles, S., Brown, A. L., Hill, S. E., Kachergus, J. M., Shi, J., Heckman, M. G., Spiegel, M. R., Cook, C., Song, Y., Yue, M., Daughrity, L. M., Carlomagno, Y., Jansen-West, K., de Castro, C. F., DeTure, M., Koga, S., Wang, Y. C., Sivakumar, P., Bodo, C., Candalija, A., Talbot, K., Selvaraj, B. T., Burr, K., Chandran, S., Newcombe, J., Lashley, T., Hubbard, I., Catalano, D., Kim, D., Propp, N., Fennessey, S., Fagegaltier, D., Phatnani, H., Secrier, M., Fisher, E. M. C., Oskarsson, B., van Blitterswijk, M., Rademakers, R., Graff-Radford, N. R., Boeve, B. F., Knopman, D. S., Petersen, R. C., Josephs, K. A., Aubrey Thompson, E., Raj, T., Ward, M., Dickson, D. W., Gendron, T. F., Fratta, P. & Petrucelli, L. Truncated stathmin-2 is a marker of TDP-43 pathology in frontotemporal dementia. *J. Clin. Invest.* **130**, 6080–6092 (2020).

72. Baughn, M. W., Melamed, Z., López-Erauskin, J., Beccari, M. S., Ling, K., Zuberi, A., Presa, M., Gonzalo-Gil, E., Maimon, R., Vazquez-Sanchez, S., Chaturvedi, S., Bravo-Hernández, M., Taupin, V., Moore, S., Artates, J. W., Acks, E., Ndayambaje, I. S., Agra de Almeida Quadros, A. R., Jafar-nejad, P., Rigo, F., Bennett, C. F., Lutz, C., Lagier-Tourenne, C. & Cleveland, D. W. Mechanism of STMN2 cryptic splice-polyadenylation and its correction for TDP-43 proteinopathies. *Science (80-.).* **379**, 1140–1149 (2023).

73. Willemse, S. W., Harley, P., van Eijk, R. P. A., Demaegd, K. C., Zelina, P., Pasterkamp, R. J., van Damme, P., Ingre, C., van Rheenen, W., Veldink, J. H., Kiernan, M. C., Al-Chalabi, A., van den Berg, L. H., Fratta, P. & van Es, M. A. UNC13A in amyotrophic lateral sclerosis: from genetic association to therapeutic target. *J. Neurol. Neurosurg. Psychiatry* **94**, 649–656 (2023).

74. Ma, X. R., Prudencio, M., Koike, Y., Vatsavayai, S. C., Kim, G., Harbinski, F., Briner, A., Rodriguez, C. M., Guo, C., Akiyama, T., Schmidt, H. B., Cummings, B. B., Wyatt, D. W., Kurylo, K., Miller, G., Mekhoubad, S., Sallee, N., Mekonnen, G., Ganser, L., Rubien, J. D., Jansen-West, K., Cook, C. N., Pickles, S., Oskarsson, B., Graff-Radford, N. R., Boeve, B. F., Knopman, D. S., Petersen, R. C., Dickson, D. W., Shorter, J., Myong, S., Green, E. M., Seeley, W. W., Petrucelli, L. & Gitler, A. D. TDP-43 represses cryptic exon inclusion in the FTD–ALS gene UNC13A. *Nature* **603**, 124–130 (2022).

75. Brown, A. L., Wilkins, O. G., Keuss, M. J., Hill, S. E., Zanovello, M., Lee, W. C., Bampton, A., Lee, F. C. Y., Masino, L., Qi, Y. A., Bryce-Smith, S., Gatt, A., Hallegger, M., Fagegaltier, D., Phatnani, H., Phatnani, H., Kwan, J., Sareen, D., Broach, J. R., Simmons, Z., Arcila-Londono, X., Lee, E. B., Van Deerlin, V. M., Shneider, N. A., Fraenkel, E., Ostrow, L. W., Baas, F., Zaitlen, N., Berry, J. D., Malaspina, A., Fratta, P., Cox, G. A., Thompson, L. M., Finkbeiner, S., Dardiotis, E., Miller, T. M., Chandran, S., Pal, S., Hornstein, E., MacGowan, D. J., Heiman-Patterson, T., Hammell, M. G., Patsopoulos, N. A., Butovsky, O., Dubnau, J., Nath, A., Bowser, R., Harms, M., Aronica, E., Poss, M., Phillips-Cremins, J., Crary, J., Atassi, N., Lange, D. J., Adams, D. J., Stefanis, L., Gotkine, M., Baloh, R. H., Babu, S., Raj, T., Paganoni, S., Shalem, O., Smith, C., Zhang, B., Harris, B., Broce, I., Drory, V., Ravits, J., McMillan, C., Menon, V., Wu, L., Altschuler, S., Lerner, Y., Sattler, R., Van Keuren-Jensen, K., Rozenblatt-Rosen, O., Lindblad-Toh, K., Nicholson, K., Gregersen, P., Lee, J. H., Kokos, S., Muljo, S., Newcombe, J., Gustavsson, E. K., Seddighi, S., Reyes, J. F., Coon, S. L., Ramos, D., Schiavo, G., Fisher, E. M. C., Raj, T., Secrier, M., Lashley, T., Ule, J., Buratti, E., Humphrey, J., Ward, M. E. & Fratta, P. TDP-43 loss and ALS-risk SNPs drive mis-splicing and depletion of UNC13A. *Nature* **603**, 131–137 (2022).

76. López-Erauskin, J., Bravo-Hernandez, M., Presa, M., Baughn, M. W., Melamed, Z., Beccari, M. S., Agra de Almeida Quadros, A. R., Arnold-Garcia, O., Zuberi, A., Ling, K., Platoshyn, O., Niño-Jara, E., Ndayambaje, I. S., McAlonis-Downes, M., Cabrera, L., Artates, J. W., Ryan, J., Hermann, A., Ravits, J., Bennett, C. F., Jafar-Nejad, P., Rigo, F., Marsala, M., Lutz, C. M., Cleveland, D. W. & Lagier-Tourenne, C. Stathmin-2 loss leads to neurofilament-dependent axonal collapse driving motor and sensory denervation. *Nat. Neurosci.* **27**, (2023).

77. Agra Almeida Quadros, A. R., Li, Z., Wang, X., Ndayambaje, I. S., Aryal, S., Ramesh, N., Nolan, M., Jayakumar, R., Han, Y., Stillman, H., Aguilar, C., Wheeler, H. J., Connors, T., Lopez-Erauskin, J., Baughn, M. W., Melamed, Z., Beccari, M. S., Olmedo Martínez, L., Canori, M., Lee, C. Z., Moran, L., Draper, I., Kopin, A. S., Oakley, D. H., Dickson, D. W., Cleveland, D. W., Hyman, B. T., Das, S., Ertekin-Taner, N. & Lagier-Tourenne, C. Cryptic splicing of stathmin-2 and UNC13A mRNAs

is a pathological hallmark of TDP-43-associated Alzheimer's disease. *Acta Neuropathol.* **147**, (2024).

78. Dittman, J. S. Unc13: a multifunctional synaptic marvel. *Curr. Opin. Neurobiol.* **57**, 17–25 (2019).

79. Ravits, J., Laurie, P., Fan, Y. & Moore, D. H. Implications of ALS focality: rostral-caudal distribution of lower motor neuron loss postmortem. *Neurology* **68**, 1576–1582 (2007).

80. Brettschneider, J., Arai, K., Del Tredici, K., Toledo, J. B., Robinson, J. L., Lee, E. B., Kuwabara, S., Shibuya, K., Irwin, D. J., Fang, L., Van Deerlin, V. M., Elman, L., McCluskey, L., Ludolph, A. C., Lee, V. M.-Y., Braak, H. & Trojanowski, J. Q. TDP-43 pathology and neuronal loss in amyotrophic lateral sclerosis spinal cord. *Acta Neuropathol.* **128**, 423–437 (2014).

81. Tan, R. H., McCann, H., Shepherd, C. E., Pinkerton, M., Mazumder, S., Devenney, E. M., Adler, G. L., Rowe, D. B., Kril, J., Halliday, G. M. & Kiernan, M. C. Heterogeneity of cortical pTDP-43 inclusion morphologies in amyotrophic lateral sclerosis. *Acta Neuropathol. Commun.* **11**, 1–12 (2023).

82. Lu, Y. L., Liu, Y., McCoy, M. J. & Yoo, A. S. MiR-124 synergism with ELAVL3 enhances target gene expression to promote neuronal maturity. *Proc. Natl. Acad. Sci. U. S. A.* **118**, (2021).

83. Sephton, C. F., Good, S. K., Atkin, S., Dewey, C. M., Mayer, P., Herz, J. & Yu, G. TDP-43 Is a Developmentally Regulated Protein Essential for Early Embryonic Development. *J. Biol. Chem.* **285**, 6826–6834 (2010).

84. Igaz, L. M., Kwong, L. K., Lee, E. B., Chen-Plotkin, A., Swanson, E., Unger, T., Malunda, J., Xu, Y., Winton, M. J., Trojanowski, J. Q. & Lee, V. M.-Y. Dysregulation of the ALS-associated gene TDP-43 leads to neuronal death and degeneration in mice. *J. Clin. Invest.* **121**, 726–738 (2011).

85. Gendron, T. F., Bieniek, K. F., Zhang, Y.-J., Jansen-West, K., Ash, P. E. A., Caulfield, T., Daughrity, L., Dunmore, J. H., Castanedes-Casey, M., Chew, J., Cosio, D. M., van Blitterswijk, M., Lee, W. C., Rademakers, R., Boylan, K. B., Dickson, D. W. & Petrucelli, L. Antisense transcripts of the expanded C9ORF72 hexanucleotide repeat form nuclear RNA foci and undergo repeat-associated non-ATG translation in c9FTD/ALS. *Acta Neuropathol.* **126**, 829–844 (2013).

86. Mori, K., Arzberger, T., Grässer, F. A., Gijselinck, I., May, S., Rentzsch, K., Weng, S.-M., Schludi, M. H., van der Zee, J., Cruts, M., Van Broeckhoven, C., Kremmer, E., Kretzschmar, H. A., Haass, C. & Edbauer, D. Bidirectional transcripts of the expanded C9orf72 hexanucleotide repeat are translated into aggregating dipeptide repeat proteins. *Acta Neuropathol.* **126**, 881–893 (2013).

87. Zu, T., Liu, Y., Bañez-Coronel, M., Reid, T., Pletnikova, O., Lewis, J., Miller, T. M., Harms, M. B., Falchook, A. E., Subramony, S. H., Ostrow, L. W., Rothstein, J. D., Troncoso, J. C. & Ranum, L. P. W. RAN proteins and RNA foci from antisense transcripts in C9ORF72 ALS and frontotemporal dementia. *Proc. Natl. Acad. Sci.* **110**, (2013).

88. Taylor, J. P., Brown, R. H. & Cleveland, D. W. Decoding ALS: From genes to mechanism. *Nature* **539**, 197–206 (2016).

89. Prasad, A., Bharathi, V., Sivalingam, V., Girdhar, A. & Patel, B. K. Molecular mechanisms of TDP-43 misfolding and pathology in amyotrophic lateral sclerosis. *Front. Mol. Neurosci.* **12**, 1–36 (2019).

90. Porta, S., Xu, Y., Lehr, T., Zhang, B., Meymand, E., Olufemi, M., Stieber, A., Lee, E. B., Trojanowski, J. Q. & Lee, V. M. -Y. Distinct brain-derived TDP-43 strains from FTLD-TDP subtypes induce diverse morphological TDP-43 aggregates and spreading patterns in vitro and in vivo. *Neuropathol. Appl. Neurobiol.* **47**, 1033–1049 (2021).

91. Narasimhan, S., Guo, J. L., Changolkar, L., Stieber, A., McBride, J. D., Silva, L. V., He, Z., Zhang, B., Gathagan, R. J., Trojanowski, J. Q. & Lee, V. M. Y. Pathological tau strains from human brains recapitulate the diversity of tauopathies in nontransgenic mouse brain. *J. Neurosci.* **37**, 11406–11423 (2017).

92. Scheckel, C., Drapeau, E., Frias, M. A., Park, C. Y., Fak, J., Zucker-Scharff, I., Kou, Y., Haroutunian, V., Ma'ayan, A., Buxbaum, J. D. & Darnell, R. B. Regulatory consequences of neuronal ELAV-like protein binding to coding and non-coding RNAs in human brain. *Elife* **5**, 1–35 (2016).

93. Sjöstedt, E., Zhong, W., Fagerberg, L., Karlsson, M., Mitsios, N., Adori, C., Oksvold, P., Edfors, F., Limiszewska, A., Hikmet, F., Huang, J., Du, Y., Lin, L., Dong, Z., Yang, L., Liu, X., Jiang, H., Xu, X., Wang, J., Yang, H., Bolund, L., Mardinoglu, A., Zhang, C., von Feilitzen, K., Lindskog, C., Pontén, F., Luo, Y., Hökfelt, T., Uhlén, M. & Mulder, J. An atlas of the protein-coding genes in the human, pig, and mouse brain. *Science (80-.).* **367**, (2020).

94. Bakken, T. E., Jorstad, N. L., Hu, Q., Lake, B. B., Tian, W., Kalmbach, B. E., Crow, M., Hodge, R. D., Krienen, F. M., Sorensen, S. A., Eggermont, J., Yao, Z., Aevermann, B. D., Aldridge, A. I., Bartlett, A., Bertagnolli, D., Casper, T., Castanon, R. G., Crichton, K., Daigle, T. L., Dalley, R., Dee, N., Dembrow, N., Diep, D., Ding, S. L., Dong, W., Fang, R., Fischer, S., Goldman, M., Goldy, J., Graybuck, L. T., Herb, B. R., Hou, X., Kancherla, J., Kroll, M., Lathia, K., van Lew, B., Li, Y. E., Liu, C. S., Liu, H., Lucero, J. D., Mahurkar, A., McMillen, D., Miller, J. A., Moussa, M., Nery, J. R., Nicovich, P. R., Niu, S. Y., Orvis, J., Osteen, J. K., Owen, S., Palmer, C. R., Pham, T., Plongthongkum, N., Poirion, O., Reed, N. M., Rimorin, C., Rivkin, A., Romanow, W. J., Sedeño-Cortés, A. E., Siletti, K., Somasundaram, S., Sulc, J., Tieu, M., Torkelson, A., Tung, H., Wang, X., Xie, F., Yanny, A. M., Zhang, R., Ament, S.

A., Behrens, M. M., Bravo, H. C., Chun, J., Dobin, A., Gillis, J., Hertzano, R., Hof, P. R., Höllt, T., Horwitz, G. D., Keene, C. D., Kharchenko, P. V., Ko, A. L., Lelieveldt, B. P., Luo, C., Mukamel, E. A., Pinto-Duarte, A., Preissl, S., Regev, A., Ren, B., Scheuermann, R. H., Smith, K., Spain, W. J., White, O. R., Koch, C., Hawrylycz, M., Tasic, B., Macosko, E. Z., McCarroll, S. A., Ting, J. T., Zeng, H., Zhang, K., Feng, G., Ecker, J. R., Linnarsson, S. & Lein, E. S. Comparative cellular analysis of motor cortex in human, marmoset and mouse. *Nature* **598**, 111–119 (2021).

95.   Pineda, S. S., Lee, H., Ulloa-Navas, M. J., Linville, R. M., Garcia, F. J., Galani, K., Engelberg-Cook, E., Castanedes, M. C., Fitzwalter, B. E., Pregent, L. J., Gardashli, M. E., DeTure, M., Vera-Garcia, D. V., Hucke, A. T. S., Oskarsson, B. E., Murray, M. E., Dickson, D. W., Heiman, M., Belzil, V. V. & Kellis, M. Single-cell dissection of the human motor and prefrontal cortices in ALS and FTLD. *Cell* (2024) doi:10.1016/j.cell.2024.02.031.

96.   O'Leary, N. A., Wright, M. W., Brister, J. R., Ciufo, S., Haddad, D., McVeigh, R., Rajput, B., Robbertse, B., Smith-White, B., Ako-Adjei, D., Astashyn, A., Badretdin, A., Bao, Y., Blinkova, O., Brover, V., Chetvernin, V., Choi, J., Cox, E., Ermolaeva, O., Farrell, C. M., Goldfarb, T., Gupta, T., Haft, D., Hatcher, E., Hlavina, W., Joardar, V. S., Kodali, V. K., Li, W., Maglott, D., Masterson, P., McGarvey, K. M., Murphy, M. R., O'Neill, K., Pujar, S., Rangwala, S. H., Rausch, D., Riddick, L. D., Schoch, C., Shkeda, A., Storz, S. S., Sun, H., Thibaud-Nissen, F., Tolstoy, I., Tully, R. E., Vatsan, A. R., Wallin, C., Webb, D., Wu, W., Landrum, M. J., Kimchi, A., Tatusova, T., DiCuccio, M., Kitts, P., Murphy, T. D. & Pruitt, K. D. Reference sequence (RefSeq) database at NCBI: current status, taxonomic expansion, and functional annotation. *Nucleic Acids Res.* **44**, D733–D745 (2016).